FLOWS AND INSTABILITIES IN LOW-TEMPERATURE PLASMAS WITH IONIZATION AND CHARGE-EXCHANGE PROCESSES

A dissertation submitted to the

College of Graduate and Postdoctoral Studies

in partial pulfillment of the requirements

for the degree of Doctor of Philosophy

in the Department of Computer Science

University of Saskatchewan

Saskatoon

By

Oleksandr Chapurin

Permission to Use

In presenting this dissertation in partial fulfillment of the requirements for a Postgraduate degree from the University of Saskatchewan, I agree that the Libraries of this University may make it freely available for inspection. I further agree that permission for copying of this dissertation in any manner, in whole or in part, for scholarly purposes may be granted by the professor or professors who supervised my dissertation work or, in their absence, by the Head of the Department or the Dean of the College in which my dissertation work was done. It is understood that any copying or publication or use of this dissertation or parts thereof for financial gain shall not be allowed without my written permission. It is also understood that due recognition shall be given to me and to the University of Saskatchewan in any scholarly use which may be made of any material in my dissertation.

Disclaimer

Reference in this dissertation to any specific commercial products, process, or service by trade name, trademark, manufacturer, or otherwise, does not constitute or imply its endorsement, recommendation, or favouring by the University of Saskatchewan. The views and opinions of the author expressed herein do not state or reflect those of the University of Saskatchewan, and shall not be used for advertising or product endorsement purposes. Requests for permission to copy or to make other uses of materials in this dissertation in whole or part should be addressed to:

> Head of the Department of Physics & Engineering Physics
>
> 163 Physics Building, 116 Science Place
>
> University of Saskatchewan
>
> Saskatoon, Saskatchewan S7N 5E2 Canada
>
> OR
>
> Dean
>
> College of Graduate and Postdoctoral Studies
>
> University of Saskatchewan
>
> 116 Thorvaldson Building, 110 Science Place
>
> Saskatoon, Saskatchewan S7N 5C9 Canada

Abstract

Plasma is rich with waves and instabilities, on scales ranging from the fastest electron plasma waves down to the slow fluctuations due to ion and atom inertial effects. The common theme of this study is flows, nonlinear waves and instabilities in low-temperature plasmas with atomic processes such as ionization and instabilities. Several nonlinear plasma problems related to applications in electric propulsion and open-mirror linear fusion devices are studied in this thesis. Hall thrusters, the devices for electric propulsion, are prone to many waves and instability phenomena, and the low-frequency ionization oscillations (propagating along its channel) stand as most commonly observed (so-called breathing mode). Though the ionization nature of the breathing mode is generally accepted, with the mode frequency scaling as the fly-by time of the slow neutral atoms, exact mechanisms remain poorly understood. In this study, we formulate a full fluid model for three species: atoms, ions, and electrons, and perform a comprehensive benchmark study between the fluid model and hybrid model (heavy kinetic species and fluid electrons). A novel result of this study is the identification of two different regimes of breathing modes. In one regime, the breathing mode co-exists with the higher frequency resistive mode, and the second – is clear breathing mode. The main features and characteristics of these regimes are identified and confirmed in both models. Generally, the benchmark study shows a good agreement between the fluid and kinetic models. A simple reduced fluid model is proposed for the solo regime. In this regime, the ion backflow region (the near-anode region with negative ion velocity) is identified as a driving mechanism for the breathing mode.

The related theme of this work is the role of atomic physics effects (ionization and charge exchange) on plasma flow in the divertors of linear fusion devices. In open magnetic field configurations, the magnetic mirrors are placed at the ends both to confine the plasma in the core and to distribute output energy over a larger area, thus reducing the wall load. Direct interaction of plasma flow with the material wall results in the re-emission of neutrals into the plasma (recycling) due to particles' reflection, desorption, and other processes. This re-emitted neutral component can dramatically impact the whole system. It is found that the low-energy neutral component has the largest influence, generating ion sources (via ionization

and charge exchange) in the region near the wall and resulting in strong modification of plasma potential and flow. To study these effects, we have developed a time-dependent hybrid drift-kinetic code with a detailed model of atom transport near the wall, including collision processes. This tool can be used for studying global quasineutral plasma flow dynamics and its interaction with atom components, such as in divertors of linear fusion devices. To illustrate its capabilities, we confirm previous findings (based on qualitative and steady-state analysis) that the ion temperature in the source generally reduces the transport of neutral atoms. Additionally, we show that an increase in the density of slow atoms above some critical value results in dramatic destabilization of plasma flow via ion streaming instabilities.

Acknowledgements

My journey through the PhD program would not be possible on my own, and this thesis work would not exist without the continuous support of many people and organizations.

First, I would like to thank my supervisor, Dr. Andrei Smolyakov, who introduced me to the plasma physics research field since my MSc degree at the University of Saskatchewan. His continuous support and inspiration helped me successfully tackle many challenging problems during the PhD program.

I would like to thank my committee members, Dr. Raymond Spiteri, Dr. Lénaïc Couëdel, Dr. Mark Boland, and Dr. Rob Pywell. Additionally, I would like to thank Dr. Raymond Spiteri for his supervision during my Mitacs internship program. It was a valuable and exciting work experience bridging academia and industry.

I am thankful to all graduate students in our research group and beyond (the list of people is long). Thank you for interesting conversations, sharing experiences, and helping with English. I want to thank Marilyn Jimenez for our journey, e.g. surviving the isolation during the COVID-19 pandemic was very memorable.

A large part of my program was devoted to Hall thruster studies. At the very beginning of my program, I visited the LAPLACE laboratory (Université de Toulouse). I had a chance to work with Dr. Gerjan Hagelaar and Dr. Jean-Pierre Boeuf, world-renown scientists in the field. I am very thankful for your supervision, insights, and collaboration.

My last project during PhD program was conducted in collaboration (internship) with TAE Energy. I am very thankful to Peter Yushmanov for his supervision and Sean Dettrick's valuable suggestions.

I am grateful to be a recipient of the scholarships and awards: Dean's Scholarship, Herzberg Travel Awards, and Harvey Skarsgard Memorial Scholarship.

I am very thankful to my mother and brother for their continuous support.

Contents

List of Tables

List of Figures

CHAPTER 1

INTRODUCTION

1.1 Thesis motivation and outline

It is of great importance to study and understand diverse plasma phenomena to address fundamental problems of nature. Plasma is heavily used in modern technology, e.g. electric propulsion for space exploration, the problem of controlled thermonuclear fusion. Plasma is a gas of charged particles, and the long-range electromagnetic interaction defines its dynamics. It is also dense enough (quantitative discussion follows) to exhibit collective plasma effects absent for a simple collection of charged particles. This includes a tendency to keep overall electric neutrality and support many wave phenomena often exhibiting turbulence. Transport in plasma caused by turbulence is an unsolved problem of classical physics, and it is manifested in numerous plasma applications and natural phenomena.

This thesis studies the dynamics of low-temperature plasma with a large fraction of neutrals, thus focusing on the flows and lower-frequency plasma waves affected by collisional atomic processes such as ionization and charge exchange. The related applications include problems for electric propulsion (Hall thrusters) and linear fusion devices, specifically its divertor region dynamics. We study the equilibrium flow, the low-frequency waves and instabilities, and their mechanisms. The reduced plasma models are formulated for specific problems and include fluid and hybrid (combining fluid with kinetic) models.

In Chapter 2 we will start with the problem of ionization modes observed in Hall thrusters. These are electric propulsion devices successfully used for low-orbital and deep space missions. The so-called breathing modes are observed as low-frequency oscillations of the discharge current and all major plasma parameters along its channel (in the axial direction). Breathing modes are associated with the periodic interplay of plasma species and neutrals via the ioniza-

tion process. Periodic depletion of neutrals and their fly-by time define the frequency of the observed mode, but the exact mechanisms remain unknown. In this study, we will compare two models, fluid and hybrid, most commonly used for studying the axial dynamics of these thrusters. The models include dynamics of three species: ions, neutrals, and electrons, with ionization that supports the discharge in the applied potential across the channel. The problem of axial dynamics is non-linear and inherently non-local; it is particularly complicated for analytical studies, even for linearized equations. Thus, numerical simulations here are the primary tool to elucidate these processes. We compare fluid and hybrid models against each other and identify their major differences. Additionally, we identify two different regimes for breathing modes (seen in both models), one with pure breathing mode and the other regime where the breathing mode co-exists with the higher frequency resistive modes. The latter are also axial modes associated with ion fly-by times. These modes are highly sensitive to electron mobility and can lead to ion heating. Note that the breathing mode frequency is almost independent of electron mobility. Our benchmark shows that the ion heating and pressure effects are important when the resistive modes are present. For the pure breathing mode regime, we identified an important role of the ion-backflow region (where the ions flow toward anode), and plasma recombination at the anode, significantly impacting the breathing modes. The benchmark study between fluid and hybrid models exposed some limitations of the fluid description of heavy species and provided important insights about axial modes of Hall thrusters.

Chapter 3 is built on the investigation of the full dynamics of breathing modes outlined in Chapter 2. In Chapter 3, we propose a mechanism for the breathing mode and a reduced model. Various mechanisms for the breathing modes are proposed in literature based on the zero-dimensional predator-prey model for neutrals and ions. Construction of a simpler model, based on continuity equations of ions and neutrals, allowed to identify the importance of the ion backflow region (formed by presheath region near anode). We show substantial evidence that the ion backflow region is responsible for the excitation of low-frequency breathing modes.

An interesting problem, presented in Chapter 4, exists in the field of linear fusion devices, consists of studying plasma dynamics on the ends of such devices in the configuration of

converging-diverging magnetic fields. These are used to distribute the output energy (by flaring magnetic field lines) that inevitably leaks from a linear fusion device. By its definition and configuration, they are inherently open systems with direct contact between plasma and outer structures (walls). Wall material bombarded with plasma includes a multitude of processes, among which we will focus on neutral recycling processes (due to reflection and desorption). Slow neutrals, introduced to the system, will potentially create low-energy plasma species sources, affecting the plasma potential distribution and thus dynamics of the whole fusion device. It is interesting to point out that any distortions, plasma sources, and dynamics spread quickly (possibly with dramatic implications) along field lines throughout the whole device, affecting the source region.

Chapter 2 of the thesis is based on the manuscript prepared for publication (preprint is published), Chapter 3 is based on the published manuscript. Both contain a short preface with a description of how they relate to the main theme.

1.2   Brief history and definition of plasma

Historical perspective

The invention of the first vacuum pumps at the beginning of the 18th century and active studies of electric phenomena brought an interesting object associated with passing a current through partially evacuated gas tubes. The visible glow observed in these experiments, where a high voltage was applied between plates inside a partially vacuumed tube, named Geissler tubes (filled with neutral gas), raised questions about the nature of this phenomenon. Throughout time, vacuum technology improved, and lower pressure discharges were obtained, allowing to observe rays of current in rarefied gas that travel in straight lines between anode and cathode (in Geissler tubes, the effect was more diffusive due to larger neutral). These new rays were named "cathode rays" by William Crookes [1], who first studied this phenomenon after achieving a higher vacuum in a discharge tube[1].

---

[1]William Crookes observed that "cathode rays" mostly disappear but remain near the anode. Later, Sir J.J. Thomson discovered the nature of cathode rays, consisting of negatively charged discrete particles - named electrons. He used Crookes tubes to discover positively charged particles and formulated one of the

The specific features of ionized gases as a separate state of matter were not recognized until the work of Irving Langmuir and Lewi Tonks. In the 1920s, they studied gas discharges in the tungsten-filament light bulbs (to improve the lifetime of the filament) [2]. They were the first who quantified and acknowledged unique plasma features, such as the notion of quasineutrality, plasma electron waves, and boundary plasma-wall effects called sheaths. These studies were fundamental for plasma physics as we know it today. They also come up with the name plasma, from the Greek word πλασμα – "moldable substance" or "jelly". Imagine a plasma system consisting of heavy ions and electrons. Its tendency to hold quasineutrality creates forces that counteract the inertial motion of light electrons, and thus vibrations of electrons in the effectively stationary ion background resemble jelly-like motion. After that, more objects (new or known before) started to *fit* into the plasma category: Earth's ionosphere, an upper layer of the atmosphere consisting of partially ionized gas (by solar radiation), astrophysical objects, like stars and solar wind. The amount of research in plasma physics scaled up significantly in the mid 20th century, addressing never-ending stability problems in controlled thermonuclear fusion (a concept of the power plant) where hot plasma is confined in strong magnetic fields.

Plasma definition

If we take a gas of charged particles, the interaction between particles is defined by the long-range electromagnetic forces. Here we discuss the criteria that make plasma state and its major properties. Imagine that you have a cloud of heavy and electrically neutral particles that occupy a sphere of radius a. If one injects electrons with sufficient energy ϵ_e into the cloud, successively ionizing heavy particles, the cloud becomes charged to a potential $\phi = Ne/a$ (CGS units), where e is the scalar elementary charge, and N is the number of charged ions. Until $e\phi < \epsilon_e$, electrons can easily escape the volume after an ionization event. After some critical number of neutrals are ionized, $e\phi = \epsilon_e$, electrons can no longer leave the volume. Thus, if we continue the process, we end up with about an equal number of ions and electrons. This leads to the notion of *quasineutrality*, where the whole population of charged

---

first atomic structure models. Another application with huge implications was using vacuum tubes in the early age of digital electronics, before the transistor era.

particles contains about the same number of positive and negative charges [3]. One can estimate the scale on which quasineutrality holds. Given the number density $n = N/(4/3)\pi a^3$, the radius is deduced from $\theta a^2 = \epsilon_e/4\pi n e^2$ (with $\theta = 1/3$). The radius a is called the Debye radius, and commonly denoted as λ_D, is given by

$$\lambda_D = \sqrt{\frac{T_e}{4\pi n_e e^2}}, \tag{1.1}$$

where n_e is the electron density, with the electron temperature $T_e \equiv k_B T_e$ (temperature in plasma conveniently defined in energy units), where k_B is the Boltzmann constant.

One of the main criteria of plasma state is that the spatial extent of plasma L is much larger than the Debye radius, $L \gg \lambda_{De}$; on this scale, the system is quasineutral. For a gas of charged particles $\lambda_D \sim n_e^{-1/2}$, and thus there exist the critical density n for which $L \geq \lambda_{De}$ will hold. Another important property of the Debye radius is that any uncompensated charge "placed" into plasma (or created by random fluctuations) will be screened (shielded) on scales larger than the Debye length; e.g., the potential of a point charge immersed into plasma is $\phi = \phi_0 e^{-r/\lambda_D}$, with $\phi_0 = e/r$ (vacuum potential). It becomes negligibly small (by screening) over distances $r \gg \lambda_D$. Such collective plasma behaviour defines its unique properties and distinguishes it from a simple set of charged particles.

Binary Coulomb interactions in plasma are screened, and particles do not effectively interact with those outside its local Debye sphere. We call such systems weakly coupled (as opposed to configurations where binary collisions dominate). Implications of this are far-reaching in what is generally called the collective behaviour of plasma. Another criterion of weakly-coupled plasma is that the particle kinetic energy must remain larger than the potential energy over the average distance between particles, $r_0 \approx n^{-1/3}$,

$$\frac{e^2}{r_0} \ll \frac{3}{2}T. \tag{1.2}$$

One can see that this condition is equivalent to the requirement that the number of particles in the Debye sphere, $N_D = (4/3)\pi\lambda_D^3 n$, is large. Indeed, Eq. (1.2) states that $N_D^{2/3} \gg 1$.

Numerous laboratory and natural plasma configurations are non-relativistic (typical velocities $v \ll c$) and with negligible quantum effects. Essentially, quantum effects are negligible as the average distance between particles is much larger than the de Broglie wavelength,

$n_0^{-1/3} \gg h/mv$, where m is a particle mass, v is the particle velocity, h is the Planck constant. Substituting the thermal velocity $v_T = \sqrt{2T/m}$, the condition for classical treatment of plasma becomes $T^{3/2}/n \gg h^3/(2m)^{3/2}$. For a given temperature, this condition may break first for light particles such as electrons, for example, in white dwarfs (starts with degenerate electrons).

Based on the above definitions, we assume a weakly-coupled, non-degenerate, and non-relativistic plasma. This includes a wide variety of laboratory and nature plasmas. Such systems are treated classically and, to high accuracy, are described by kinetic plasma theory coupled with classical electromagnetism.

1.3 Electric propulsion and Hall thrusters

Electric propulsion

Electrically powered propulsion uses charged particles as a propellant in external electric and magnetic fields. The main advantage over chemically based propulsion is that a charged propellant can achieve much higher exhaust velocities. It can be demonstrated with a simple force relation acting upon an accelerating object, the generated thrust[2] is $F_T = \dot{m}v_{ex}$, where v_{ex} is the exhaust velocity (assumed constant) and $\dot{m}$ is the mass flow rate. The same thrust values may be obtained with higher v_{ex} and utilizing less propellant, resulting in a better mass efficiency. In fact, the chemical propulsion is limited to exhaust velocities $\sim 5\,$km/s, which imposes restrictions on its applications to long-term space missions, as well as for compact and lightweight satellites (orbital corrections
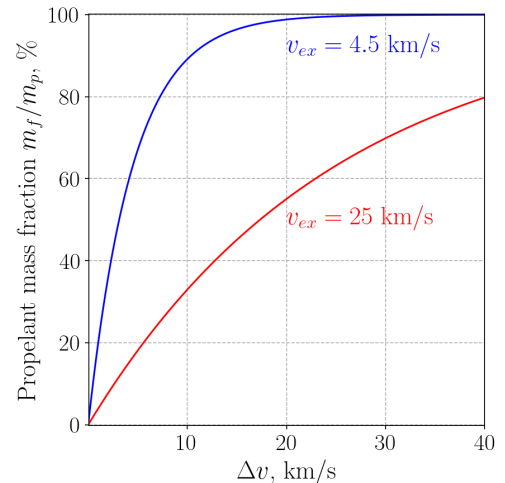
Figure 1.1: Ratio of propellant mass to total rocket mass required to achieve an increment of velocity Δv, given by Tsiolkovsky equation (1.3).

___
[2]Force exerted on a rocket during ejection of propellant by Newton's third law.

and simple maneuvers). Fig. 1.1 demonstrates that larger exhaust velocity ($\sim 25\,\text{km/s}$) allows to carry much less fuel to achieve the same increment in velocity Δv. It is seen via Tsiolkovsky's rocket equation [4, 5]

$$\frac{m_f}{m_p + m_f} = \exp\left(\frac{-\Delta v}{v_{ex}}\right), \tag{1.3}$$

where m_f is the initial fuel mass and m_p is the useful payload. The limitations of electric propulsion mainly consist in the power source that must be carried on the spacecraft. For that reason, electric propulsion operates in relatively low power regimes, with the thrust $\sim 100 mN$ [6], and thus usually requires long times to achieve the desired Δv.

So, how do electric thrusters work? Consider systems that use plasma (consisting of heavy ions and electrons) and work on the electrostatic principle, i.e. acceleration of ions by an electric field. When ionized gas is placed in an external electric field, the work done by the electric field on ions mostly contributes to the thrust, but at the same time, it drives an electron current (moving in the opposite direction), which consumes the supplied power. It is possible to reduce the electron current and its losses by introducing an external magnetic field perpendicular to the motion of ions (and electric field). When the amplitude of the magnetic field is not too high, it can effectively trap electrons (significantly reduce the current along the electric field) while leaving ions effectively unmagnetized (ion gyroradius is larger than the system size). Moreover, in the configuration of crossed $\mathbf{E}$ and $\mathbf{B}$ fields, electrons will drift in the direction perpendicular to both fields, so-called $\mathbf{E} \times \mathbf{B}$ drift. If this direction is closed (e.g., azimuthal), electrons will follow closed trajectories, becoming trapped, with highly reduced motion along the thruster channel.

Hall thrusters

One class of electric propulsion thrusters working on this principle are Hall thrusters. Hall thrusters were originally developed in USSR and USA and applied in practical flights in USSR in the 1970s [7]. In the 1990s, the technology spread worldwide, and active research is ongoing, with numerous modifications and new theoretical insights [8].
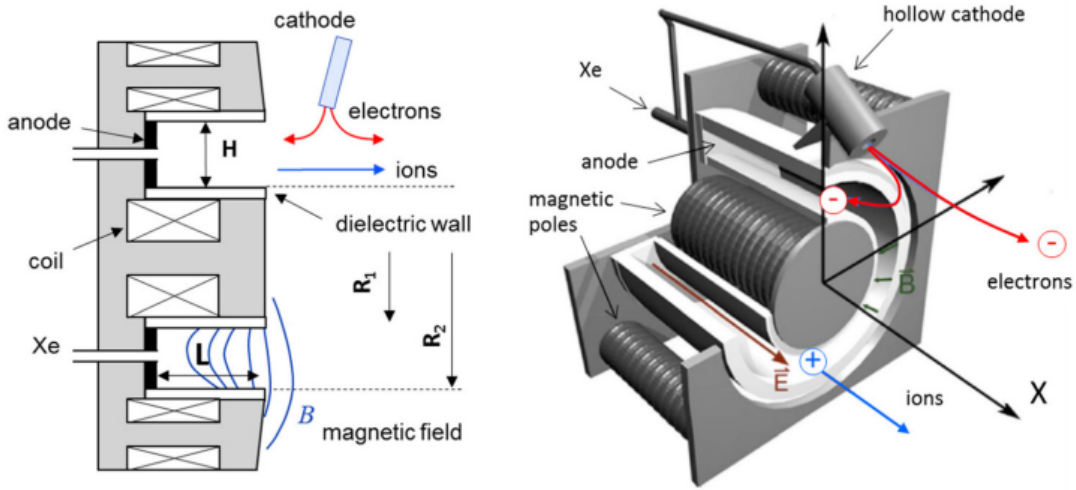
Figure 1.2: Hall thruster schematic [8]. Radial-axial dissection (cut) is shown on the left, and a three-dimensional model on the right.

The schematic of conventional Hall thruster is shown in Fig. 1.2. It contains plasma in the coaxial cylindrical configuration, between two dielectric cylinders, with the anode at the back wall and the cathode electron gun[3] in front of the exit plane. The nearly radial magnetic field lines are created with electromagnets, with the maximum magnetic field lines near the exit plane. Neutral atoms are injected into the near-anode region. With the applied potential difference, the discharge is created and continuously supported by ionization by electron-neutral impact. The cathode serve a dual role: it is a source of electrons in the thruster channel and the charge neutralizer of the output ion beam. A strong magnetic field is used near the channel's exit to confine electrons, increasing their residency time for effective ionization. Low electron conductivity (especially near the exit) leads to the establishment of a bulk electric field in the axial direction. Ions, effectively insensitive to the magnetic field, accelerate by the axial electric field towards the exit and generate thrust. Interestingly, the established electric field is nearly uniform in the azimuthal direction, despite the asymmetric placement of the cathode.

Thus, we have the following degrees of freedom: *axial*, which is parallel to the thruster

---

[3]A thermionic element emits electrons when heated, such as hot metal filament.

motion in space, the direction of the electric field and accelerating ions; it has a physical boundary on one side (anode) and open on the other (channel exit); *azimuthal*, which confines drifting electrons due to the $\mathbf{E} \times \mathbf{B}$ drift and thus sustain high electron current; *radial*, the direction of the magnetic field and bounded with dielectric walls (to suppress the secondary electron emission). In our studies of low-frequency modes of Hall thruster, the axial dynamics is of particular interest; its schematic is shown in Fig. 1.3. As noted above, the plasma discharge is supported by the continuous ionization process, which relies on neutral supply and the applied potential difference (across the channel). All these factors contribute to complex nonlinear dynamics involving three species: neutrals, ions, and electrons. It is also nonlocal via the applied potential constraint.
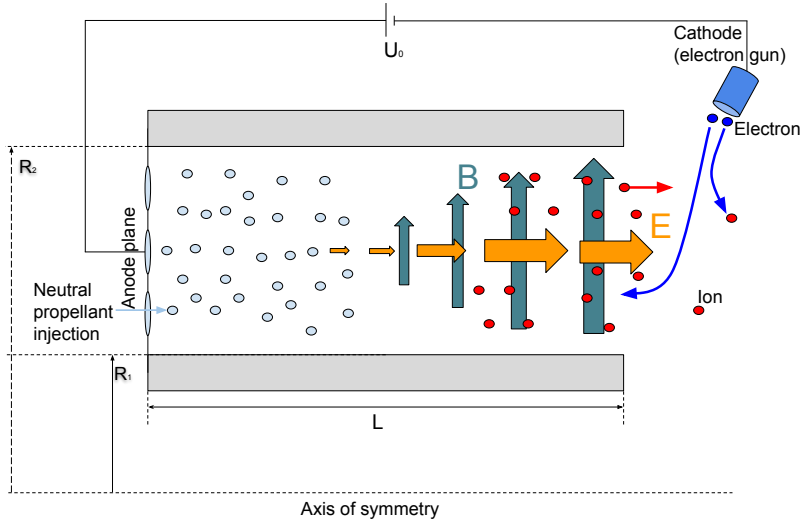
Figure 1.3: Schematic representation of Hall thruster dissected radial-axial plane, with qualitative distributions of particles and fields in the channel. Axial dynamics is highly nonlocal due to applied external potential between anode and cathode.

One of the characteristics of Hall thruster is the presence of turbulence and structures (azimuthal and axial) that affect their operation. In particular, the observed axial electron transport is orders of magnitude larger than the classical collisional transport predicts. The classical transport is due to electron collisions allowing drift in the axial direction (perpendicular to the magnetic field). Estimates for the collisional electron transport are readily

9

obtained from the stationary electron momentum balance equation:

$$0 = -\frac{e}{m_e}(\mathbf{E} + \mathbf{v} \times \mathbf{B}) - \nabla p_e - \nu \mathbf{v_e}, \tag{1.4}$$

where $\mathbf{E} = E\hat{\mathbf{e}}_x$ is along the axial direction, $\mathbf{B} = B\hat{\mathbf{e}}_r$ is the radial magnetic field; ν is the total electron collision frequency (mainly due to electron-neutral collisions), $\mathbf{v}_e$ is the electron flow velocity. Then the axial electron flow velocity is

$$v_x = -\mu_e E - \frac{\mu_e}{n}\frac{\partial p}{\partial x}, \tag{1.5}$$

where μ_e is the classical expression for the electron mobility across the magnetic field:

$$\mu_e = \frac{e}{m\nu}\frac{1}{1 + \omega_{ce}^2/\nu^2}, \tag{1.6}$$

where $\omega_{ce} = eB/m_e$ is the electron cyclotron frequency. In the region of the high magnetic field, $B \approx 150\,\mathrm{G}$ and $\omega_{ce} \approx 1{\times}10^9\,\mathrm{s}^{-1}$, while $\nu \approx 5{\times}10^6\,\mathrm{s}^{-1}$, thus the so-called Hall parameter $h = \omega_{ce}/\nu \gg 1$ is typical for a Hall thruster setup. Thus, for a large Hall parameter Eq. (1.4) predicts

$$\mu_e \sim \frac{1}{B^2}, \tag{1.7}$$

which is the classical transport for electrons; it appears that the modest values of B could effectively entrap electrons.

Even in early experiments with Hall thrusters, it was noted that the measured electron current exceeds the classical values by few orders [6], and the exact mechanisms involved are not clear. Possible explanations are electron-wall collisions and turbulent electron transport. Turbulence-related transport is likely due to instabilities developing in azimuthal direction: low-frequency spoke phenomena [9] and high-frequency magnetized drift instabilities excited by strong $\mathbf{E}{\times}\mathbf{B}$ electron currents [10]. Then, the fluctuating azimuthal electric field $\widetilde{\mathbf{E}} = \widetilde{E}_\theta\hat{\mathbf{e}}_\theta$ can push the axial current via the $\widetilde{\mathbf{E}} \times \mathbf{B}$ drift (given a non-zero correlation between $\widetilde{E}_\theta$ and the electron density fluctuation $\widetilde{n}_e$ [11]). To account for the anomalous parts of the electron current, the Bohm diffusion [12] is used, giving the mobility expression

$$\mu_B = \frac{1}{16B}, \tag{1.8}$$

where the factor $1/16$ was obtained empirically. The Bohm diffusion is often included in Hall thruster models, as used in our models in Chapters 2 and 3. The Bohm anomalous frequency

$$\nu_B = \frac{\beta e}{16 m_e} \frac{1}{B}, \tag{1.9}$$

is added to the total electron momentum exchange frequency ν, with the parameter β to control the anomalous contribution. In this way the total frequency ν accounts for contributions from different factors, including collisions with neutrals, wall collisions, etc.

Accurate models for the electron transport from first principles must likely include two or all three dimensions, electron inertia effects. Due to the general problem of scale separation, high computational costs, and potential numerical problems, phenomenological description of electron transport is a typical choice for reduced models.

1.4   Magnetic mirror for thermonuclear fusion

Thermonuclear Fusion

Thermonuclear fusion is a nuclear reaction when a few atomic nuclei are merged into one (or, at least, a smaller amount of) nuclei that are chemically different from the initial reactants. Suppose the nuclear binding energy of the product (per nucleus) is larger than that of reactants. This leads to the mass defect, the product mass is smaller than the sum of reactants masses. The excess energy is released in some form (gamma radiation, the kinetic energy of byproduct, etc.), with the amount corresponding to $E = m_d c^2$, where m_d is rest "defect" mass, c is the speed of light. Fusion reactions associated with the energy release (exothermic) involve lightweight reactants, so the atomic number of a resulting product is 26 (iron) or smaller; for the heavier products binding energy start to decrease (due to effective nucleus size grows, see the nuclear binding energy curve [13]). The reverse nuclear reaction is known as fission which has been successfully utilized by existing nuclear power plants since the 1950s.

Fusion is both one of the fascinating natural phenomena (as the energy source for stars) and a very challenging applied physics and engineering pursuit which run since the late 1950s (for peaceful applications to build controllable energy plants). The main difficulty from a physics standpoint arises from overcoming the repulsive Coulomb interaction of reactants;

they need to get close, at distances where the strong nuclear force begins to take effect, at $\sim 10^{-15}$ m. For example, to bring two protons to the distance 10^{-15} m, one needs the energy of $\sim 10 \, \text{keV}$ to overcome the Coulomb force. At the same time, it is not enough just to reach this energy, the probability of Coulomb scattering dominates over fusion cross-sections in the whole energy spectrum. Therefore, one must confine hot plasma long enough for a sufficient number of fusion reactions and positive power outputs. Indeed, successful confinement is the main difficulty for fusion devices.

Controlled fusion is one of the important applications of laboratory plasma physics. Several configurations were proposed based on magnetic, inertial, or electrostatic plasma confinement. One of the promising approaches is the magnetic confinement that uses a magnetic field as a wall-less barrier that keeps hot charged particles (plasma) away from the material walls. Main configurations for magnetically confined systems can be categorized as systems with open or closed magnetic field lines[4]. Closed systems, for example, are the torus-shaped tokamak and stellarator with the predominantly toroidal magnetic field with some additional poloidal magnetic field to suppress hydrodynamic instabilities [14]. Generally speaking, closed systems are advantageous for confinement since transport in the perpendicular (to magnetic field) direction is suppressed for magnetized particles. In an open system the magnetic field leaves the confinement volume thus resulting in large losses along the field lines. At the same time, open ends allow to naturally extract power from such devices. The magnetic mirrors flaring towards end walls also serve an additional purpose to reduce and control heat load per unit of area by expanding the plasma flow over the larger region.

Plasma flow escaping the magnetic mirror accelerates ions to supersonic speeds. The direct plasma-wall contact with the end structures (walls) may pollute the divertor region by slow neutral atoms. Such atom sources can affect the whole operation of the device by generating slow ion and electron sources. This scenario is studied in Chapter 4 of this thesis. Thus, we briefly discuss the physics of magnetic mirror configuration, plasma acceleration through the magnetic mirror, and possible effects due to neutral sources.

---

[4]Physically, all magnetic field lines closed as per $\nabla \cdot \mathbf{B} = 0$, here the closed magnetic configuration means that the magnetic field lines are closed within the volume of a device.
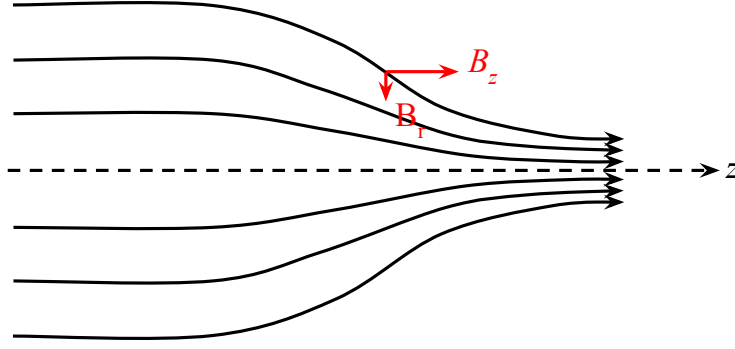
Figure 1.4: Converging magnetic field lines in configuration of magnetic mirror with the most intense field on the right (magnetic throat).

Plasma flow in magnetic mirror

The magnetic mirror is a magnetic field configuration with converging magnetic field lines, Fig. 1.4. Particles moving to the region of the stronger field in this configuration can be reflected purely by the magnetic (Lorentz) force (parallel energy transforms to perpendicular, effectively slowing down parallel motion). The symmetric configuration with mirrors on both ends is called the magnetic trap; it can effectively confine charged particles[5]. It is worth mentioning that the reversed configuration (diverging magnetic field) is known as the magnetic nozzle and is used in electric propulsion applications, e.g. VASIMR rocket [15], it converts the thermal energy of charged particles into parallel motion, thus generating thrust[6]. A charged particle in a sufficiently strong magnetic field characterized with magnetic moment μ as the integral of motion [14]

$$\mu = mv_\perp^2/2B = \text{const}, \tag{1.10}$$

where m is the mass of a charged particle, $v_\perp$ its perpendicular velocity, and B is the magnitude of a magnetic field. The magnetic moment is well conserved when the Larmor radius of a particle is much smaller than the gradient length of magnetic field $L_B = (|\nabla B|/B)^{-1}$,

---

[5]It applies only to single particles that do not resemble collective effects; it is shown further that plasma is not confined in the standard magnetic trap.

[6]Similarly to de Laval nozzle for neutral gas.

i.e. when the magnetic field does not change significantly per one gyro-rotation [14]. Then the total kinetic energy

$$\varepsilon = \frac{m}{2}\left(v_\perp^2 + v_z^2\right) = \frac{mv_z^2}{2} + \mu B = \text{const},\tag{1.11}$$

where v_z is the parallel velocity; it is seen that the quantity μB plays a role of potential energy if we consider dynamics along to the magnetic field line. If a particle moves in the direction of stronger B, its parallel energy decreases, and depending on its initial energy ε_i and the value of μ. The particle can be even reflected, if the following condition is satisfied:

$$\frac{mv_z^2}{2} = \varepsilon_i - \mu B < 0,\tag{1.12}$$

which is similar to the classical result for a particle trapped in a potential well (maximum of μB must be larger than the initial energy), where potential energy is μB, but with the important difference that this quantity depends on particle's initial (perpendicular) velocity. In the coordinates of initial parallel and perpendicular velocities $(v_{\perp 0}, v_{z0})$, the condition (1.12) describes the so-called loss cone, i.e. the region of initial velocities that will lead to a loss (reciprocal region leads to reflection, and thus confinement), which is

$$v_{\perp 0}^2 < v_{z0}^2 \left(1 - \frac{B_{\text{max}}}{B_0}\right)^{-1},\tag{1.13}$$

where B_0 is the magnetic field at point entry (would be the minimum value if the injection is in the middle of magnetic trap), and the B_{max} is the maximum value of magnetic field (throat of the magnetic mirror), $R \equiv B_{\text{max}}/B_0$ is the magnetic mirror ratio.

Now, if the configuration of the magnetic trap is used to confine plasma (which is the case for highly ionized and hot gas), collective effects will play a crucial role. One may think that particles could bounce between two ends of the trap, losing only particles in the loss cone, and eventually, losses will stop. But binary collisions in plasma will scatter particles into the loss cone. Estimates show [16] that the Coulomb electron-electron collisions are $\sqrt{m_i/m_e}$ more frequent, and they effectively become isotropic, thus continuously filling the loss cone. This leads to higher electron losses and the ambipolar electric field rising to keep plasma quasineutrality. The electric field slows down electron losses but increases ion losses (it is shown below how the loss cone is modified in the presence of an electric field). The Boltzmann

approximation for electrons gives a good estimate for the electrostatic field appearing in this case; it is derived from the electron momentum balance equation with the electron inertia neglected:

$$0 = en_e \nabla_z \phi - T_e \nabla_z n_e, \tag{1.14}$$

where the force due to density gradient is compensated by the electric field force, so there is no net electron current. With plasma quasineutrality we have $n = n_i = n_e$, and integrating Eq. (1.14), the potential along the magnetic field line is $e\phi(z)/T_e = \ln n(z) - \ln n(0)$ (setting $\phi(0) = 0 \, \text{V}$). Depending on the magnetic mirror ratio, plasma density may drop about 1-2 orders crossing the throat of the mirror [17], and thus potential difference may reach few electron temperatures T_e/e (e.g., $\Delta\phi \approx 700 \, \text{V}$ for $T_e = 200 \, \text{eV}$ with $R = 7$, and system length $3 \, \text{m}$, as shown in the numerical simulations in Chapter 4). The electrostatic electric field is conservative, $E_z = -\nabla_z \phi$, thus the condition (1.12) modifies to

$$\frac{m_i v_z^2}{2} = \varepsilon_i - e\phi - \mu B < 0, \tag{1.15}$$

where the quantity $U_{\text{eff}} = e\phi + \mu B$ is often called the effective (or Yushmanov) potential. Note, in Eq. (1.15) we assumed an ion particle (positively charged) with the mass m_i. Thus, the particle is trapped if $\varepsilon_i < U_{\text{eff}}$, which depends on both B and ϕ profiles. The loss boundary with the conic shape becomes a more complicated surface, given by

$$v_{\perp 0}^2 < \left(v_{z0}^2 + \frac{2e\Delta\phi(z')}{m_i} \right) \left(1 - \frac{B(z')}{B_0} \right)^{-1}, \tag{1.16}$$

where z' is the location of the maximum of U_{eff}. As discussed above, the faster electron losses lead to the potential that reduces these losses. Thus, one should consider $\Delta\phi(z') < 0$ in Eq. (1.16). The schematic representation of loss and trapped regions for positively charged particles in velocity space is shown in Fig. 1.5. While the loss cone is the same irrespective of the sign of the charge, the electric field expands the ion loss region and shrinks that of electrons.

In full generality, with the thermal spread of particle energies, the kinetic (or drift-kinetic) description of plasma flow through magnetic nozzle requires numerical treatment. It cannot be analytically obtained even with the Boltzmann electron model (1.14), and the assumption of quasineutrality. Indeed, the electrostatic potential can be integrated only when the density
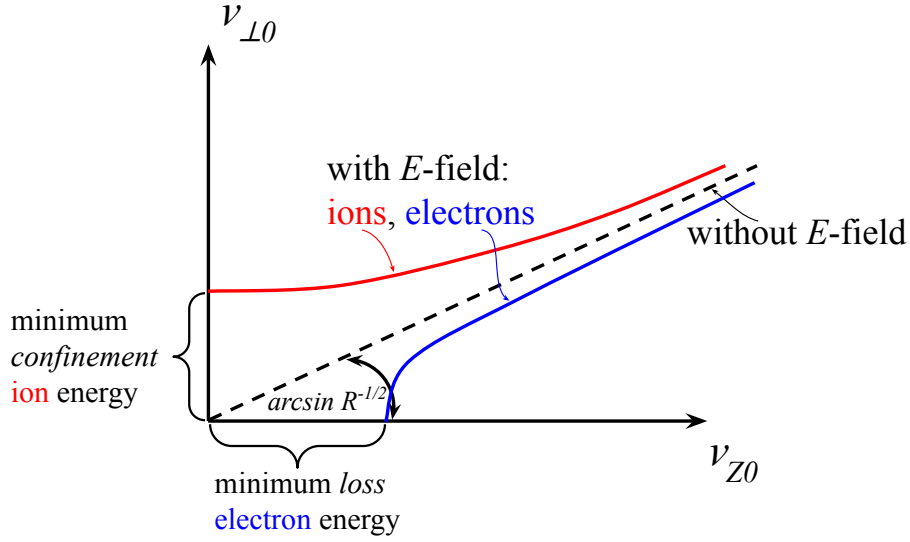
Figure 1.5: Schematic representation of regions for lost and trapped positively charged particles in absence of electric field (standard loss cone), and in presence of electric field.

is known, and the density is evaluated from microscopic particle's position that requires the potential for integration of motion (and accurate account of escaped or reflected particles of different energy). In literature, this was addressed, for example, with a drift-kinetic stationary model with $\mu = \text{const}$ using an iterative approach [18] or time-dependent particle-in-cell [19]. Our model of Chapter 4 is time-dependent and based on drift-kinetic ions (particle-in-cell), Boltzmann electrons, and full quasineutrality assumption. It also includes the model of atom transport (due to ions bombarding the wall) and collisions due to charge exchange (ion-neutral) and ionization (electron-neutral).

Analytical solutions, however, have been obtained for the cold fluid theory. The stationary ion momentum equation can be written in the form [17]

$$\left(M^2 - 1\right) \frac{\partial M}{\partial z} = -M \frac{\partial \ln B}{\partial z}, \tag{1.17}$$

where $M = V_i/c_s$, the ion flow velocity V_i normalized on the ion sound speed $c_s = \sqrt{T_e/m_i}$ (constant for isothermal electrons). The right-hand side of Eq. (1.17) represents the effect of the guiding magnetic field acting equivalently to de Laval nozzle's variable cross-section area. Continuous solutions to Eq. (1.17) are obtained with the regularization condition that states that both $\partial \ln B / \partial z = 0$ and $M^2 - 1 = 0$ must hold at the transition point. This
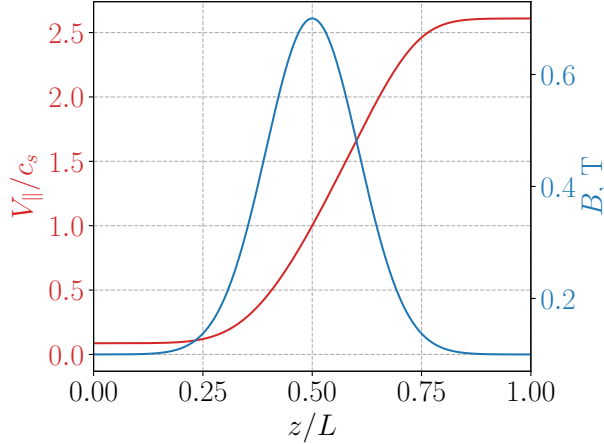
Figure 1.6: Magnitude of axial magnetic field in configuration of magnetic nozzle. Ion velocity profile is shown as solution to Eq. (1.17)

defines the location of the sonic point ($M = 1$), which is tied to the extrema (maximum) of the magnetic field. The example of the magnetic field profile and the corresponding solution to Eq. (1.17) are shown in Fig. 1.6.

In Chapter 4 we show that the presence of neutrals and collisions in the near-wall region will strongly affect the plasma flow accelerated through the magnetic mirror. Additional plasma sources near the wall contribute to an overall drop in potential difference and can even excite streaming instabilities. Understanding the main mechanisms behind these effects is essential, as they may significantly impact the overall fusion device operation.

1.5 Plasma models

1.5.1 Kinetic description

It was pointed out that in weakly coupled plasma $N_D \gg 1$ and $L \gg \lambda_D$, the number of particles is enormous, it allows to use the statistical approach to describe discrete particles with the continuum distribution function $f(\mathbf{x}, \mathbf{v}, t)$ defined as a number of particles per phase space volume $d\mathbf{x}d\mathbf{v}$. The phase space volume $d\mathbf{x}d\mathbf{v}$ considered here is physically small; it still must contain a large number of particles, so the fluctuations are small due to the change of the number of particles. The evolution of the distribution function in time gives the most accurate statistical description of the plasma system (exactly tracking every particle in

phase space is impractical for analysis or numerical treatment). Then the total change of the distribution function in time is given by the Boltzmann equation

$$\frac{\mathrm{d}f_\alpha(\mathbf{x}, \mathbf{v}, t)}{\mathrm{d}t} = \mathrm{C}_{coll}(f_\alpha), \tag{1.18}$$

where α denote species type (e.g. electrons, ions), C_{coll} is a collision operator. A simple form for C_{coll} in the presence of collisions with neutral atoms

$$\mathrm{C}_{coll} = \nu \left(f_0 - f_\alpha \right), \tag{1.19}$$

called the Krook collision operator, where ν is the average collision frequency, f_0 is an equilibrium distribution function.

The total time derivative is obtained via the chain rule as

$$\frac{\mathrm{d}}{\mathrm{d}t} = \frac{\partial}{\partial t} + \frac{\mathrm{d}\mathbf{x}}{\mathrm{d}t} \cdot \frac{\partial}{\partial \mathbf{x}} + \frac{\mathrm{d}\mathbf{v}}{\mathrm{d}t} \cdot \frac{\partial}{\partial \mathbf{v}}, \tag{1.20}$$

where the characteristics $\mathrm{d}\mathbf{x}/\mathrm{d}t = \mathbf{v}$, $\mathrm{d}\mathbf{v}/\mathrm{d}t = \mathbf{F}/m_\alpha$ given by the classical equations of motion. In the case where collisions are negligible, $\mathrm{C}_{coll} = 0$, one obtains the Vlasov equation:

$$\frac{\partial f_\alpha}{\partial t} + \mathbf{v} \cdot \frac{\partial f_\alpha}{\partial \mathbf{x}} + \frac{q_\alpha}{m_\alpha} \left(\mathbf{E} + \frac{\mathbf{v}}{c} \times \mathbf{B} \right) \cdot \frac{\partial f_\alpha}{\partial \mathbf{v}} = 0, \tag{1.21}$$

where the macroscopic electromagnetic fields $\mathbf{E}$ and $\mathbf{B}$ satisfy Maxwell equations:

$$\nabla \cdot \mathbf{E} = 4\pi\rho, \tag{1.22}$$

$$\nabla \cdot \mathbf{B} = 0, \tag{1.23}$$

$$\nabla \times \mathbf{E} = -\frac{1}{c}\frac{\partial \mathbf{B}}{\partial t}, \tag{1.24}$$

$$\nabla \times \mathbf{B} = \frac{4\pi}{c}\mathbf{J} + \frac{1}{c}\frac{\partial \mathbf{E}}{\partial t}. \tag{1.25}$$

The system of equations (1.21-1.25) is known as the Vlasov-Maxwell system. The coupling is due to the charge density $\rho(\mathbf{x}, t)$ and the current density $\mathbf{J}(\mathbf{x}, t)$ evaluated from the first moments of the distribution function f_α. The charge density can be found by summation:

$$\rho(\mathbf{x}, t) = \sum_{\alpha=i,e} q_\alpha n_\alpha(\mathbf{x}, t), \tag{1.26}$$

where the number density n_α is evaluated by integrating the distribution function over the entire velocity space:

$$n_\alpha(\mathbf{x}, t) = \int_{\mathbf{v}} f_\alpha(\mathbf{x}, \mathbf{v}, t) \mathrm{d}^3 v. \qquad (1.27)$$

The current density $\mathbf{J}(\mathbf{x}, t)$ is

$$\mathbf{J}(\mathbf{x}, t) = \sum_{\alpha=i,e} q_\alpha n_\alpha(\mathbf{x}, t) \mathbf{V}(\mathbf{x}, t) = \sum_{\alpha=i,e} q_\alpha \int_{\mathbf{v}} \mathbf{v} f_\alpha(\mathbf{x}, \mathbf{v}, t) \mathrm{d}^3 v, \qquad (1.28)$$

where $\mathbf{V}(\mathbf{x}, t)$ is the average flow velocity.

1.5.2 Fluid description

Full kinetic treatment achieved with the Vlasov-Maxwell system (1.21) is often difficult for analytical and numerical treatment. Also, the evolution of the distribution function in six-dimensional phase space may be too detailed for some problems. The reduced treatment exists in terms of the fluid equation, describing the evolution of macroscopic plasma quantities. The fluid reduction is formally obtained by taking the successive moments of the Boltzmann equation,

$$\int_{\mathbf{v}} [x] \frac{\mathrm{d} f_\alpha(\mathbf{x}, \mathbf{v}, t)}{\mathrm{d} t} \mathrm{d}^3 v = \int_{\mathbf{v}} [x] \mathrm{C}_{coll}(f_\alpha) \mathrm{d}^3 v, \qquad (1.29)$$

weighted with the physical quantities $[x]$, and allows to evaluate average macroscopic quantities, such as number density, $[x] = 1$, velocity, $[x] = \mathbf{v}$, pressure $[x] = mv'^2$ (here v' is the random component of the velocity, defined below), etc. During integration of Eq. (1.29), three-dimensional velocity space averages out. Thus, some effects associated with velocity space (commonly called as kinetic effects) are missing. This procedure results in an infinite hierarchy of partial differential equations (in time and space) for macroscopic quantities. For collisionless plasma, $\mathrm{C}_{coll}(f_\alpha) = 0$, integrating Eq. (1.29) with $[x] = 1$, we obtain the continuity equation for the number density $n(\mathbf{x}, t)$ (index α is further omitted):

$$\frac{\partial n}{\partial t} + \nabla \cdot n\mathbf{V} = 0, \qquad (1.30)$$

and, the next moment with $[x] = \mathbf{v}$, the conservation of momentum [20]

$$mn \left(\frac{\partial \mathbf{V}}{\partial t} + \mathbf{V} \cdot \nabla \mathbf{V} \right) = -\nabla \cdot \mathbf{\Pi} + en \left(\mathbf{E} + \frac{\mathbf{V}}{c} \times \mathbf{B} \right), \qquad (1.31)$$

19

where $\mathbf{\Pi}$ the total stress tensor, given by

$$\mathbf{\Pi} = m \int_{\mathbf{v}} \mathrm{d}^3 v \ \mathbf{v}' \mathbf{v}' f, \tag{1.32}$$

with the microscopic random velocity $\mathbf{v}' = \mathbf{v} - \mathbf{V}$; here $\mathbf{v}$ is the microscopic velocity and $\mathbf{V}$ is the average (flow) velocity. One can expand the total stress tensor into components:

$$\mathbf{\Pi} = p\mathbf{I} + \boldsymbol{\pi}, \tag{1.33}$$

where $\boldsymbol{\pi}$ is the stress tensor

$$\boldsymbol{\pi} = m \int_{\mathbf{v}} \mathrm{d}^3 v \ \left(\mathbf{v}' \mathbf{v}' - \frac{1}{3} v'^2 \right) f, \tag{1.34}$$

and p is the scalar pressure. Thus, the total stress tensor is decomposed on the scalar pressure p (accounts for diagonal elements of $\mathbf{\Pi}$) and the stress tensor π (off-diagonal). Then, the conservation of momentum is written as

$$mn \left(\frac{\partial \mathbf{V}}{\partial t} + \mathbf{V} \cdot \nabla \mathbf{V} \right) = -\nabla p + en \left(\mathbf{E} + \frac{\mathbf{V}}{c} \times \mathbf{B} \right) - \nabla \cdot \boldsymbol{\pi}, \tag{1.35}$$

The moment equation for evolution of the scalar pressure p is found with $[x] = mv'^2$ and given by [20]:

$$\frac{3}{2} \frac{\partial p}{\partial t} + \frac{3}{2} \mathbf{V} \cdot \nabla p + \frac{5p}{2} \nabla \cdot \mathbf{u} = -\boldsymbol{\pi} {:} \nabla \mathbf{u} - \nabla \cdot \mathbf{q}, \tag{1.36}$$

where $\mathbf{q}$ is the heat flux, and represent the next (higher order) moment variable. For the consistency, the definitions of the macroscopic variables defined above are

$$n = \int_{\mathbf{v}} \mathrm{d}^3 v \ f, \tag{1.37}$$

$$\mathbf{V} = \frac{1}{n} \int_{\mathbf{v}} \mathrm{d}^3 v \ f \mathbf{v}, \tag{1.38}$$

$$p = \frac{1}{3} \int_{\mathbf{v}} \mathrm{d}^3 v \ f v'^2, \tag{1.39}$$

$$\mathbf{q} = \int_{\mathbf{v}} \mathrm{d}^3 v \ f \frac{m v'^2}{2} \mathbf{v}'. \tag{1.40}$$

Often, to model lower frequency dynamics in unmagnetized plasma (or along magnetic field lines), there is no need for detailed resolution of electron motion, thus neglecting the electron inertia effects. Then the stationary electron momentum balance equation gives

$$0 = -\nabla p_e + en_e \nabla \phi, \tag{1.41}$$

20

where $E = -\nabla\phi$; which describes equilibrium of electron current due to pressure gradient and electric field forces. In this approximation, electrons instantaneously respond to the combination of these forces and perfectly balance them out. For the isothermal electrons, one can integrate it

$$n_e = n_{0e} \exp \frac{e\phi}{T_e}, \qquad (1.42)$$

where n_{0e} is the constant of integration. The Boltzmann approximation for electrons has been used in Chapter 4 for modeling electrons in the magnetic mirror (along field lines). A more detailed, magnetized form of Eq. (1.41) that also includes the friction term due to collisions has been utilized in the low-frequency model of Hall thrusters in Chapters 2 and 3.

1.6 Numerical methods

Nowadays, numerical simulations are widely used in plasma physics research. Simulations accompany almost all newly published works in plasma physics, not least due to the general complexity of plasma systems. Simulations can give a greater insight into plasma processes than experiments and are used for prototyping and testing new or modified devices.

1.6.1 Kinetic methods

Solving the Vlasov-Maxwell system (1.21-1.25) gives most complete descriptions of plasma. Direct methods solving for the continuum distribution function in discretized phase space, e.g. with the finite differences [21], or expanding the distribution function with spectral representation in velocity space [22, 23]. But the most popular and very robust method is a particle method, called particle-in-cell (PIC). In PIC, plasma species are simulated as particles carrying the artificial weight; each particle represents some number of real particles and is called a macroparticle (for brevity, we will use particle). The particle's trajectories evolve in the continuous phase space, and their dynamics are described by the classical equations of motion (the characteristics of the Vlasov equation):

$$\frac{d\mathbf{x}}{dt} = \mathbf{v}, \quad \frac{d\mathbf{v}}{dt} = \frac{q}{m}\left(\mathbf{E} + \mathbf{v} \times \mathbf{B}\right). \qquad (1.43)$$

While using the artificial weight reduces the number of simulation particles, calculating all binary electromagnetic forces would be too expensive. Thus, the corresponding electromagnetic fields in PIC are obtained from the Maxwell equations and solved on the grid, elegantly combining Lagrangian and Eulerian approaches. The source terms $\rho = e(n_i - n_e)$, $\mathbf{J} = e(n_i \mathbf{V}_i - n_e \mathbf{V}_e)$ are evaluated on the grid from the microscopic coordinates and velocities, and Maxwell equations (1.22-1.25) are solved for $\mathbf{E}, \mathbf{B}$ fields. The interpolation functions used for evaluation of $\rho, \mathbf{J}$ give particles a "shape" (and finite-size) as seen by the field solver on the grid. The finite size of particles eliminates the problem of the singular potential of point sources with potential $\phi \sim 1/r$.

The described PIC algorithm, in principle, tracks the exact trajectories of particles in plasma. In fusion applications, for highly magnetized charged particles, a simplified gyrokinetic approach is often used. The simplification is achieved by averaging over the fast gyrofrequency, and thus equations of motion (1.43) are averaged removing the gyrophase angle [24]. Another simplification is possible when the effects of finite gyroradius are also neglected leading to the drift-kinetic model. In this thesis, in Chapter 4, we apply a drift-kinetic model for ions in plasma for magnetic mirror configuration.

The PIC method was invented in Los Alamos National Laboratory, originally applied to hydrodynamic problems [25], where combining of the Lagrangian and Eulerian approach (utilizing advantages of both) was beneficial in resolving shock-wave structures [26]. PIC gained popularity for plasma simulations after successful demonstration of the Landau damping effect preceding its experimental evidence [27]. Since the very first work [25], it is pointed out that the lack of macroparticles leads to a high level of statistical noise (especially due to a limited amount of computational resources at the time). Indeed, the statistical noise in PIC is one of its major drawbacks[7], as the level of noise scales with a number of particles in cell N_c as $\sim 1/\sqrt{N_c}$. It can lead to inaccurate results in capturing pure kinetic effects, such as wave-particle resonances in a developing instability [30].

---

[7]The main techniques for noise reduction include so-called cold start: instead of using pseudo-random number sequence, sampling of initial phase space information is done with the low-discrepancy sequences (not without its "side-effects") [28]. Another recently adopted technique is the delta-f method, which consists of augmenting particle approach with continuum method for equilibrium distribution [29].

1.6.2   Fluid methods

Fluid modeling is often useful for macroscopic global simulations of plasma; its reduced form and lower dimensionality allow for faster simulations. It can also be advantageous to use a "flexibility" of fluid equations: physical effects are easily added or removed. For example, in Chapter 3 we were able to strip off the fluid model to a much simpler set of equations (continuity equations), which gave a better insight into the problem. At the same time, a lack of some effects cannot be simply observed, and a good physical intuition is required behind using fluid modeling of plasma.

For studies presented in this work, namely in Chapters 2 and 3, BOUT++ computational framework [31] was used for fluid modeling. It is free and open-source project, developed continuously by a number of contributors [32], originating in Lawrence Livermore National Laboratory. BOUT++ is a modular code for solving an arbitrary number of three-dimensional partial-differential equations (PDE). It supports curvilinear geometry and relies on finite-difference methods [31, 33]. Time integration of PDE in BOUT++ is based on the method of lines (MOL). MOL consists of two main steps: discretization (approximation) of spatial derivatives and then time integration of resulting ordinary-differential equations (ODEs) along with boundary conditions, resulting in a differential-algebraic system. Spatial derivatives are approximated with finite-difference (FD) methods. These include central derivatives, upwinding schemes in each dimension separately, and flux conserving schemes, all of up to 4th order. BOUT++ includes various implicit, explicit, and implicit-explicit schemes among ODE integrators. One commonly used and robust ODE integrator is the CVODE solver from the SUNDIALS package[34], with variable-order, variable-step multistep methods suitable for stiff and nonstiff problems. The CVODE solver was used to solve the fluid equations for Hall thruster models, presented in Chapters 2 and 3.

1.6.3   Hybrid and quasineutral models

Reduction to fluid equations effectively decreases the number of degrees of freedom (compared to kinetic representations) and simplifies the analysis or numerical treatment. Nevertheless, kinetic effects may play a substantial role in some problems (beam instabilities, resonance

wave-particle effects). Thus, in some models coupling between different approaches is done for different plasma species. In Chapter2 we utilized a hybrid model for a Hall thruster simulation, where heavy species (ions and atoms) were modeled with the kinetic approach (PIC), and electrons described with the fluid model. Later, in Chapter4, a similar approach was employed for the configuration of plasma acceleration in a large-scale magnetic mirror.

For large-scale electrostatic problems, where the Debye length λ_D is small compared to the plasma dimensions, and there is no particular interest in the microscopic phenomena, it is common to use the quasineutrality assumption, $n_e = n_i$. Instead of the Poisson equation, the electric field can be deduced e.g. from the electron fluid equations. Since the electron density n_e is known, the electric field becomes the unknown quantity in the set of electron fluid equations [35]. By neglecting the smallest plasma scale $\sim \lambda_D$, we also neglect the electron inertial motion and assume that electrons (immediately) re-position in a way to balance out currents and satisfy quasineutrality. Up to high accuracy, it holds on average over time scale $\omega \ll \omega_{pe}$. Therefore, the quasineutral approximation is typically used in the low-frequency models (called plasma approximation [14]). The obvious drawback of such an approach is the inability to resolve the sheath potentials, which are inherently non-quasineutral. It requires additional analytical approximations added to the potential boundary conditions. Numerically, quasineutral models are advantageous; they eliminate computational time constraints posed on the small electron time scale while remaining explicit. It is suggested that a practically useful alternative is a semi-implicit method for the Poisson equation, stable irrelative to the resolved time and spatial domain [35] (if Debye length is not resolved, the sheath potential drop occurs on the order of discretization size).

CHAPTER 2

FLUID AND HYBRID SIMULATIONS OF THE IONIZATION INSTABILITIES IN HALL THRUSTER

2.1 Preface

Low-frequency axial modes of ionization nature in Hall thrusters are observed in most experiments. Predictive models that recover these modes are important from an engineering standpoint and serve as a research tool in plasma physics. Time-dependent nonlocal and nonlinear phenomena often can only be solved with numerical simulations. In this work, two reduced models, fluid and hybrid, are compared against each other in a series of experiments. The parameters of the model correspond to the benchmark project LANDMARK [36], which provides the set of parameters for the reduced fluid and hybrid models based on experimental benchmarks. In this work, we identify various regimes of breathing modes, give their main characteristics, and discuss major differences between the models. The publication is prepared based on the material of this Chapter; its preprint is available in arXiv [37]. Note that there are Appendices associated with this publication; they are presented at the end of this Chapter.

2.2 Abstract

Low-frequency axial oscillations in the range 5-50 kHz stand out as a pervasive feature observed in many types of Hall thrusters. While it is widely recognized that the ionization effects play the central role in this mode, as manifested via the large-scale oscillations of neutral and plasma density, the exact mechanism(s) of the instabilities remain unclear. To

gain further insights into the physics of the breathing mode and evaluate the role of kinetic effects, a one-dimensional time-dependent full nonlinear low-frequency model describing neutral atoms, ions, and electrons, is developed in full fluid formulation and compared to the hybrid model in which the ions and neutrals are kinetic. Both models are quasineutral and share the same electron fluid equations that include the electron diffusion, mobility across the magnetic field, and the electron energy evolution. The ionization models are also similar in both approaches. The predictions of fluid and hybrid simulations are compared for different test cases. Two main regimes are identified in both models: one with pure low-frequency behavior and the other one, where the low-frequency oscillations coexist with high-frequency oscillations in the range 100-200 KHz, with the characteristic time scale of the ion channel flyby time, 100-200 kHz. The other test case demonstrates the effect of a finite temperature of injected neutral atoms, which has a substantial suppression effect on the oscillation amplitude.

2.3 Introduction

Hall thrusters are successfully used for electric propulsion in space, e.g. for satellite orbit keeping, and becoming an enabling technology of choice for long-term missions, such as trips to Mars. Despite the relatively long history of practical use (since 1972 [7]), the crucial physical aspects of their operation are poorly understood. In the absence of predictive modeling capabilities, scaling of these devices for large (e.g., for long-term missions) and for low (for microsatellites) power is very difficult and expensive. The quantitative understanding of the physics of these devices remains an important task.

The plasma discharge in Hall thrusters is supported by the electrons drifting in the closed (periodic) azimuthal E × B direction. At the same time, ions create the thrust (effectively unmagnetized due to large gyroradius) accelerated by the electric field in the axial direction. One of the characteristics of Hall thrusters is the presence of turbulence and structures (azimuthal and axial) that affect their operation. Studies of nonlinear phenomena in these plasmas are of great practical importance and address fundamental problems of plasma physics and plasma turbulence. In particular, the turbulent electron transport in such devices is

orders of magnitude larger than the classical collisional transport (across the magnetic field) predicts. Inhomogeneous plasmas with $E \times B$ electron drift are typically prone to various drift instabilities, both due to the fluid [38] and kinetic mechanisms [11, 39, 40, 41, 42], which drive high cross-field electron currents (for more details see Ref. [43]).

Among the plethora of wave phenomena in a Hall thruster device, low-frequency oscillations propagating in the axial direction stand as one of the most common and observed in most types of Hall thrusters [7]. They appear as the axial discharge current oscillations with frequencies of 5-50 kHz [44]. A strong periodic depletion of atoms in the ionization region is observed during the oscillations, suggesting the ionization nature. In the literature, they are known as breathing modes (due to slow periodic plasma bursts out of the channel exhaust). Analytical studies of these phenomena are difficult due to the importance of nonlinear effects and the global nature of solutions; thus, numerical methods have to be used. Qualitatively, the oscillation period of breathing modes depends on the travel time of neutral particles to the ionization region, e.g. for the characteristic $1\,\mathrm{cm}$ and atom velocity $150\,\mathrm{m/s}$ gives $15\,\mathrm{kHz}$. Overall, we understand the phenomenology of the oscillations but cannot accurately predict their existence and amplitude. Generally accepted phenomenological description of these oscillations is described as the following sequence: decrease of the discharge current $\rightarrow$ decrease of ionization $\rightarrow$ increase of the neutral density in the exhaust region $\rightarrow$ increase of the electron conductivity in that region $\rightarrow$ increase of the current and ionization $\rightarrow$ neutral depletion $\rightarrow$ decrease of the current and so on. According to this picture, the oscillation frequency is related to the time necessary for the neutrals to refill the ionization region.

The 0D predator-prey model proposed earlier [45, 46, 47] is appealing because of its simplicity but fails to identify the conditions for the instability. Moreover, more accurate treatments show that the basic two-component (plasma-neutral) system with uniform ion and neutral velocities is stable [47, 48, 49]. A simple model was proposed that the ion backflow region, which occurs near the anode as a result of the large contribution of the electron diffusion current (due to the density gradient) and quasineutrality constraint, provides a critical excitation mechanism for the breathing mode [48]. Linear resistively unstable modes [50] and fluctuations of electron temperature and power absorption [47, 49] were also investigated as possible triggers of the breathing modes.

In general, several physical mechanisms affect the breathing mode excitation and characteristics: electron momentum and energy losses to the wall, anomalous cross-field transport and heating, the ion backflow, and recombination at the anode. These mechanisms are interrelated, depend in a complex way on the magnetic field configuration, and are not easily quantifiable. Numerical models that include many of these effects were proposed [51, 52, 53, 54, 46, 55]. However, some calibration and adjustment of the parameters are required to satisfactorily reproduce the breathing modes characteristics observed experimentally [56]. Therefore further insights on key physical processes are required to expand the predicting powers of such models, especially to new parameters range and new operational regimes.

While many time-dependent numerical models for breathing modes are based on fully fluid formulations, the hybrid modeling was also undertaken using the kinetic description for ions and neutrals [53, 57, 50, 54, 58, 59]. The extent to which the ion and neutrals kinetic effects influence the breathing mode excitation and characteristics remain a mute point of many studies. The goal of this paper is to analyze the role of ions and neutrals kinetic effects under the same physics of the electron dynamics, which is treated with the fluid theory. We use the axial one-dimensional full fluid and hybrid models and compare their results.

The basic fluid model describes ions and atoms with the two fluid moments (conservation of mass and momentum), and electrons are considered in drift-diffusion approximation with a full electron energy balance. In the hybrid model, heavy species (ions, atoms) are kinetic (via particle-in-cell method), and electrons are fluid (modeled in the same way in both approaches). Both models include plasma recombination at the anode and neutral dynamics with ionization due to electron-neutral impact. The plasma discharge is supported by the ionization process driven by the axial current due to the applied potential across the domain. For the fluid simulations BOUT++ computational framework [31] is used. The hybrid code was developed in the LAPLACE laboratory, France [60, 61, 52]. The parameters of the simulations are chosen according to the "Fluid/Hybrid" test case in the LANDMARK (Low temperAture magNetizeD plasMA benchmaRKs) benchmarking project [36]. Previously, a comparison between fluid and hybrid models for the axial direction of Hall thruster configuration was presented in Ref. [54]. However, this model did not include electron pressure

gradients, thus omitting the effects of electron diffusion resulting in the formation of the presheath region near the anode and ion transition through the ion-sound barrier. Nor did it include the full electron energy balance.

One of the important findings of the present paper is the identification of two distinct regimes of breathing oscillations, the result which was confirmed with both fluid and hybrid models during this benchmark. We show that the regime with higher electron energy losses exhibits the low-frequency mode ($\sim$14 kHz) that coexists with the high frequency ion "transient-time" oscillations ($\sim$150 kHz) [44]. In the second regime, with low electron energy losses, pure breathing oscillations are observed, the so-called solo regime. We believe that different mechanisms are involved in these regimes.

For the first regime, we identify the high frequency oscillations as the excitation of the resistive modes (convective instability with the characteristic ion fly-by frequency) [62, 50, 63, 64]. Such resistive-type modes appear in simple models without ionization or electron diffusion. The main feature of resistive modes is a strong dependence of growth rate and frequency on the electron mobility (resistivity) [63]. Similar features are shown in this work, while the low-frequency mode (breathing mode) has weak or no dependency on the electron mobility (see Appendix 2.A).

In fact, the frequency of resistive modes can vary significantly, ranging 0.1-10 MHz, and may become close to that of the breathing modes at the lower end of its spectrum. Some axial thruster models (with ionization but without electron diffusion) [7, 65] claimed that these modes might be responsible for the breathing modes observed in Hall thrusters. For clarity, here we will call breathing modes only those associated with atom depletion, whose frequencies scale according to atom fly-by time and ionization processes.

In our earlier work, we have proposed a reduced model (only ion and atom dynamics included) for the second, solo regime of the breathing mode. In this regime, the instability is triggered by the ion backflow (negative ion velocity) in the near-anode presheath region [48]. It was demonstrated that such configuration is prone to low-frequency oscillations, where the ion backflow region is necessary. Recently, it has been shown in Ref. [66] with a more rigorous formal analysis that the sign-alternating ion velocity profile with a positive slope (i.e. negative ion velocity near anode and positive towards the exit) indeed is a necessary condition

to excite the oscillations. It is also pointed out that the problem cannot be reduced to the 0D predator-prey model.

Finally, we demonstrate the effect of atom temperature in the solo regime. We find that a finite energy spread of injected atoms strongly suppresses the amplitude of the oscillations compared to the injection cases with the same velocity (called below as monokinetic injection). It is found that even a small spread in atom temperature for the solo regime notably lowers the amplitude of breathing mode. For the first regime, with the presence of resistive modes, the atom temperature effect is negligible. We also show the role of ion heating (due to the resistive modes) and selective ionization of neutrals.

The paper is organized as follows. In Section 2.4 the detailed description of both fluid and hybrid models is given. Section 2.5 defines the main features of two distinct regimes of low-frequency oscillations and presents results for three test cases with a detailed comparison between models.

2.4 Fluid and hybrid models of low-frequency dynamics

This section presents a detailed description of the full fluid model and the hybrid model. Two models share the same electron fluid equations (drift-diffusion approximation and energy evolution). The models are considered in the electrostatic and quasineutral approximation, with the three species: neutral atoms, ions, and electrons. The ionization effects included via the electron-atom collisions, serving as a mechanism for supporting plasma discharge. Atom losses are only due to ionization, and radial atom losses were not included. The models also include the self-consistent electric field, the anode plasma recombination, the electron pressure effects, and the electron heat flux across the magnetic field.

The simulated length of $5\,\mathrm{cm}$ is assumed in the axial direction of a Hall thruster (x-direction), with the channel exit in the middle where the radial magnetic field has its maximum, Fig. 2.1. The profile of the magnetic field magnitude given by $B = B_0 \exp\left[-\left(x - x_0\right)^2/2\delta_B^2\right]$, where $x_0 = 2.5\,\mathrm{cm}$ is the channel exit location, and δ_B is the characteristic width coefficient for the magnetic field profile, which are set $\delta_{B,\mathrm{in}} = 1.1\,\mathrm{cm}$, $\delta_{B,\mathrm{out}} = 1.8\,\mathrm{cm}$, respectively for the inner and outer regions [36].
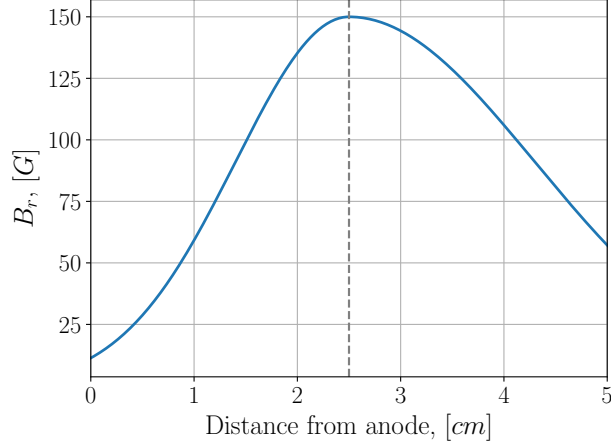
Figure 2.1: The magnetic field profile used in simulations, with the channel exit located 2.5 cm from anode (dashed line).

2.4.1 Fluid model

First, a short description of each species dynamics is given, and then the full system of time-dependent equations is formulated. For the neutral atoms, a constant flow velocity V_a along the channel is considered, and the continuity equation with the source term is used to describe their dynamics:

$$\frac{\partial n_a}{\partial t} + V_a \frac{\partial n_a}{\partial x} = -\beta n_a n_e, \tag{2.1}$$

where n_a is the atom number density, n_e is the electron number density, $\beta(\varepsilon)$ is the ionization rate coefficient that depends on the electron energy $\varepsilon = (3/2)T_e$, where T_e is the electron temperature (β is shown in Appendix 2.B). The ionization due to electron-atom impact produces a pair of ion and electron with a loss of neutral atom, hence the sink term $-\beta n_a n_e$ (same and opposite sign source terms are included in the ion and electron continuity equations).

The ion species are unmagnetized (gyroradius is much larger than the thruster dimensions for a typical magnitude of a magnetic field in the thruster) and described with the conservation of number density and momentum equations:

$$\frac{\partial n_i}{\partial t} + \frac{\partial}{\partial x}(n_i V_i) = \beta n_a n_e, \tag{2.2}$$

$$\frac{\partial V_i}{\partial t} + V_i \frac{\partial V_i}{\partial x} = \frac{e}{m_i}E + \beta n_a (V_a - V_i), \tag{2.3}$$

where n_i is the ion density, V_i is the ion flow velocity, E is the axial electric field, e is the

31

elementary charge, m_i is the ion mass (Xenon, 131.293 amu). The ion pressure term and generalized viscosity tensor are neglected in this model (ions are ballistic with temperatures much lower than that of electron component).

The magnetized electron species are described with the first three fluid moment equations: (electron inertia is neglected)

$$\frac{\partial n_e}{\partial t} + \frac{\partial}{\partial x}\left(n_e V_{ex}\right) = \beta n_n n_e, \tag{2.4}$$

$$0 = -\frac{e}{m_e}\mathbf{E} - \frac{eB}{m_e}\left(\mathbf{V}_{e\perp} \times \hat{\mathbf{z}}\right) - \frac{1}{n_e m_e}\frac{\partial\left(n_e T_e\right)}{\partial x} - \nu_m \mathbf{V}_{e\perp}, \tag{2.5}$$

$$\frac{3}{2}\frac{\partial}{\partial t}\left(nT_e\right) + \frac{5}{2}\frac{\partial}{\partial x}\left(n_e V_{ex} T_e\right) + \frac{\partial q_e}{\partial x} = -n_e V_{ex}\frac{\partial\phi}{\partial x} - n_e n_a \mathrm{K} - n\mathrm{W}, \tag{2.6}$$

where n_e is the electron density, $\mathbf{V}_{e\perp} = (V_{ex}, V_{e\theta})$ is the electron flow velocity perpendicular to the magnetic field (x and θ are the axial and the azimuthal coordinates), m_e is electron mass, B is the external radial magnetic field, ν_m is the total electron momentum exchange frequency, W is an anomalous energy loss coefficient, K is the collisional energy loss coefficient (it is shown in Appendix 2.B) and q_e is the electron heat flux. A phenomenological anomalous electron energy loss coefficient (e.g., due to radial sheath losses) W is introduced [53] as

$$\mathrm{W} = \nu_\varepsilon \varepsilon \exp\left(-U/\varepsilon\right), \tag{2.7}$$

where $\varepsilon = 3T_e/2$, $U = 20\,\mathrm{eV}$, ν_ε is the anomalous energy loss frequency. The heat flux across the magnetic field is

$$q_e = -\frac{5}{2}\mu_e n T_e \frac{\partial T_e}{\partial x}. \tag{2.8}$$

The electron momentum conservation equation (2.5) is simplified assuming no pressure gradients nor equilibrium electric fields other than in the axial direction, hence the axial electron velocity (denoted further as V_e) can be expressed as

$$V_e = -\mu_e E - \frac{\mu_e}{n_e}\frac{\partial(nT_e)}{\partial x}, \tag{2.9}$$

where the electron mobility μ_e is the well-known classical electron mobility across the magnetic field:

$$\mu_e = \frac{e}{m_e \nu_m}\frac{1}{1 + \omega_{ce}^2/\nu_m^2}, \tag{2.10}$$

where $\omega_{ce} = eB/m_e$ is the electron cyclotron frequency. Eq. (2.9) commonly called the drift-diffusion equation. The model of electron transport as based on the assumption of the following total electron momentum exchange collision frequency:

$$\nu_m = \nu_{en} + \nu_{walls} + \nu_B, \tag{2.11}$$

where the electron-neutral collision frequency ν_{en}, electron-wall collision frequency ν_{walls}, and anomalous Bohm frequency ν_B are given with

$$\nu_{en} = k_m n_a, \tag{2.12}$$

$$\nu_{walls} = \alpha 10^7 \ [\text{s}^{-1}], \tag{2.13}$$

$$\nu_B = (\beta_a/16) \, eB/m_e. \tag{2.14}$$

where $k_m = 2.5 \times 10^{-13} \, \text{m}^{-3}\text{s}^{-1}$, α and β_a are free parameters. For the electron mobility model different parameters are used inside and outside the channel (denoted additionally as *in, out*): the near wall conductivity contribution $\alpha_{\text{in}} = 1$, $\alpha_{\text{out}} = 0$, the anomalous contribution is set to $\beta_{a,\text{in}} = 0.1$, $\beta_{a,\text{out}} = 1$. The anomalous loss (electron) energy frequency coefficient in Eq. (2.7) is a constant, set to $\nu_{\varepsilon,\text{out}} = 10^7 \ \text{s}^{-1}$ outside the channel. Inside the channel $\nu_{\varepsilon,\text{in}}$ is an input parameter of the model (see Section 2.5).

Here, we seek the low-frequency and bulk plasma modes, thus electron inertia is neglected (as shown above) and further the full plasma quasineutrality is assumed. One can check the validity of the quasineutral approximation [51] by using the Poisson equation $\varepsilon_0 \partial E / \partial x = e(n_i - n_e)$ (ε_0 is the permittivity of free space). With the typical values of the electric field $E \approx 10^4$ V/m and the size of acceleration zone $1 \, \text{cm}$, average plasma density $n_0 = 10^{17} \, \text{m}^{-3}$, the difference $(n_i - n_e)/n_0 \approx 5 \times 10^{-4}$. Instead of the Poisson equation, the electric field is found from the electron momentum equation as shown below. Note that while the quasineutrality neglects a potential drop on the Debye sheath near the anode, it still allows the presheath region to form if the electron pressure is included [67, 68, 69, 70], as in our electron model. The presheath is the region where the electric field is induced to accelerate ions towards a plasma boundary to compensate the electron current due to the pressure gradient.

Thus, the full system of time-dependent fluid equations to be solved include Eqs. (2.1,2.2,2.3,2.6), along with the drift-diffusion form for the electron velocity equation (2.9). Full quasineu-

trality $n = n_i = n_e$ is enforced and the self-consistent electric field is found via the electron drift-diffusion equation (2.9), given by

$$E = \frac{J_T}{en\mu_e} - \frac{V_i}{\mu_e} - \frac{1}{n}\frac{\partial nT_e}{\partial x}, \qquad (2.15)$$

where the total current density $J_T = en\,(V_i - V_e)$. Here J_T is constant in space (divergenceless current), which can be seen by combining continuity equations for ions and electrons with quasineutral assumption. We will use the integral approach, consisting of the evaluation the total current density J_T via the constraint $\int_0^L E dx = U_0$ (then it is substituted to Eq. (2.15) to evaluate the electric field), which yields to

$$J_T = \frac{U_0 + \int_0^L \left(\dfrac{V_i}{\mu_e} + \dfrac{1}{n}\dfrac{\partial p_e}{\partial x} \right) dx}{\int_0^L \dfrac{dx}{en\mu_e}}, \qquad (2.16)$$

where L is the system length, U_0 is the applied voltage (without sheath voltage).

The fluid model is solved with the following boundary conditions. A constant mass flow rate $\dot{m}$ and the full recombination of plasma that flows to the anode determines the value of n_a at the anode boundary,

$$n_a(0) = \frac{\dot{m}}{m_i A V_a} - \frac{n V_i(0)}{V_a}, \qquad (2.17)$$

where A is the anode surface area. The value of the ion velocity is imposed at the anode as $V_i(0) = -b_v\sqrt{T_e/m_i}$ with the parameter $b_v = 0$–1, the Bohm velocity factor that can be varied. Both anode and cathode electron temperature are fixed with $T_e(0) = T_e(L) = 2\,\text{eV}$.

As noted in Ref. [51], plasma acceleration in the configuration of the axial direction of a Hall thruster shows similarities to the flow in de Laval nozzle. Indeed, the whole acceleration region can be split into subsonic $V_i < c_s$ and supersonic $V_i > c_s$ regions, where $c_s = \sqrt{T_e/m_i}$ is the ion sound speed. While in de Laval nozzle the transition through sonic point happens at the region with the smallest cross-section of the channel (due to extrema condition and regularity requirement), for the bounded plasma configuration the position is determined via the nonlinear relationship between plasma parameters (and their first derivative) at the sonic point and a value of the total current [71]. Note that the total current J_T, given by Eq. (2.16), is a function of U_0 with the integral dependence on all main plasma parameters, thus the problem is inherently nonlocal, which has no analogy with the standard de Laval nozzle.

34

Another difference is that in the axial direction of Hall thrusters the presheath region can induce the backward ion flow in a large portion of the thruster channel (see Case 2 below).

The time-dependent fluid model, equations (2.1,2.2,2.3,2.6), are solved via the BOUT++ [31] computational framework. The CVODE solver from the SUNDIALS package [34] was used to solve the algebraic-differential system resulting from the method of lines utilized in the BOUT++. The upwind terms are discretized with the WENO 3rd order scheme and other terms with the 2nd order central-difference scheme. The numerical parameters used are the following: the axial direction is discretized with 256 points, the absolute and relative tolerances for the CVODE are set to 10^{-8} and 10^{-4}, respectively. Note that the fluid equations are normalized, and the normalization scheme is given in Appendix 2.C.

2.4.2 Hybrid model

The hybrid model has the same electron equations as in the fluid model, while ions and neutrals are modeled via particle-in-cell (PIC) method [60, 61, 52]. The plasma recombination effect is also included via the relationship (2.17), but the ion velocity at the anode is not forced to satisfy the Bohm velocity. The ionization is included via the electron-atom impact with the Monte Carlo sampling of ionization events (via the null collision method [72, 35]) using the macroscopic ionization rate $\beta(\varepsilon)$, obtained in the same way as in the fluid model. Neutral atoms are injected with a constant flow rate $\dot{m}$ either with the constant velocity V_a (monokinetic), thus $f(v_x) = \delta(v_x - V_a)$, or with a half-Maxwellian velocity distribution function at the left wall (anode),

$$f(v_x) = \frac{2v_x}{v_{Ta}^2} \exp(-\frac{v_x^2}{v_{Ta}^2}), \quad v_x > 0, \tag{2.18}$$

where $v_{Ta}^2 = 2k_B T_a/m_a$ is the atom thermal speed ($m_a = m_i$), T_a is the atom temperature (in K). For the half-Maxwellian injection (2.18) the average flow velocity is $v_{Ta}/\sqrt{\pi}$. Ions are assumed singly charged and unmagnetized, thus they are only accelerated by an electric field. Ions are produced according to the ionization rate coefficient $\beta(\varepsilon)$, i.e. self-consistently with the electron temperature evolution and the local atom density. Both atoms and ions are lost at the boundaries. In this model the ion velocity is not forced to the Bohm velocity, like in the fluid ion model. With the quasineutral approach ($n_e = n_i$ is forced at every time step),

plasma density is evaluated from the ion particle distribution and thereafter used for the electron temperature (2.6) and the electric field (2.9) calculations. Formally, the evolution of the distribution function for ions $f_i(x, v_x, t)$ and atoms $f_a(x, v_x, t)$ is described with the Boltzmann equation for each specie:

$$\frac{\partial f_i}{\partial t} + v_{ix}\frac{\partial f_i}{\partial x} + \frac{e}{m_i}E\frac{\partial f_i}{\partial v} = S(x, v_x), \tag{2.19}$$

$$\frac{\partial f_a}{\partial t} + v_{ax}\frac{\partial f_a}{\partial x} = -S(x, v_x), \tag{2.20}$$

where $S(x, v_x)$ is the collisional source term due to the ionization. In the case of the monokinetic target species (atoms), the ionization leads to the ion creation with the atoms velocity V_a (constant) and the source term can be expressed [53] as $S(x, v_x) = \beta n_e n_a \delta(v_x - V_a)$. For the simulations with finite atom temperature, newly created ions assigned velocities by sampling from the isotropic Maxwellian distribution with the temperature T_a with the standard sampling techniques [73]. Solutions to Eqs. (2.19,2.20) effectively obtained by solving the motion equations for the corresponding particle type (the method of characteristics via PIC method). Eqs. (2.19,2.20) and the electron fluid equations (2.6, 2.9) form the complete set of equations solved in the hybrid model.

In the hybrid model, in all test cases presented below, the average total number of macroparticles in the system was 5 million for the ions and 0.5 million for the atoms. The time step was set to $\Delta t = 1.62\,\text{ns}$. The fluid equations (for electrons) in the hybrid model are resolved with the finite volume methods [35], with the same spatial discretization as the PIC method, set to 300 cells. The results presented in this paper do not depend significantly on these parameters.

2.5 Simulation results and comparison

The fluid and the hybrid models described above were studied for three test cases (denoted as Cases 1, 2, and 3). Cases 1 and 2 will demonstrate two distinct regimes of low-frequency oscillations, and Case 3 shows the effect of atom temperature. Note that Cases 1 and 2 use monokinetic atoms with the velocity $V_a = 150\,\text{m/s}$. Cases 1 and 2 are chosen with the following observation: larger values of anomalous (electron) energy loss frequency $\nu_{\varepsilon,\text{in}}$ in

Eq. (2.7) allow the high frequency (of ion fly-by time) modes to appear and coexist with the low-frequency modes, represented in Case 1. The simulations with lower values of $\nu_{\varepsilon,\text{in}}$ reveal only the large amplitude low-frequency oscillations, we call it the solo regime. In Case 1 $\nu_{\varepsilon,\text{in}} = 0.95 \times 10^7\,\text{s}^{-1}$, and in Case 2 $\nu_{\varepsilon,\text{in}} = 0.4 \times 10^7\,\text{s}^{-1}$. This is the only parameter distinguishing Cases 1 and 2 (for all cases reported in this paper we keep $\nu_{\varepsilon,\text{out}} = 10^7\ \text{s}^{-1}$).
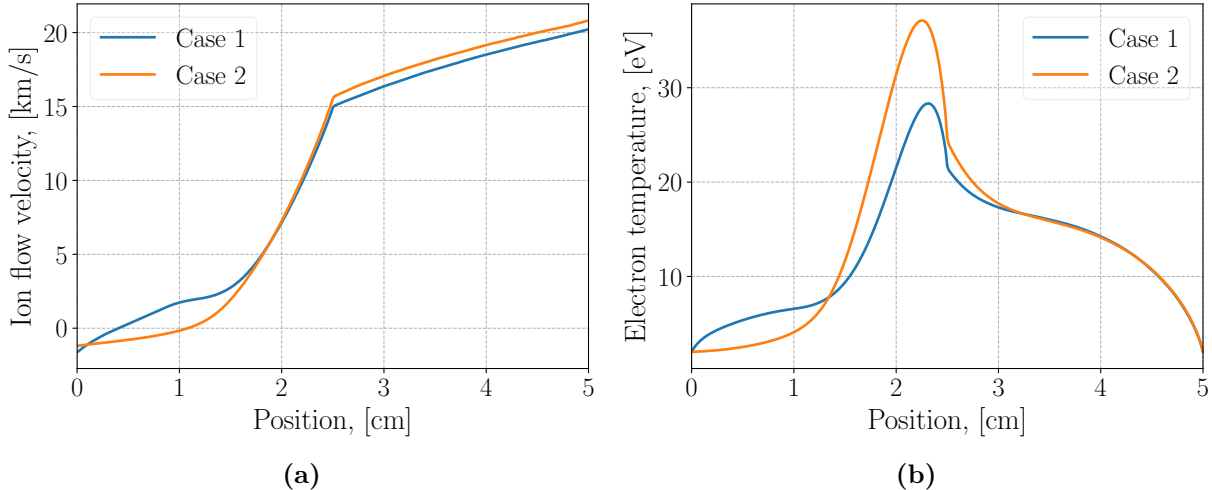
Figure 2.2: Averaged in time profiles of ion velocity (a) and electron temperature (b) for Case 1 ($\nu_{\varepsilon,\text{in}} = 0.95 \times 10^7\,\text{s}^{-1}$) and Case 2 ($\nu_{\varepsilon,\text{in}} = 0.4 \times 10^7\,\text{s}^{-1}$). The result is obtained with the hybrid model.

Besides the different time-dependent behaviour, these regimes show a notable difference in the time-averaged axial profiles of the ion velocity and the electron energy, see Figs. 2.2a and 2.2b. For Cases 1 and 2 the ion velocity profile is similar near the exit and beyond, but in the near-anode region the ion backflow region (where ions are moving towards the anode) is much shorter for Case 1, Fig. 2.2a. The ion backflow region is associated with the presheath formation near the anode (with the negative electric field). The size of the presheath region as a function of $\nu_{\varepsilon,\text{in}}$ is shown in Fig. 2.4, where a transition between regimes with large and short backflow region happens near the value $\nu_{\varepsilon,\text{in}} = 0.75 \times 10^7\,\text{s}^{-1}$. The electron temperature for Case 2 is peaked near the channel exit, Fig. 2.2b, with very low values in the near-anode region. For Case 1 the electron temperature spreads more uniformly and to the near-anode region.

The difference in the electron temperature distributions might be due to the difference in
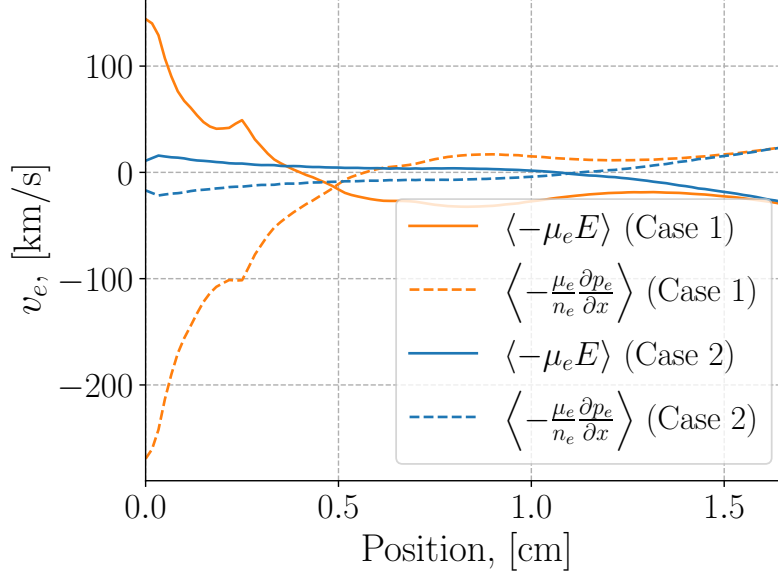
Figure 2.3: Electron flow velocity components, response to the electric field and due to due for Case 1 and 2 (result obtained with the hybrid model).

the electron flow velocity near the anode. Fig. 2.3 shows the time-averaged electron velocity components, evaluated according to Eq. (2.9). Note substantially higher electron velocity due to the pressure gradient in Case 1 for $x < 0.4\,\mathrm{cm}$, which also results in larger total electron flow velocity near the anode. Thus, in Case 1, convection reduces the electron temperature in the ionization region (increasing it near the anode). Indeed, the average gradient parameter $L_n^{-1} = \partial_x n_i / n_i$ is about five times larger for Case 1, which drives this electron current. Recall that the presheath region is formed due to diffusive electron current by inducing ion current (total current is conserved), generating the negative electric field in this region. All features presented above clearly distinguish Case 1 and Case 2.

Finally, Case 3 demonstrates the effect of finite atom temperature, where atoms are injected into the system with the half-Maxwellian distribution, Eq. (2.18), and all the other parameters are the same as in Case 2. The main effect of atom temperature is found to be a significant reduction of breathing mode amplitude to those observed in Case 2. Besides finite atom temperature, all parameters for Case 3 are exactly the same as in Case 2, and the atom temperature is set to $T_a = 500\,\mathrm{K}$ ($V_a = 142\,\mathrm{m/s}$, close to monokinetic $150\,\mathrm{m/s}$ used in Cases 1 and 2).
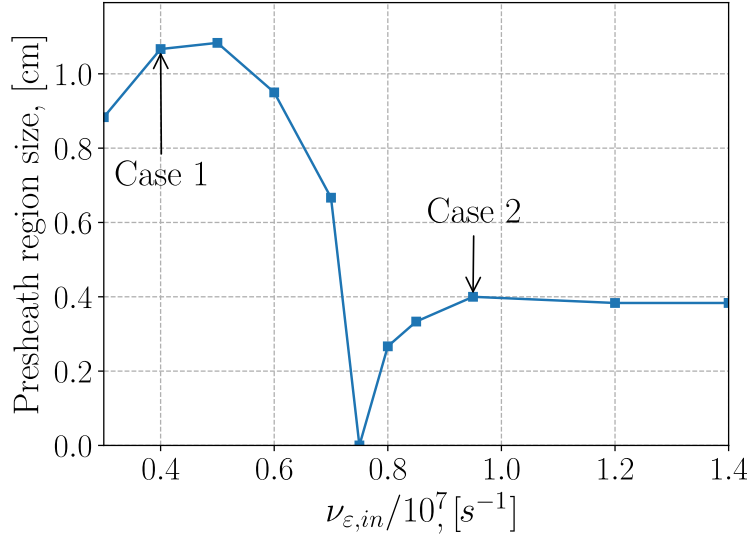
Figure 2.4: Extent of the presheath zone, defined as the region with negative electric field near the anode, as a function of anomalous electron energy losses coefficient ν_ε (result obtained with the hybrid model).

2.5.1 Case 1: Low electron energy losses; the co-existence of low- and high-frequency modes

This case exhibits both low- and high-frequency oscillations in the fluid and the hybrid models. The hybrid model results in a smaller amplitude of the total current, see Figs. 2.5a and 2.5b. The time-averaged total currents are close, $8.2\,\mathrm{A}$ in the hybrid model and $8.3\,\mathrm{A}$ in the fluid model. The ratio of the time-averaged ion current (at the plume exit, $x = 5\,\mathrm{cm}$) to the total current is 45% in the hybrid model and 48% in the fluid.

The spectral power of the total current also shows some differences in both low- and high-frequency ranges, Figs. 2.6a and 2.6b. The main low-frequency mode in the fluid model is $11.4\,\mathrm{kHz}$, while it is $14.4\,\mathrm{kHz}$ in the hybrid model. The total current signal in the hybrid model contains more noise (statistical noise due to the use of macroparticles), but the high-frequency component is clearly seen at around $125\,\mathrm{kHz}$. In the fluid model the high-frequency mode is shifted towards higher frequencies, centered at about $175\,\mathrm{kHz}$.

39
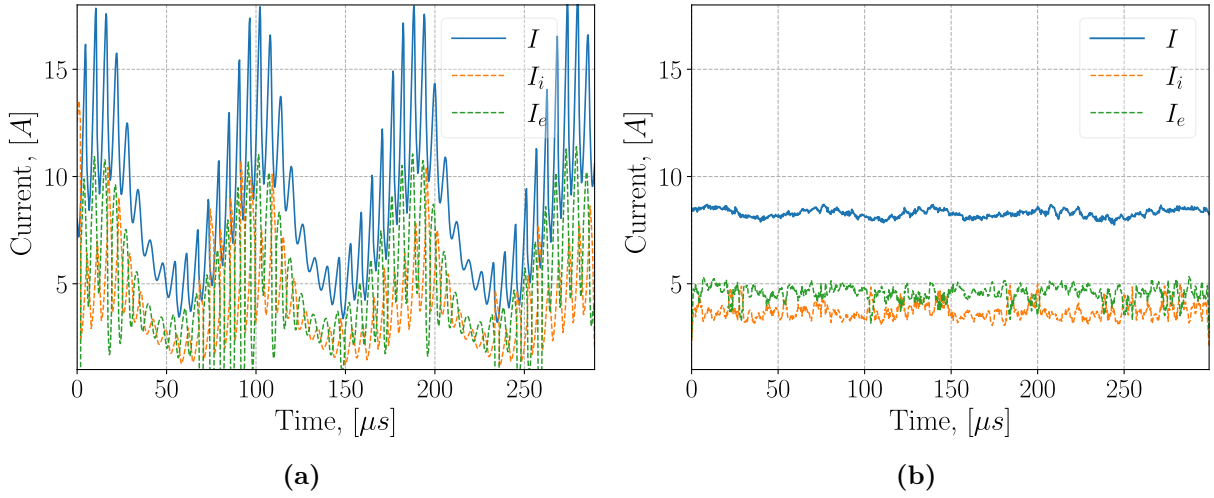
Figure 2.5: Amplitudes of the total, ion, and electron currents in fluid model (a) and hybrid model (b). Ion and electron currents are evaluated at $x = 5\,\mathrm{cm}$. Small averaging window of length $2.3\,\mu\mathrm{s}$ is applied to the ion and electron currents (to filter out high-frequency noise).
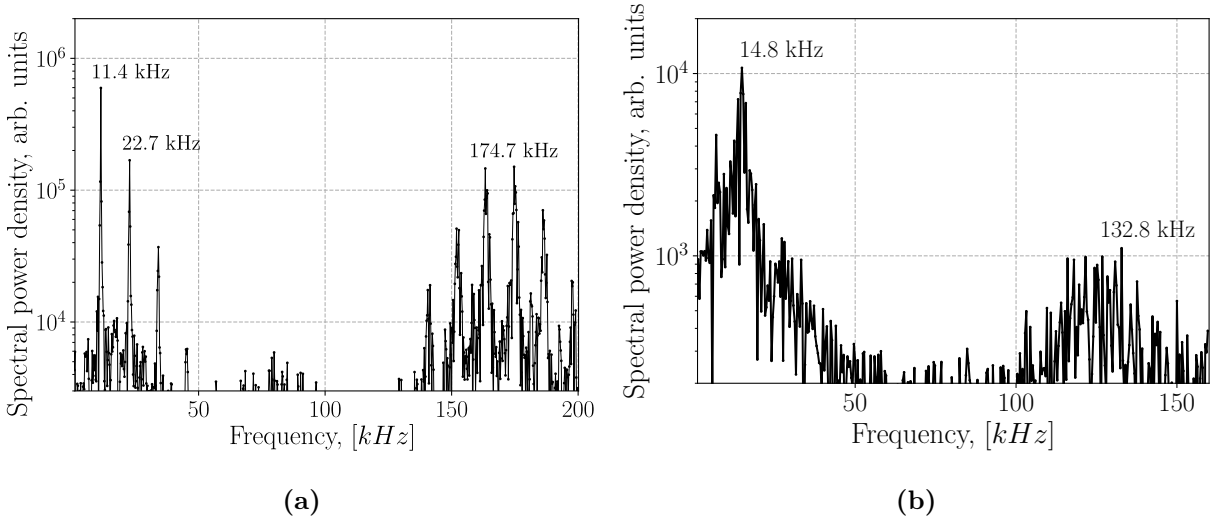
Figure 2.6: Spectral density of the total current yield in fluid model (a) and hybrid model (b).

Besides the currents, a more rigorous comparison between the two models is shown in Figs. 2.7a-2.7d, with the time-averaged axial profiles of the main plasma quantities. Due to the oscillatory nature of these solutions, the averaging time window was chosen as the ten periods of the corresponding main low-frequency mode in each simulation. The main

discrepancy lies in the peak plasma density in the ionization (source) region at about $1.3\,\mathrm{cm}$ from the anode; the hybrid model results in the higher value of the peak plasma density. Also, the ion velocity in the plume ($x > 2.5\,\mathrm{cm}$) is slightly higher in the hybrid model.
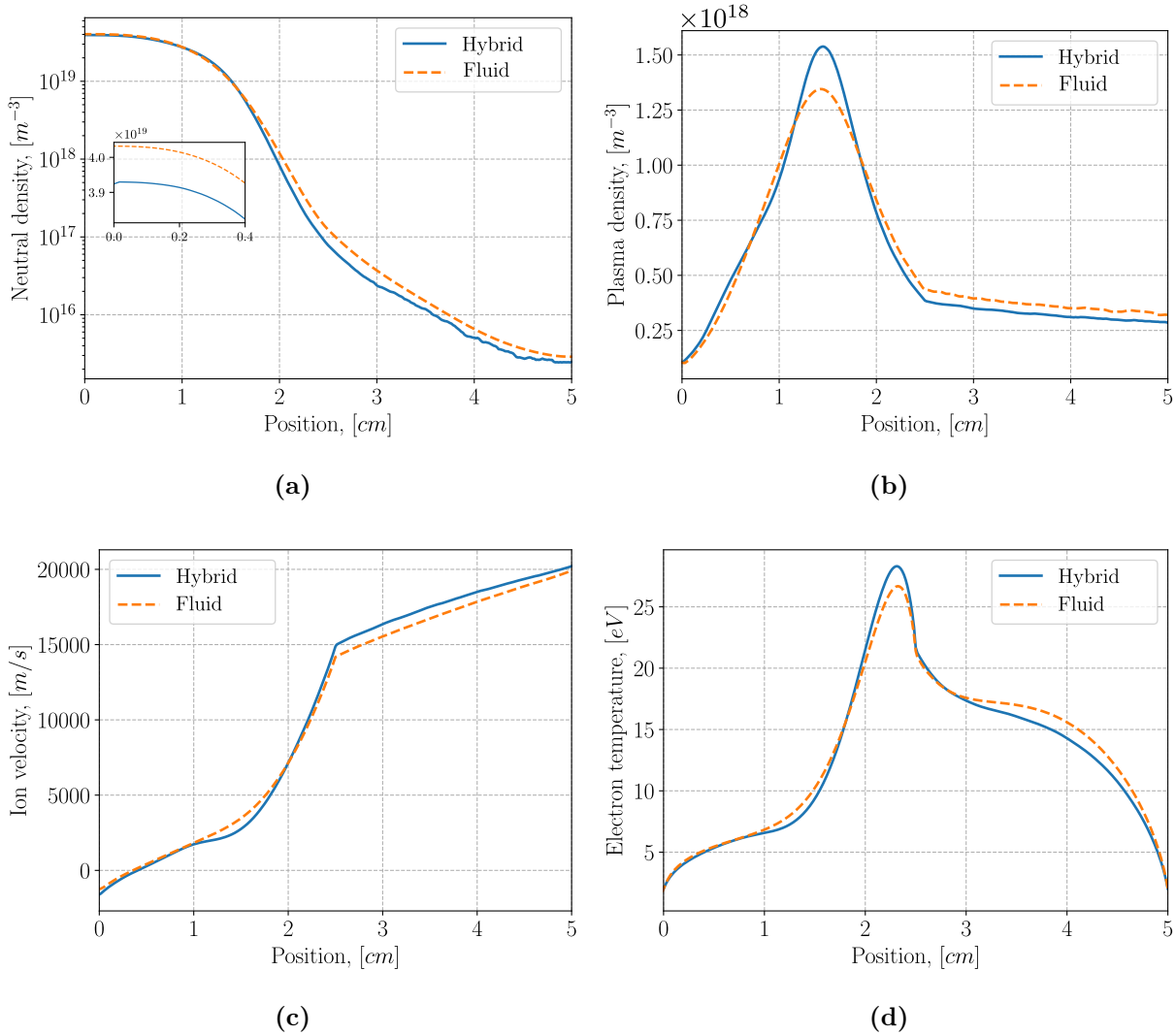
Figure 2.7: Comparison of time-averaged axial macroscopic profiles resulted from fluid and hybrid models of neutral density (a), plasma density (b), ion flow velocity (c), and electron temperature (d).

The ion phase space (hybrid model) is shown in Fig. 2.8a. The ion velocity distribution function (IVDF) is highly inhomogeneous inside the channel, suggesting that the higher fluid moments may play a role (recall that the nullified pressure term gives the closure in the ion

fluid model). Typically, ion pressure effects are neglected due to a low ion temperature; ion formation is due to the ionization process as they carry the low atom temperature even when accelerating by the axial electric field.
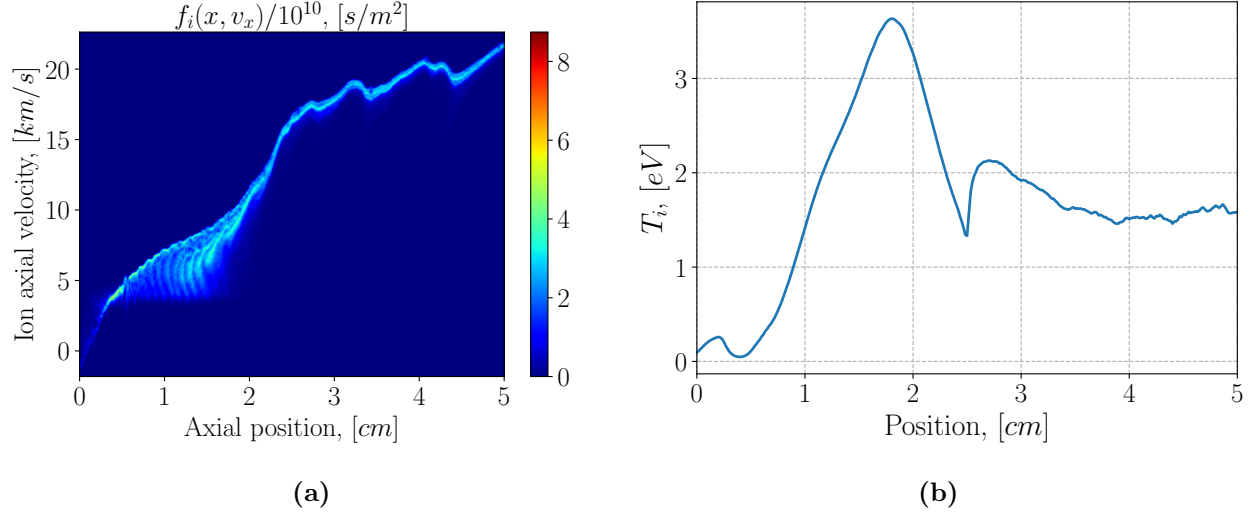
Figure 2.8: Instantaneous image of ion distribution function (in space of axial co-ordinate and axial velocity) in the hybrid model (a). Ion temperature spatial profile (time-averaged) evaluated from ion kinetic representation in the hybrid model (b).

To check the validity of this assumption, the fluid moments were calculated from the kinetic particle representation in the hybrid model. It allows to test the ion momentum balance equation (to identify the role of the ion pressure term) in a more complete form:

$$\frac{\partial V_i}{\partial t} + V_i \frac{\partial V_i}{\partial x} = \frac{e}{m_i} E - \frac{1}{n_i} \frac{\partial p_i}{\partial x} + \beta n_a \left(V_a - V_i \right), \tag{2.21}$$

where the fluid moments, such as the ion density n_i, the ion flow velocity V_i, and the ion pressure p_i were evaluated from the ion distribution function in the following way:

$$n_i = \int f_i dv_{ix}, \tag{2.22}$$

$$V_i = \frac{1}{n_i} \int v_i f_i dv_{ix}, \tag{2.23}$$

$$p_i = m_i \int v_i' v_i' f_i dv_{ix}, \tag{2.24}$$

where $v_i' = v_i - V_i$ is the random component of particle velocity. The time-averaged profile of the ion temperature $T_i = p_i/n_i$ is shown in Fig. 2.8b, revealing values of the ion temperature

up to $3.5\,\mathrm{eV}$ in the ionization region (with the average over the whole domain of $1.7\,\mathrm{eV}$). For the momentum balance test, each term in Eq. (2.21) was evaluated as a function of time and space and then averaged in time over a few periods of the main low-frequency mode. Fig. 2.9a shows the difference between the left- and the right-hand sides of equation (2.21). The plotted terms were normalized to the value V^2/L, where the ballistic ion velocity is $V^2 = 2eU_0/m_i$ with the potential difference $U_0 = 300\,\mathrm{V}$ over the system length L. It is seen that the ion pressure term notably improves the overall ion momentum balance, suggesting the fluid model for this configuration should not ignore the ion pressure.
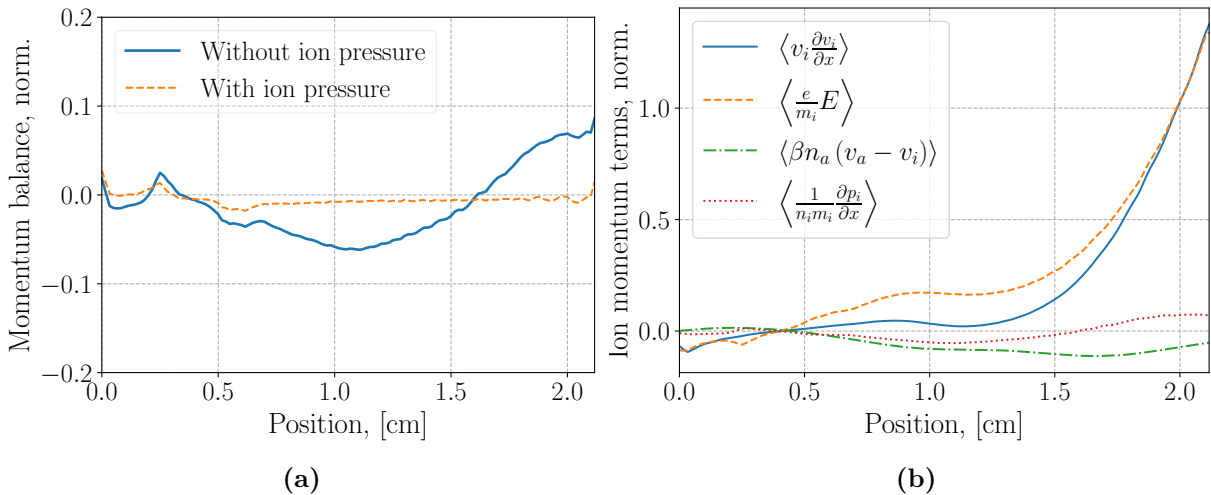
Figure 2.9: Difference between left and right hands sides of the ion momentum balance equation (ion-mom) evaluated from the kinetic description of the hybrid model (a). Separate terms of the same equation averaged in time (denoted with angle brackets) over few periods of the low-frequency component (b).

It is interesting to further inspect each term in Eq. (2.21). The unsteady term $\partial V_i/\partial t$ is negligible due to time averaging, while the other terms have comparable values inside the channel, see Fig. 2.9b. In the near-anode region, the ion pressure ($T_i \approx 0.1\,\mathrm{eV}$) and the ionization friction are negligible, so the ions accelerate towards the anode in the weak negative electric field ballistically. Then in the ionization (source) region, we see that all terms are comparable. The ion pressure and the collisional drag compensate the ballistic acceleration, so the ion inertia remains low. Finally, in the acceleration zone ($x > 1.5\,\mathrm{cm}$) and beyond the inertial and the ballistic terms start to dominate. It is seen that the ion pressure term changes the sign at $x \approx 1.6\,\mathrm{cm}$ (due to ion density profile, Fig. 2.7b) and contributes to the

ion acceleration.

Based on the results above, the ion pressure force term $-T_i\partial_x n_i$ was added to the fluid model with the temperature kept constant for simplicity. We understand that for the self-consistent treatment, an ion energy balance equation shall be included (or equation of state). The average (space and time) value of the ion temperature evaluated in the hybrid model for this case was $1.7\,\text{eV}$. However, it is found to produce a fully stationary solution with the ion pressure force mentioned above. Using a slightly lower value, $T_i = 1.2\,\text{eV}$, resulted in the oscillatory solution. This results in a better agreement between the two models, the total current amplitude decrease and the main low-frequency mode increase, Figs. 2.10a and 2.10b. The low-frequency mode increased to $13.9\,\text{kHz}$, and the high-frequency peak is shifted to a lower value of $153\,\text{kHz}$. The ratio of the ion current to the total current shows an improved agreement, 45%, the same as in the hybrid model. However, the time-averaged total current value of $8.7\,\text{A}$ became somehow larger than in the hybrid model (8.2 A). Also, the higher frequency component is closer to the hybrid result. As for the peak plasma density discrepancy (Fig. 2.7b), it remained similar.

(a)   (b)
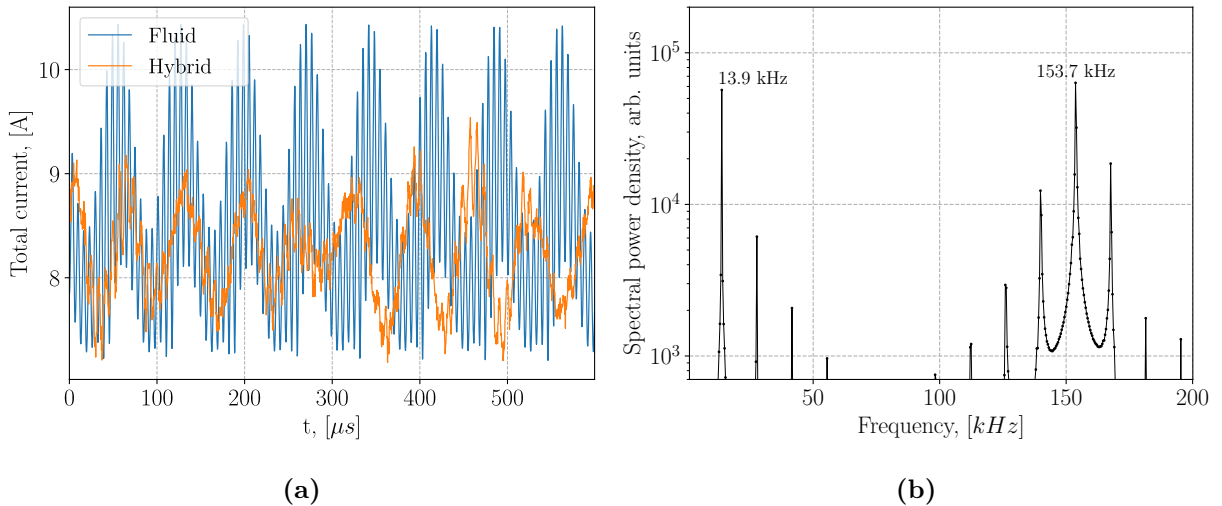
Figure 2.10: Comparison of total current in the fluid model and hybrid model (a) and the spectral power density of the total current in the fluid model (b). The result obtained is for the fluid model with the ion pressure term included.

44

2.5.2 Case 2: High electron energy losses; the solo regime of the low-frequency mode

This case is subject to the low-frequency oscillations only, with the only difference to Case 1 in the value of the anomalous (electron) energy loss frequency, which is $\nu_{\varepsilon,\text{in}} = 0.4 \times 10^7 \, \text{s}^{-1}$. As in the previous case, the total current amplitude is higher in the fluid model, Figs. 2.11a and 2.11b, but the main oscillation frequency in two models is similar, Figs. 2.12a and 2.12b.

The time-averaged profiles agree well between the two models, with the only notable discrepancy in the plasma density profile, which is ∼30% lower inside the channel region for the fluid model, see Figs. 2.13a-2.13d.

Unlike in Case 1, the IVDF for this case (Fig. 2.14a) reveals that the ion population remains cold (everywhere except in the near-anode region), and the ion momentum balance must be well satisfied without the ion pressure term. This is seen in Fig. 2.14b, where the ion pressure force remains low everywhere in the channel. In fact, in this case, the ballistic ion acceleration is more pronounced, dominating everywhere except the stall point ($V_i \approx 0$). Indeed, the average (space and time) ion temperature, calculated similarly as in Case 1 from the hybrid model, is $0.3 \, \text{eV}$ (about 5 times smaller than in Case 1) and not exceeding $1 \, \text{eV}$ in the domain.

(a)   (b)
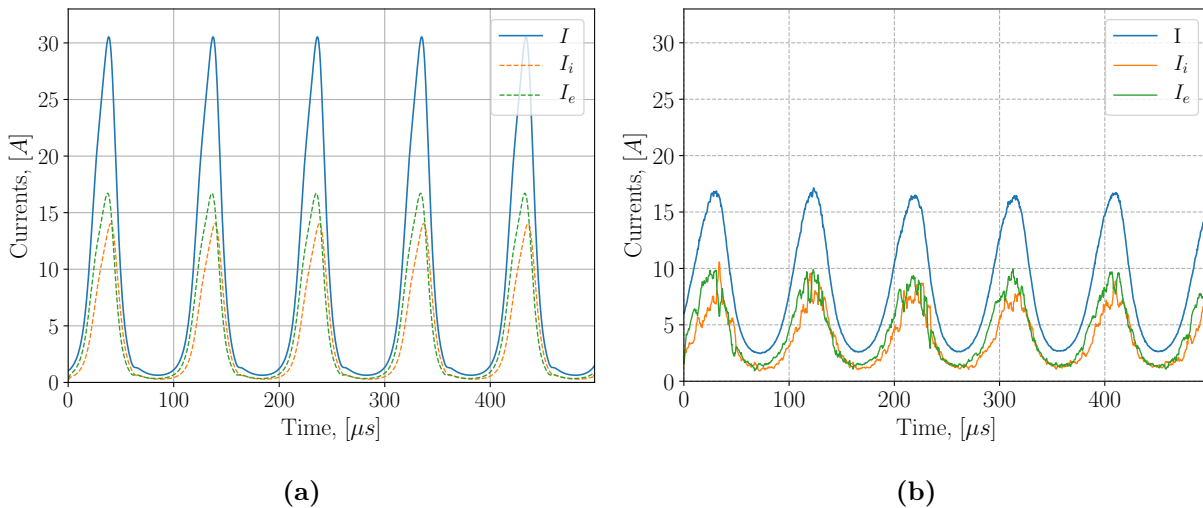
Figure 2.11: Amplitudes of total, ion, and electron currents in fluid model (a) and hybrid model (b) for Case 2. Ion and electron currents are evaluated at $x = 5 \, \text{cm}$.
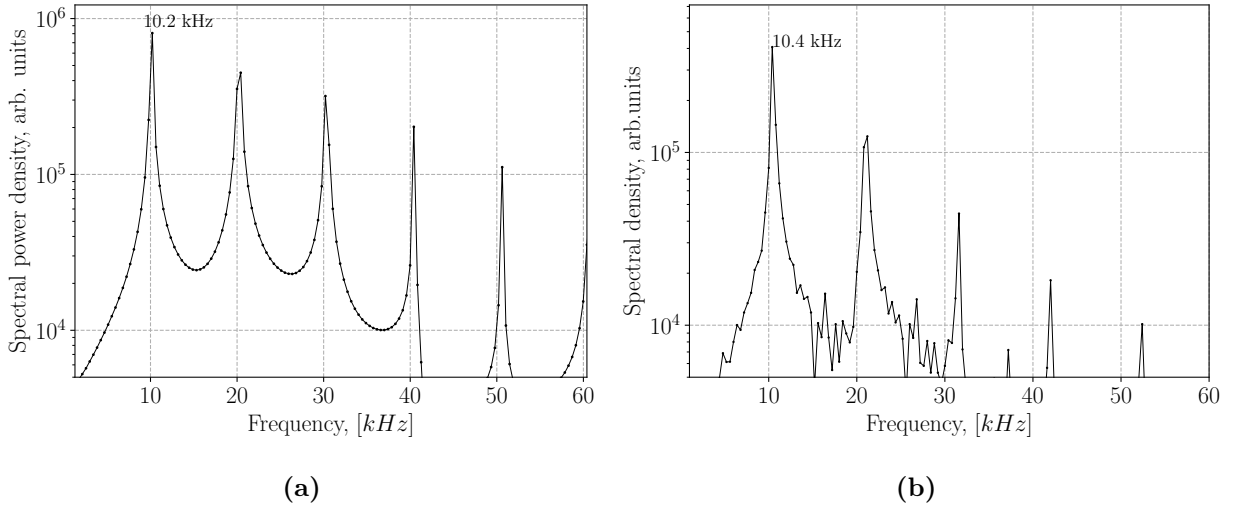
Figure 2.12: Spectral density of the total current for fluid model (a) and hybrid model (b).

The main stages of the breathing mode dynamics are illustrated with the plasma and atom density distributions at various moments in time, Fig. 2.15. After atoms reach the ionization zone and undergo ionization, plasma density increases and is quickly depleted ($\sim$1 km/s) to the left (due to the backflow region with negative ion velocity) and the right of the ionization zone. Then all of the ion flux that reached to the anode recombines and forms the peak in neutral density at the anode, increasing the number of atoms advecting to the ionization zone; this process repeats. In our previous work, Ref. [48], this setup was studied in detail, and it was shown that the ion backflow region plays a crucial role in these oscillations and that they can exist without the recombination mechanism.

It is found that the oscillation dynamics in Case 2 highly depends on the recombination at the anode, modeled with Eq. (2.17), and the number of recombined atoms proportional to the oscillation current amplitude. Note that in Case 1, recombination plays a minor role and does not affect the presented results. In contrast, turning off the recombination in Case 2 nullifies the oscillations and the stationary solutions obtained (in both models). We suggest that the main difference in this case between the fluid and the hybrid model, in this case, lies in the differences with the ion velocity boundary condition.
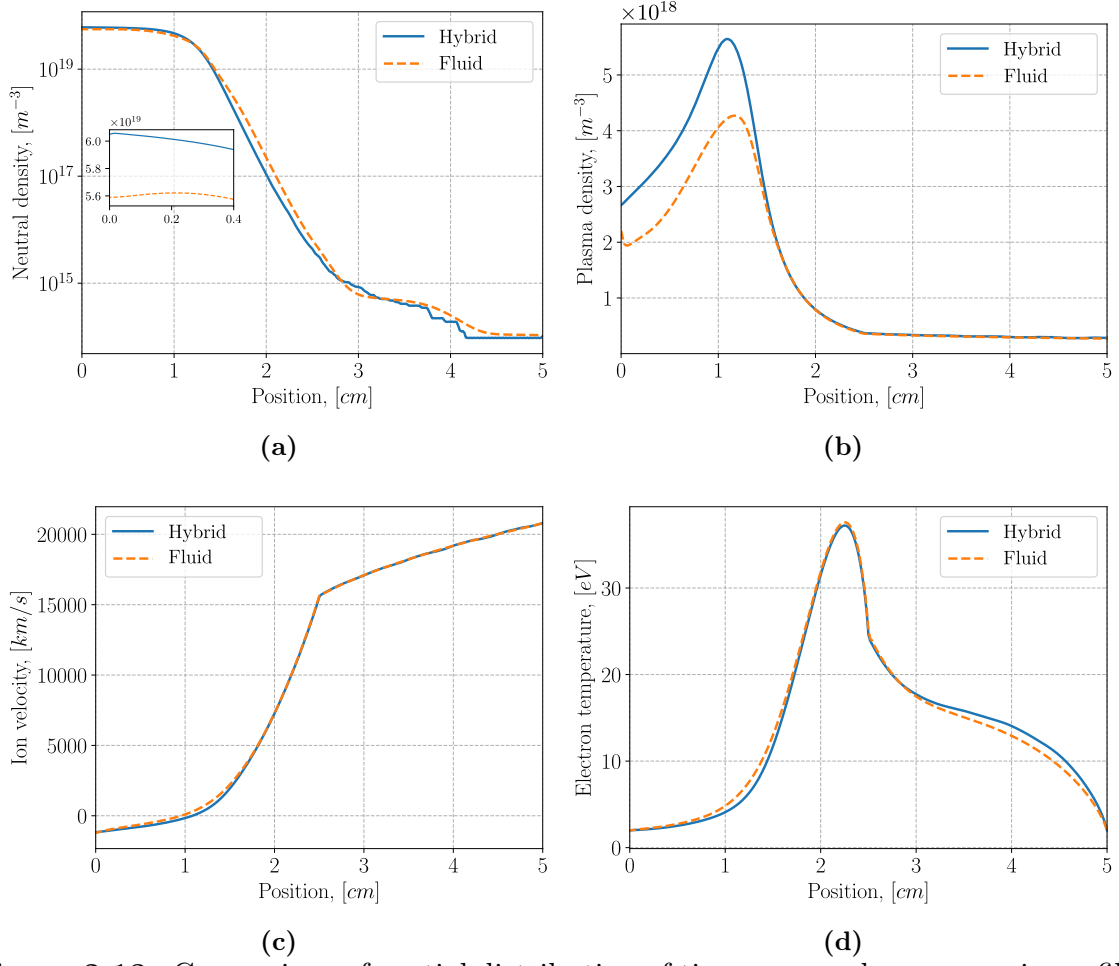
Figure 2.13: Comparison of spatial distribution of time-averaged macroscopic profiles between fluid and hybrid models for Case 2.
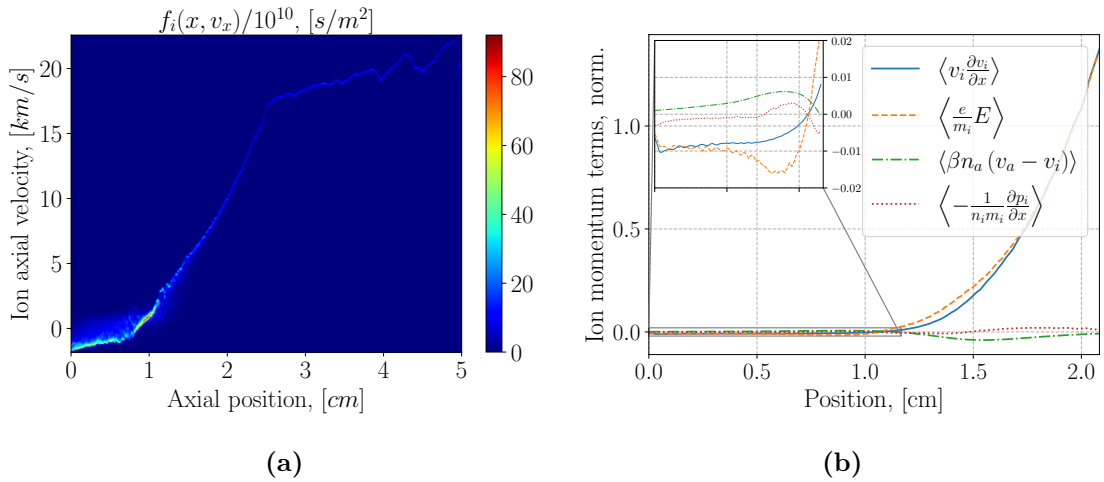
Figure 2.14: Instantaneous image of ion distribution function (in space of axial coordinate and axial velocity) in the hybrid model (a). Separate terms of the ion momentum balance equation (2.22) evaluated from the ion kinetic description (hybrid model), averaged in time (denoted with angle brackets) over few periods of the low-frequency component (b).
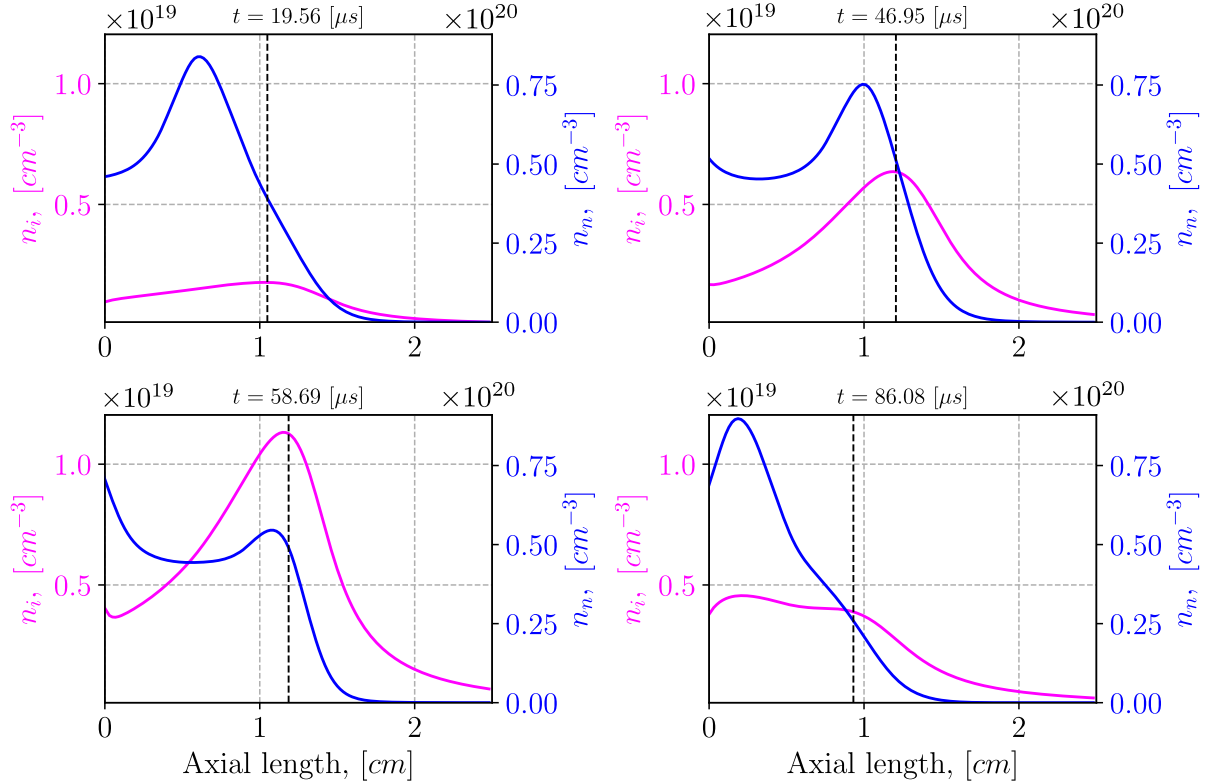
Figure 2.15: Neutral and plasma density evolution during one oscillation period. Dashed line separates the region with negative (to the left) and positive (to the right) ion velocity.

Normally, in the fluid quasineutral models, this boundary condition is fixed to the Bohm velocity, as in our fluid model. When the Bohm boundary condition is scaled with the factor $b_v = 0$–1 (ion velocity effectively decreased at the anode) in the fluid model, the oscillation amplitude also decreases, see Fig. 2.16. It clearly shows that the plasma recombination provides the additional feedback in this configuration, and the main difference with the hybrid model lies in the ion boundary conditions causing larger oscillation amplitude in the fluid model. In the hybrid model (in our setup), ions are not forced to satisfy the Bohm condition, and the flow velocity is established self-consistently. We modeled this behaviour with the free boundary condition for the ion velocity at the anode in the fluid model, forcing $\partial_x^2 V_i(0) = 0$. In the presence of ion backflow (like we see in Case 1,2) in the quasineutral approximation, the ion velocity at the anode is defined self-consistently by the characteristic at the location where $V_i = 0$; thus, a fixed boundary is not required.
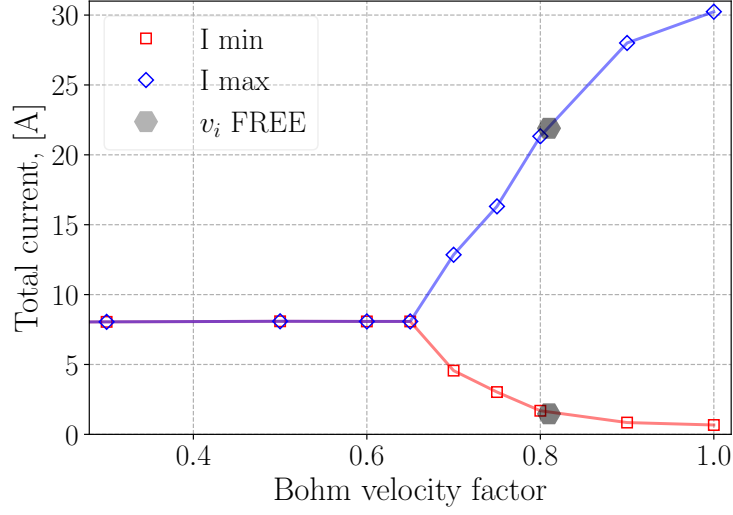
Figure 2.16: Minimum and maximum total current values during oscillations for various ion velocities at the anode, expressed as fractions of the Bohm velocity. Note that oscillations are absent for $V_i < -0.65c_s$.

The obtained result in the fluid model with the free boundary condition for the ion velocity at the anode reveals less violent oscillations and generally better agrees with the hybrid model results. The total current oscillation amplitude is lower, Fig. 2.17, closer to the hybrid mode result. The time-averaged atom and plasma density profiles are in a better agreement, Figs. 2.18a and 2.18b.
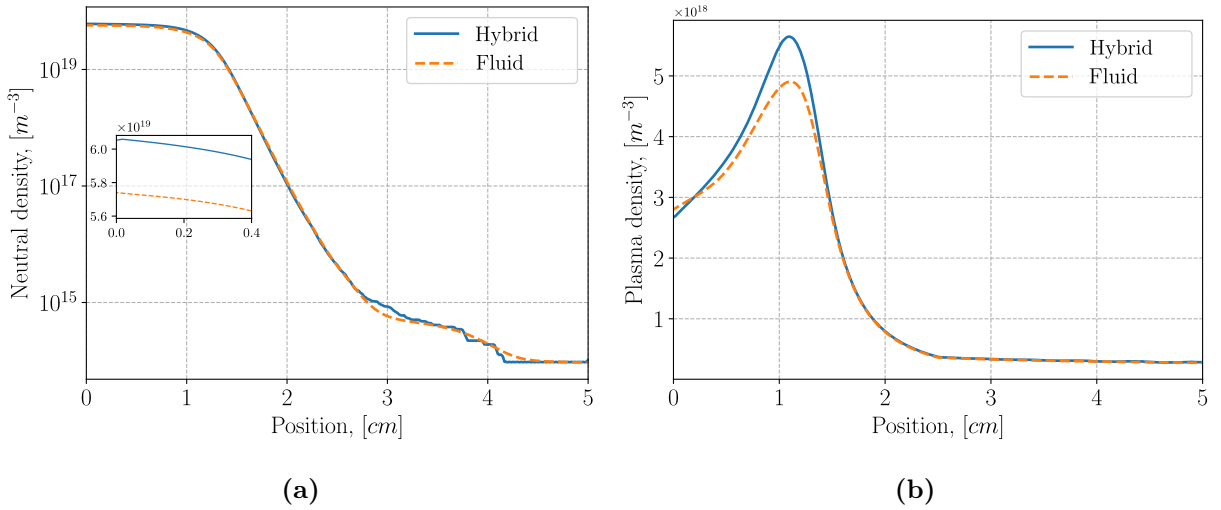
Figure 2.18: Atom (a) and ion (b) axial profiles, averaged in time, compared in both models where the free boundary condition used in the fluid model.
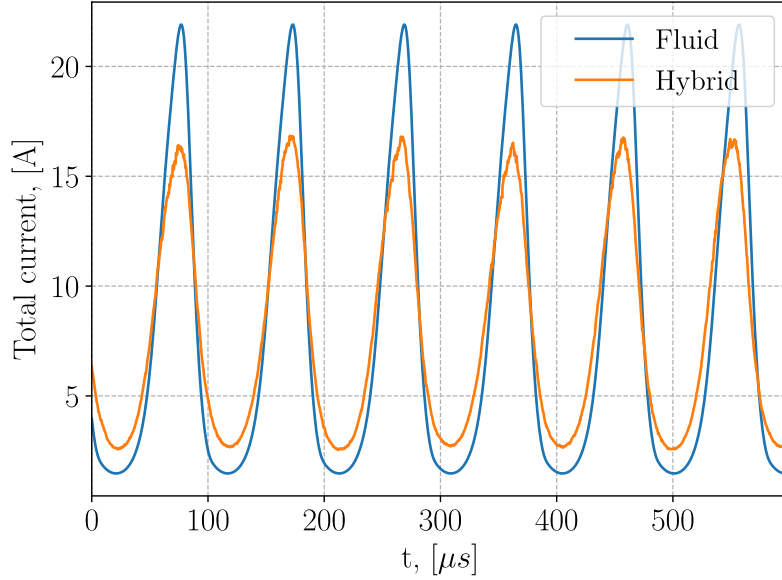
Figure 2.17: Comparison of the total current obtained in both models where the free boundary condition used in the fluid model for ion velocity at the anode.

2.5.3 Case 3: Effects of finite temperature of neutral atoms

Here, the finite atom temperature is included while all other parameters are kept as in Case 2. Atoms are injected at the anode with the half-Maxwellian flux distribution, Eq. (2.18) with a temperature $T_a = 500 \, \text{K}$. Unlike Case 2, the oscillation amplitude in this case is much smaller in the hybrid model, Fig. 2.20a, with the amplitude of $\sim 1 \, \text{A}$ (in comparison to Case 2 with $\sim 13 \, \text{A}$). In the previous cases, injected atoms in the hybrid model were kept monokinetic (zero thermal energy). The average injection velocity for the half-Maxwellian is $V_0 = v_{Ta}/\sqrt{\pi} = 142 \, \text{m/s}$, which is close to $150 \, \text{m/s}$ used in the previous monokinetic runs.

It was noticed that the atom flow velocity in the hybrid model exhibits a clear spatial dependence, "accelerating" along the channel. This effect is known as selective ionization (the ionization frequency does not depend on the atom particle velocity, but their mean free path does), observed both in experiments [74, 75] and simulations [76]. It is clear that atoms in the fluid model with the simple advection equation (2.1) cannot capture this effect; hence the atom momentum balance equation was included in the fluid model:

$$\frac{\partial \left(n_a V_a \right)}{\partial t} + \frac{\partial}{\partial x} \left(n_a V_a^2 \right) = -\beta n_a n_i V_a - \frac{T_a}{m_i} \frac{\partial \left(n_a \right)}{\partial x}, \tag{2.25}$$

where the closure is given with the constant temperature $T_a = 500 \, \text{K}$. The illustration that

the momentum balance given by Eq. (2.25) has a sufficient number of terms, the atom fluid moments were calculated from the kinetic representation of atoms in the hybrid model, and the balance is compared, see Fig. 2.19. Thus, Eq. (2.25) along with the continuity equation

$$\frac{\partial n_a}{\partial t} + \frac{\partial (n_a V_a)}{\partial x} = -\beta n_a n_i \tag{2.26}$$

solved in the fluid model, with $T_a = 500\,\mathrm{K}$ and the fixed atom flow velocity at the anode $V_a(0) = 142\,\mathrm{m/s}$ (Dirichlet condition), and the same recombination boundary condition given by Eq. (2.17). This allowed to recover qualitatively the atom flow velocity behaviour, Fig. 2.20b, but in the same time the fluid model resulted in a completely stationary solution, Fig. 2.20a.
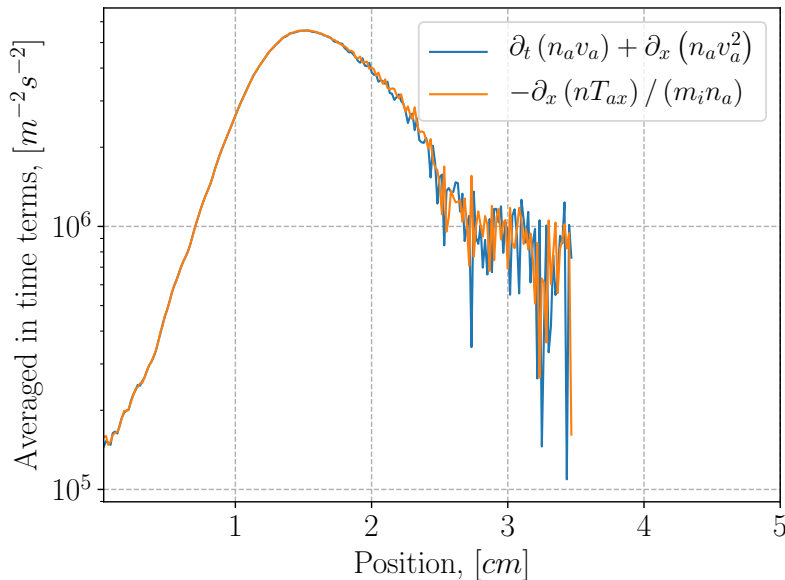
(a)

Figure 2.19: Atom momentum balance equation terms evaluated from the hybrid model results. Note that the number of macroparticles (and atom density) significantly decrease to the right along the channel elevating the noise.

To better identify the role of the atom distribution in the hybrid model, we configured the shifted Maxwellian distributions [73] for atoms with various temperatures denoted as $T_{a,s}$, and the fixed shift velocity $150\,\mathrm{m/s}$. Thus, the value of $T_{a,s} = 0\,\mathrm{K}$ corresponds to Case 2. We found that even a low spread for atom velocities, e.g. corresponding to $T_{a,s} \approx 50\,\mathrm{K}$, heavily damps the oscillation amplitude to the order $1\,\mathrm{A}$, similar to what we obtained with
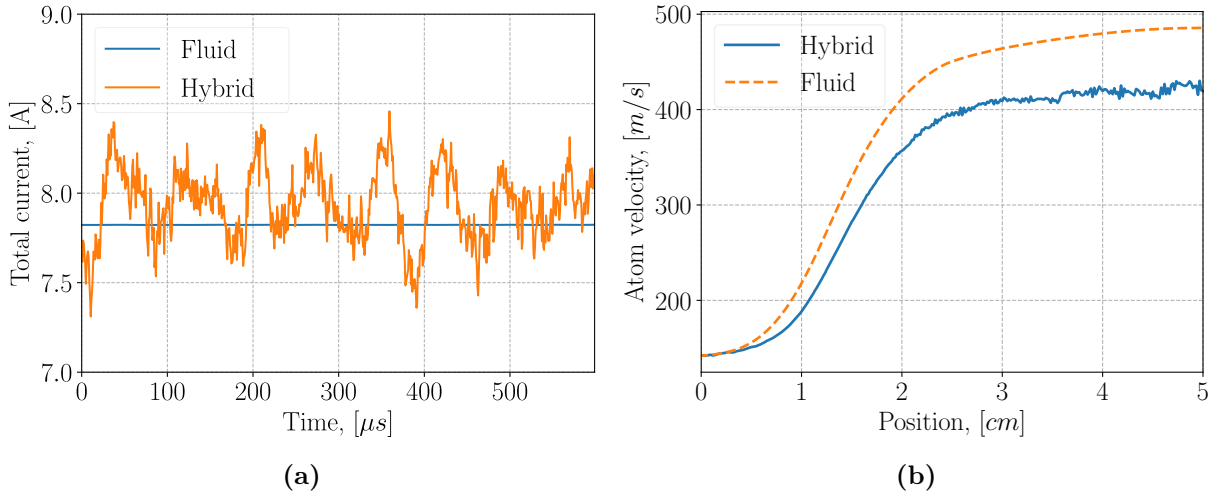
Figure 2.20: The total current in fluid and hybrid simulations (a); comparison of time-averaged spatial profile of atom flow velocity for both models (b).

the half-Maxwellian and $T_a = 500\,\mathrm{K}$.

Interestingly, we were not able to find higher amplitude low-frequency oscillations for this case in the hybrid model (scanning parameters like ν_ε or β_a). However, slightly varying the maximum magnetic field profile position (moving it inside the channel), higher amplitude breathing modes were observed even with thermal atoms. This important behaviour needs further attention, which is out of the scope of this paper and is left for future studies.

2.6   Concluding remarks and summary

Generally, plasma models for Hall thruster configuration have to deal with long time scales (defined by slow neutral dynamics, requiring at least $\sim 10^6$ electron plasma periods) and large spatial scales (above $\sim 10^3\ \lambda_{De}$). A scale separation by many orders is a typical problem in plasma modeling. Full kinetic descriptions for the problem involving low-frequency dynamics in the axial direction may not be practical due to computational cost and potential numerical problems. Reduced plasma models, such as the fluid model formulated via the conservation laws derived from higher dimensional kinetic formulation, are less computationally expensive and capture main physical phenomena in many situations. Fluid formulations typically allow easier analysis and physical interpretation of the results. A good compromise is achieved with
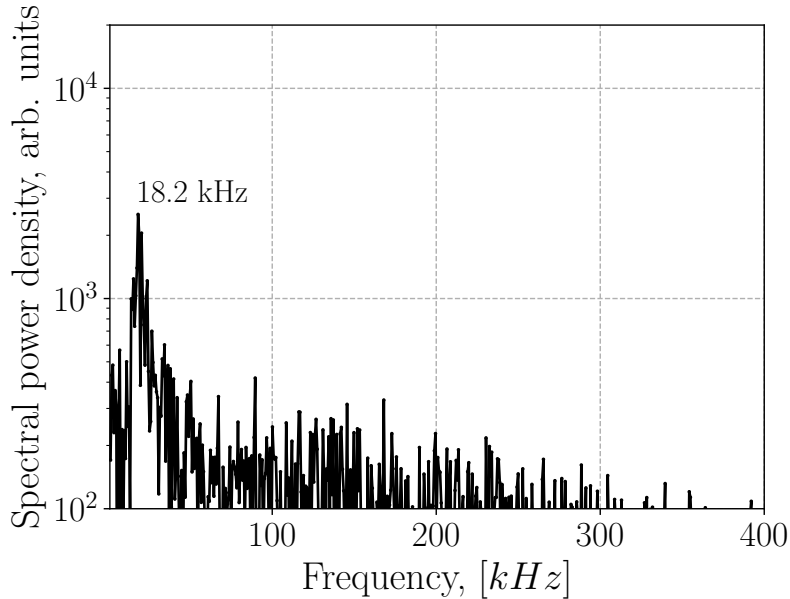
Figure 2.21: Power spectrum of the total current in the hybrid simulation. Note that there is increase in frequency (from 10.2 kHz to 18.2 kHz) in compare to Case 2 (with monokinetic atoms).

hybrid models. One species is modeled with fluid equations, and the other is kinetic (e.g. fluid electrons with neglected inertia are common for such low-frequency models). Typically, full kinetic simulations for plasma thrusters require some speed-up techniques, such as artificial increase of dielectric permittivity, an increase of electron to ion mass ratio, geometrical downscaling [77, 78, 79, 80], all to overcome numerical constraints and resolve low-frequency dynamics. Full kinetic (particle-in-cell) 2D axial-azimuthal model (with the artificial increase of dielectric permittivity) reproduces the low-frequency ionization oscillations with no assumptions made on anomalous electron transport coefficients (electron current develops self-consistently via azimuthal drift instabilities), presented in Ref. [81]. Note that the radial coordinate may introduce important modifications to the azimuthal drift mode (excitation of large scale MTSI modes) with an influence on the anomalous electron transport [40, 41, 42]. Thus, ideally, the detailed model of electron transport will be reproduced in a 3D simulation.

In this paper, low-frequency plasma dynamics in the axial direction of a Hall thruster are studied with full fluid and hybrid (kinetic/fluid) models. The model parameters are taken close to those of the LANDMARK benchmarking project [36]. We identified and distinguished two low-frequency oscillations regimes: one is subject to the low-frequency

53

oscillations only, and another with both low frequency and high frequency (time of ion flyby oscillations) components. Another distinct feature is the extent of the ion backflow region: in the case with the pure low-frequency component, the ion backflow on average is about half of the channel length, while for the regime where two modes coexist, it is much shorter, Fig. 2.2a. These regimes are observed in fluid and hybrid models and presented as Cases 1 and 2 in the numerical experiments. Finally, Case 3 illustrates the effects of finite atom temperature.

The main difference between the full fluid and hybrid model results, as expected, is caused by the different approaches in heavy species modeling. The kinetic method for heavy particles in the hybrid model automatically includes effects of the non-equilibrium distribution function (i.e. higher fluid moments effects, only limited by statistical noise errors of the PIC approach). However, as seen from the results, a simple fluid model for both ion and atom components (first two moments) is well sufficient to reproduce the main results and capture breathing mode frequency and the resistive mode presence.

It is found that in Case 1 (regime with co-existence of low- and high-frequency modes), the finite value of ion pressure played a notable role in oscillatory behaviour. Ion temperature is often assumed negligible in Hall thrusters operation (similar to a neutral temperature, up to about $1000\,\mathrm{K}$ or $0.1\,\mathrm{eV}$), thus it was not included in the primary fluid model. Using kinetic representation from the hybrid model, we show that the ion momentum balance without the ion pressure was notably violated. Thus the ion pressure term (with constant temperature) was added into the fluid model. It resulted in a better conformity between the two models. Nevertheless, both fluid and hybrid models predicted the existence of two modes in this configuration even without the ion pressure in the fluid model, suggesting that these oscillations are the so-called resistive modes [50, 64]. We believe these modes are observed in the models without electron pressure, many of which were done in the primary studies and modeling of the axial dynamics of Hall thrusters [7, 50]. We conjecture that the resistive modes of high frequencies play an important role in the excitation of the low-frequency modes.

For Case 2, which shows only the low-frequency oscillations, we already performed extensive studies, Ref. [48], where we identified that the mechanism of these oscillations lies in the ion backflow region (presheath) and that they can be additionally reinforced with the

plasma recombination. This led to the observation that the difference in the ion boundary conditions at the anode played a crucial role in our benchmark. Bohm velocity for ions in the fluid model generated a larger atom yield (due to recombination, Eq. (2.17)) from the anode in comparison to the hybrid model where this velocity was unconstrained and found to be smaller on average (thus leading to smaller atom yield). Modifying the ion velocity boundary condition in the fluid model (replacing the Bohm condition with a free boundary condition) resulted in better conformity between the two models. Similar to the previous case, we conclude that the main physical behaviour was identified in both models even without this modification.

Finally, in Case 3, with finite atom temperature in the hybrid model but the same values of other parameters as in Case 2, it is shown that the advection equation in the fluid model, Eq. (2.1), with the constant flow velocity is not sufficient to describe atom dynamics. An effect of selective ionization of neutral particles is observed in this case, where average macroscopic velocity increased more than twice along the channel. Thus, the fluid model was supplemented with the atom momentum balance equation (2.25), which resulted in a better agreement between the two models, reproducing the selective ionization effect. Though it resulted in a completely stationary solution, the hybrid model preserved the breathing oscillations (with similar frequency to Case 2) but with a much smaller amplitude.

In summary, benchmarking of the fluid and hybrid models show very close agreement for averaged plasma parameters profiles. Both models reveal the existence of the two different regimes of the low-frequency oscillations in Hall thrusters. While qualitatively, the two regimes are identifiable in both models, there are some quantitative differences in the frequencies and the amplitude of the oscillations. These differences are attributed to the ion finite thermal (pressure) effects which were not originally included in the fluid model. Account of the finite ion pressure improves the agreement. The finite temperature (energy) spread of the neutral atoms provides a strong stabilizing effect on the oscillations. These results highlight limitations of the fluid models that have to be considered in future modeling of practical devices.

2.A   Resistive modes

Here we present the cases with more prominent resistive modes and show their effect on the ion heating, which is the extension to Case 1. It is found that the larger value of the anomalous (electron) energy loss frequency, $\nu_{\varepsilon,\text{in}} = 1.2 \times 10^7\,\text{s}^{-1}$, leads to the solution where the resistive mode dominate, see Fig. 2.23a. It reveals larger amplitude and clearly distinct high-frequency oscillations (168 kHz), with the small low-frequency modulation (14.4 kHz), Fig. 2.23b shows its spectrum. As it was demonstrated for Case 1, ion temperature effects were not negligible, and ions were heated to a few electron volts. We noticed that the average ion temperature is higher with presence of the resistive modes as shown in Fig. 2.22, where the resistive modes appear for values $\nu_{\varepsilon,\text{in}} = 0.9\,\text{s}^{-1}$ and higher.
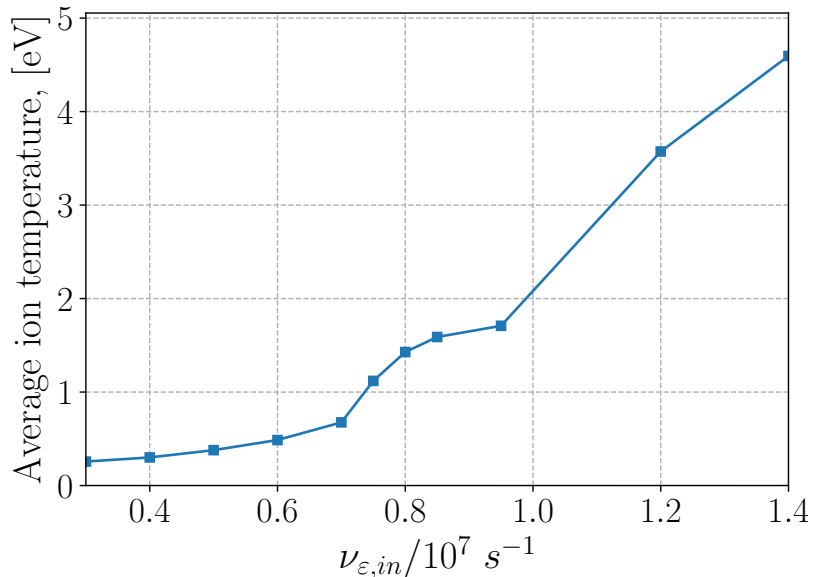
Figure 2.22: Ion average thermal energy as a function of the anomalous electron energy loss coefficient. As we move into regime with resistive modes present (studied in Case 1), ion heating increases and ion pressure effects may become important.
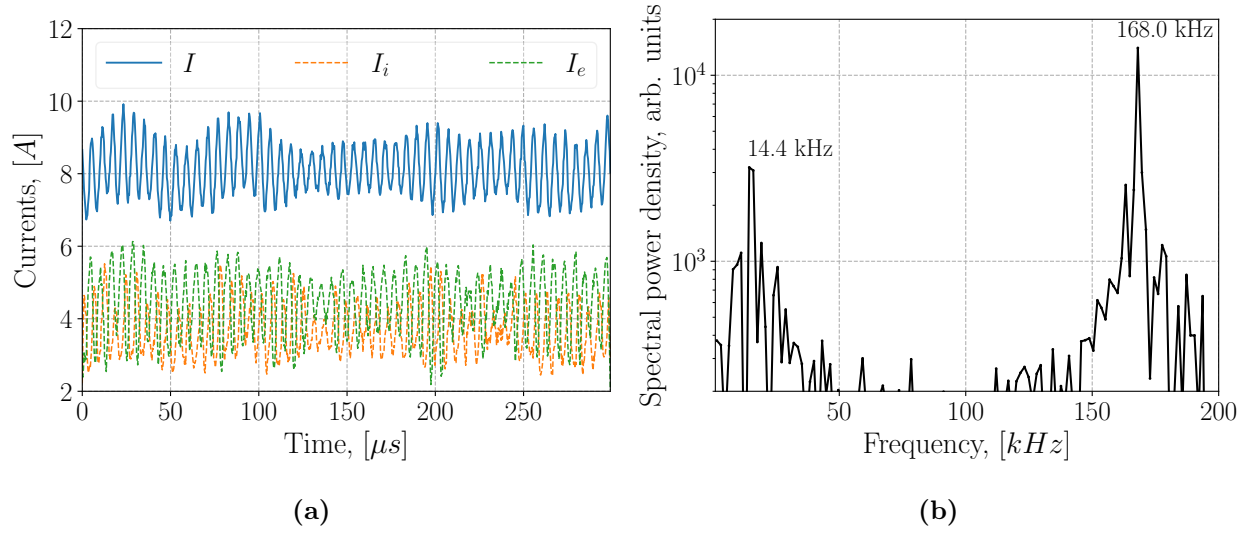
Figure 2.23: Currents (a) and the total current spectra (b).
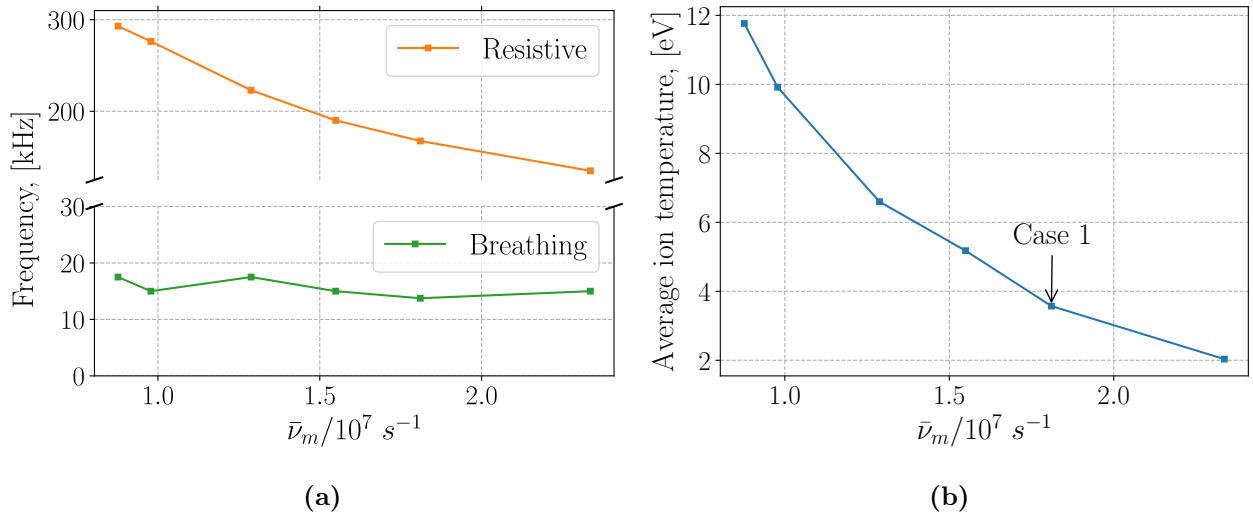
Figure 2.24: Frequency of breathing and resistive modes as a function of averaged (over time and space inside the channel) total electron momentum exchange frequency $\bar{\nu}_m$ (a). Average ion temperature (in time and whole domain) as function of $\bar{\nu}_m$ (b). The parameter varied in this study was the anomalous Bohm coefficient $\beta_{a,in}$ inside the channel, directly affecting the total electron frequency, Eq. (2.11).

Now, we show that the frequency of the resistive mode scales with the average electron collision frequency $\bar{\nu}_m$, Fig. 2.24a, and thus the higher electron mobility $\sim 1/\bar{\nu}_m$ leads to

the higher frequencies. At the same time, the ion heating effect is stronger for the higher frequency of resistive modes, Fig. 2.24b. It is interesting to note that the breathing mode frequency stays approximately the same, Fig. 2.24a, along with the size of the presheath region.

2.B Ionization rate and energy loss functions
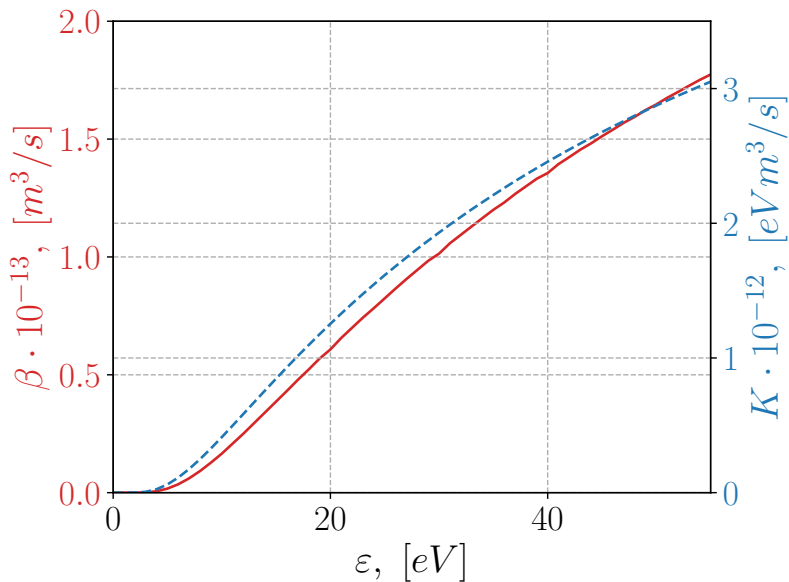
Figure 2.25: Ionization rate β and electron ionization energy loss coefficient K.

The ionization rate $\beta(\varepsilon) = \langle \sigma(v)v \rangle$ as a function of electron energy ε is obtained by averaging over Maxwellian EEDF with the cross-sections from the SIGLO database [82]. The collisional energy loss coefficient $K(\varepsilon)$ is generated by BOLSIG+ [83] as a table-valued function. Both functions are shown in Fig. 2.25.

2.C Normalization scheme for fluid model

The system length L_0 and a typical ion-sound velocity $c_s = \sqrt{T_e/m_i}$ (for $T_e = 20\,\text{eV}$) are chosen as basis for normalization, they form the characteristic frequency $f_0 = c_s/L_0$.

Densities are normalized to the neutral density at the anode $N_0 = n_a(0, t)$ without the recombination (thus). Normalization scheme:

$$t^* = f_0 t, \ x^* = \frac{x}{L_0}, \ E^* = E \frac{eL_0}{m_i V_0^2}, \ j^* = \frac{j}{eN_0 V_0}, \ \mu_e^* = \mu_e \frac{m_i f_0}{e}, \ \beta^* = \frac{\beta N_0}{f_0}$$

Acknowledgments

CHAPTER 3

ON THE MECHANISM OF IONIZATION OSCILLATIONS IN HALL THRUSTERS

3.1 Preface

This chapter aims to bring light on one of the possible mechanisms of the breathing mode. In the previous Chapter, a purely breathing mode regime (corresponding to Case 2) was reproduced in the fluid and hybrid models. Here we show a clear connection between the existence of the ion backflow region (due to presheath near the anode) and excitation of the breathing mode. We briefly describe a hierarchy of the simple reduced models based on 0-D predator-prey dynamics. We point out the importance of axial coordinate dynamics where spatial profiles (like ion velocity with backflow region) play a crucial role. We introduce the reduced fluid model based on the continuity equations for ions and atoms (provided fixed velocity and ionization profiles). The material presented in this Chapter is published in the Journal of Applied Physics [48].

3.2 Abstract

Low frequency ionization oscillations involving plasma and neutral density (breathing modes) are the most violent perturbations in Hall thrusters for electric propulsion. Because of its simplicity, the zero-dimensional (0-D) predator-prey model of two nonlinearly coupled ordinary differential equations for plasma and neutral density has been often used for the characterization of such oscillations and scaling estimates. We investigate the properties of its continuum analog, the one-dimensional (1-D) system of two nonlinearly coupled equations

in partial derivatives (PDE) for plasma and neutral density. This is a more general model, of which the standard 0-D predator-prey model is a special limit case. We show that the 1-D model is stable and does not show any oscillations for the boundary conditions relevant to Hall thruster and the uniform ion velocity. We then propose a reduced 1-D model based on two coupled PDE for plasma and neutral densities that is unstable and exhibit oscillations if the ion velocity profile with the near the anode back-flow (toward the anode) region is used. Comparisons of the reduced model with the predictions of the full model that takes into account the self-consistent plasma response show that the main properties of the breathing mode are well captured. In particular, it is shown that the frequency of the breathing mode oscillations is weakly dependent on the final ion velocity but shows a strong correlation with the width of the ion back-flow region.

3.3 Introduction

Hall thrusters are electric propulsion plasma devices with cross-field $\mathbf{E} \times \mathbf{B}$ configuration, where electrons are effectively trapped by the magnetic field, and heavy ions are accelerated by the electric field generating thrust. Despite the long history and a large number of successful missions, as well as the relatively simple design of these devices, many physical phenomena are not well understood. Large amplitude discharge current oscillations in the axial direction of Hall thrusters, or the so-called breathing modes, are among the most strong perturbations that affect the operation, e.g. with current oscillations reaching 100% and even extinguishing the discharge [84]. The physics of the breathing mode has been studied in many papers but the full understanding is far from complete. Simulations of low-frequency axial dynamics of Hall thrusters were done earlier with various approximations, including fluid [7, 60, 55], and hybrid [7, 53, 85, 50, 76] (fluid electrons and kinetic ions and atoms) models. Ionization is one of the key physics elements of the breathing mode oscillations. In addition to the basic coupling of plasma density and neutral gas due to the ionization, many models include self-consistent electric field calculations along the channel, and some models include electron pressure evolution and detailed electron energy balance.

At the same time, a simple zero-dimensional (0-D) model was proposed [45, 46] to explain

the mechanism of breathing mode, in which neutral and ion (plasma) densities are coupled in the form of predator-prey model (Lotka-Volterra equations). The predator-prey model is a system of two nonlinearly coupled ordinary differential equations that describes periodic oscillations in a number of physics and biology systems. This model is claimed to predict the frequencies close to the observed in experiments. It was, however, noted that for the constant ion and neutral velocities, the model is stable and does not predict any instability [47] so the conditions for the excitation of the ionization oscillations are not clear. Additional effects and modifications [47, 86] were proposed for the predator-prey model to make it unstable but it remains unclear to what degree the 0-D models are capable to predict the breathing mode oscillations (discussed in section 3.4).

Nevertheless, simple reduced models are of considerable interest. First, such models are useful as scaling tools, e.g. for the design of power supply sources. Another motivation stems from the considerable complexity of the full models. In the full models with many parameters that are unknown experimentally, it is rather difficult to predict the conditions for the instability and therefore difficult to translate the predictions of the theoretical models into practical recommendations. The search for physical mechanism (or mechanisms) and critical controlling parameters continues [87]. Reduced models focusing on selected specific phenomena may allow easier experimental validation and eventually lead to a better understanding of the physics of the instability, its conditions, and the development of the full predictive model(s) [88, 89].

In this work, we analyze the properties of the continuum one-dimensional (1-D) model, based on two coupled partial differential equations (PDE) for the evolution of neutral and plasma densities. The 0-D predator-prey is a reduction of the 1-D model. If anything, the more complete 1-D model should exhibit the same physics (and e.g. predict similar characteristics of the oscillations) if the reduction from the 1-D to the 0-D model is appropriate for the relevant physics, and the oscillations in the 0-D model are not the artefact introduced by the simplifications. We show, however, that the 1-D model is not only stable with boundary conditions of a typical Hall thruster and the standard assumptions of the *uniform velocity* (as it is used in 0-D model) but also does not show the oscillations observed in the 0-D model. On the contrary, any oscillations, even introduced externally, are damped in time and space.

We then propose a modified 1D model with a non-uniform ion velocity profile and with a back-flow (toward the anode) the region near the anode. We show that such a model is unstable and exhibit ionization oscillations with characteristics roughly consistent with the predictions of the full fluid model [90]. Rather good agreement of the results of the reduced (simplified) and full models suggests that the reduced model captures well essential physics relevant to the breathing mode and may point to the critical conditions for the instability.

The paper is organized as follows. In section 3.4, various modifications of the 0-D model are discussed. In section 3.5, the continuum 1-D model is introduced. The stationary solutions are obtained here, their stability and response to external perturbations are discussed for the uniform profile of the ion velocity. Section 3.6 presents a reduced 1-D continuum model with the ion back-flow region near the anode and shows that this model exhibit unstable nonlinear oscillations. In section 3.7, the predictions of the reduced model are compared against the full self-consistent simulations.

3.4 Zero-dimensional (0-D) predator-prey models

In this section we discuss the various modifications and properties of the zero-dimensional (0-D) predator-prey models for the ionization oscillations. Such a simplest model includes basic time and space dynamics of plasma and neutrals and is based on the continuity equations for the ion density n_i (assuming full plasma quasineutrality), and neutral atom density n_a:

$$\frac{\partial n_a}{\partial t} + v_a \frac{\partial n_a}{\partial x} = -\beta n_a n_i, \tag{3.1}$$

$$\frac{\partial n_i}{\partial t} + \frac{\partial}{\partial x}\left(n_i v_i\right) = \beta n_a n_i, \tag{3.2}$$

where v_i, v_a are ion and atom flow velocities, respectively, and β is the ionization rate coefficient. We assume that v_a is a constant, but v_i and β, in general, could be non-uniform in space. A basic assumption leading to a simple zero-dimensional predator-prey model [45] is that the ionization zone and acceleration zone is replaced by the transition layer of the width L. The integration of Eqs. (3.1)-(3.2) over this region results in the system of ordinary

differential equations (ODE):

$$\frac{\partial}{\partial t} \langle n_a \rangle + \frac{1}{L} (n_a v_a)|_0^L = -\beta \langle n_a n_i \rangle, \tag{3.3}$$

$$\frac{\partial}{\partial t} \langle n_i \rangle + \frac{1}{L} (n_i v_i)|_0^L = \beta \langle n_a n_i \rangle, \tag{3.4}$$

where averages over the transition layer are defined as $\langle (...) \rangle = L^{-1} \int_0^L (...) \, dx$ and β is assumed constant here. A set of approximations are made to obtain the original predator-prey model [45]. First, the ion and neutral fluxes at the boundaries of the transition layer are assumed in the form: $(n_i v_i)|_0 = 0$, $(n_i v_i)|_L = n v_i$ and $(n_a v_a)|_0 = n_a v_a$ and $(n_a v_a)|_L = 0$, where v_i is the final ion velocity and $n(t)$ is plasma density at the exit of the transition layer, at $x = L$, $n(t) \equiv n_i(t, L)$, and $N(t)$ is neutral density at $x = 0$, $N(t) \equiv n_a(t, 0)$. Thus, these boundary conditions imply full ionization, $n_a(L) = 0$, zero flux of the ions from the left boundary, $(n_i v_i)|_0 = 0$, and full acceleration the transition layer, $(n_i v_i)|_L = n v_i$. Then, the boundary values for the plasma and neutral densities are used to approximate the averages over the transition layer: $\langle n_a n_i \rangle \simeq nN$, $\langle n_a \rangle \simeq N$, and $\langle n_i \rangle \simeq n$. These steps lead to the 0-D ODE system [45]

$$\frac{dN}{dt} - \frac{1}{L} N v_a = -\beta N n, \tag{3.5}$$

$$\frac{dn}{dt} + \frac{1}{L} n v_i = \beta N n. \tag{3.6}$$

These equations have the equilibrium solution with $n_{eq} = v_a/L\beta$ and $N_{eq} = v_i/L\beta$. Considering the perturbations $\left(\widetilde{n}(t), \widetilde{N}(t) \right) \sim \exp\left(-i\omega t\right)$ near the equilibrium, $n = n_{eq} + \widetilde{n}(t)$, $N = N_{eq} + \widetilde{N}(t)$ one obtains stable oscillations with

$$\omega^2 = \beta^2 n_{eq} N_{eq} = v_i v_a / L^2 \tag{3.7}$$

It was later noted [46] that oscillations (time dependence) in N are inconsistent with the constant mass rate boundary condition at $x = 0$, $(n_a v_a)|_0 = N v_a = \dot{M}/A m_a = const$, which means that the N should be constant for the constant neutral flow velocity; A is the cross-section area. A modification of the 0-D model was suggested in Ref. [47] where the value of neutral density at the left (entrance) side was fixed constant, $(n_a v_a)|_0 = N_0 v_a$, and the value at the exit was assumed time dependent, $(n_a v_a)|_L = N(t) v_a$, so the neutral balance equation takes the form

$$\frac{dN}{dt} + \frac{1}{L} (N - N_0) v_a = -\beta N n. \tag{3.8}$$

The plasma balance equation was also modified with an additional term due to the sheath losses at the lateral walls

$$\frac{\mathrm{d}n}{\mathrm{d}t} + \frac{1}{L}nv_i + \frac{1}{d}nc_s = \beta N n, \tag{3.9}$$

where sheath losses are estimated based on the Bohm condition for the ion velocity, where d is the radial channel width and $c_s = \sqrt{T_e/m_i}$. With these modifications, the equilibrium value of the neutral density in equations (3.8-3.9) is only corrected by the sheath losses,

$$N_{eq} = \frac{1}{\beta}\left(\frac{v_i}{L} + \frac{c_s}{d}\right), \tag{3.10}$$

while the equilibrium value of plasma density can be very different from that in equation (3.5) and takes the form

$$n_{eq} = \frac{v_a}{\beta L}\left(\frac{N_0}{N_{eq}} - 1\right). \tag{3.11}$$

Note that in this model, the value of the neutral density at $x = 0$ should be sufficiently large $N_0 > N_{eq} = (v_i/L + c_s/d)/\beta$. Considering perturbations near N_{eq} and n_{eq} one obtains damped oscillations [47]

$$\omega = -\frac{i}{2}\frac{v_a}{L}\frac{N_0}{N_{eq}} \pm \sqrt{\beta^2 n_{eq} N_{eq} - \frac{1}{4}\left(\frac{v_a}{L}\right)^2 \left(\frac{N_0}{N_{eq}}\right)^2}. \tag{3.12}$$

The essential problem of the predator-prey model is that it does not predict instability so no condition for the oscillations can be determined. It was argued that the electron dynamics should be important and more complex models were proposed such as using the electron (instead of ion) continuity equation with the drift-diffusion approximation for the electron velocity [91, 92, 93], ion flows [86], electron energy evolution [47, 94], and two-zone model [88, 89]. Ref. [95] provides an overview of various models and involved mechanisms.

3.5 Continuum (1-D) predator-prey model

Ideally, the reduction from the continuous 1-D model to the 0-D models as was discussed in the previous section should preserve the essential properties and features of the more complete model and do not introduce any fundamental changes to the 1-D model. Therefore, is of interest to study if the 1-D model has the properties predicted by the 0-D models. Here we discuss properties of the stationary and time-dependent solutions of the one-dimensional

(continuous) model consisting of the continuity equations (3.1) and (3.2) for atoms and ions with constant flow velocities v_a and v_i, and the ionization rate β. These are the same assumptions with which the original predator-prey model was derived. The stationary problem is formulated as two coupled equations:

$$v_a \frac{\partial n_a}{\partial x} = -\beta n_a n_i, \tag{3.13}$$

$$v_i \frac{\partial n_i}{\partial x} = \beta n_a n_i. \tag{3.14}$$

The exact solution to this system is found in the form:

$$n_{a,st}(\xi) = n_{a0} \left(1 + \frac{n_0 v_i}{n_{a0} v_a} \right) \frac{1}{(n_0 v_i)/(n_{a0} v_a) \exp(\xi) + 1}, \tag{3.15}$$

$$n_{i,st}(\xi) = n_0 \left(1 + \frac{n_{a0} v_a}{n_0 v_i} \right) \frac{\exp(\xi)}{\exp(\xi) + (n_{a0} v_a)/(n_0 v_i)}, \tag{3.16}$$

where n_0, n_{a0} are values of ion density and atom density, respectively, at the left boundary, and normalized length is $\xi = x/l_0$, with $l_0 = v_i v_a / \beta (n_0 v_i + n_{a0} v_a)$. It can be noted that the solutions of the stationary problem depend only on two parameters, n_0, n_{a0}. Typical stationary solutions for $v_i/v_a = 10$ are depicted in Figs. 3.1a and 3.1b by solid lines. Note that the position of the crossing point, where the ion and neutral densities are equal, and the localization of the ionization source $\beta n n_a$ depend on the value n_0: they move to the right with decreasing n_0, and goes to infinity for $n_0 \to 0$.

Numerical studies of the time-dependent equations (3.1) and (3.2) were performed with fixed boundary values at the left n_0, n_{a0} and free boundary conditions (spatial second derivative is zero) on the right end. This analysis shows that all perturbations are damped and converge to the stationary solutions given by equations (3.15) and (3.16), as shown in Fig. 3.1a at different times. Thus, the 1-D predator-prey model with a constant spatial profile of the ion velocity does not exhibit oscillatory or unstable behaviour, unlike zero-dimensional predator-prey models. The 1-D continuum model presented here in some sense is similar to the asymptotic low-frequency model derived in the limit $n/N_a \ll 1$ [46, 55], which also predicts the neutral oscillations with the frequencies of the order of given by equation (3.7). Contrary to [46, 55], our model does not show neutrally stable oscillations but only damped modes.

66

(a) $n_0/n_{a0} = 0.05$, $l_0 = 1.31\,\mathrm{cm}$ **(b)** $n_0/n_{a0} = 0.0001$, $l_0 = 1.96\,\mathrm{cm}$
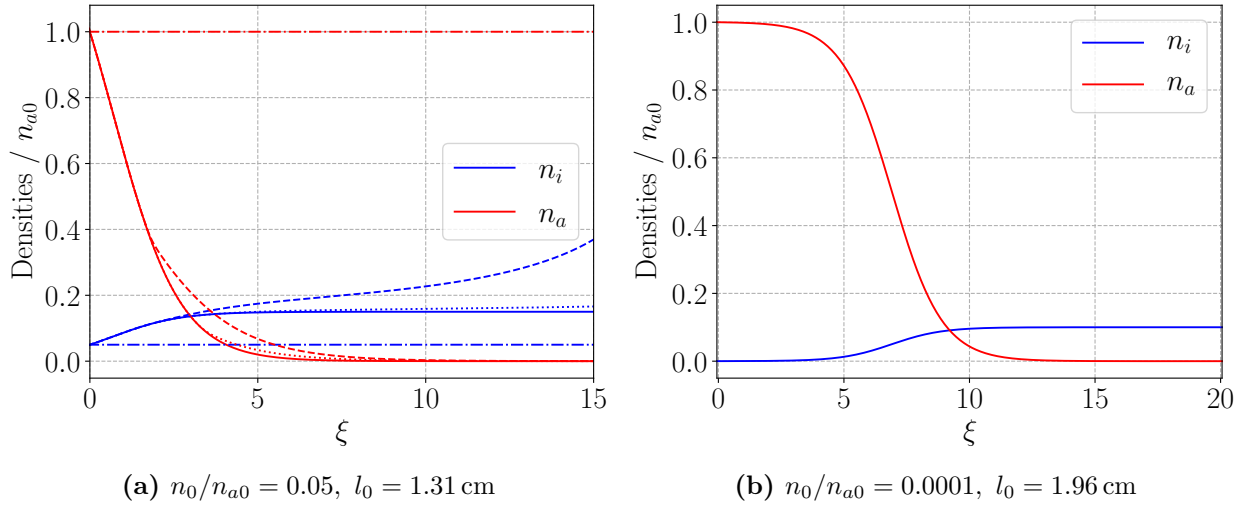
Figure 3.1: Stationary solutions given by Eqs. (3.13) and (3.14) are shown by solid lines, with higher (a) and lower (b) ion density at the left boundary n_0. The time dependent solutions of Eqs. (3.1), and (3.2), converging to the stationary solution are shown for the case (a) at three consecutive time steps $t_1 < t_2 < t_3$, dot dashed (initial condition), dashed, and dotted line, respectively.

One can envisage that the boundary value of plasma density could be perturbed, e.g. by some sheath instability. Such perturbations may also arise in the experiments with segmented anode [96], external modulations of the anode voltage [97], and two-stage thruster configurations [98]. Therefore, it is interesting to investigate how this nonlinear system responds to external perturbations of the ion density and whether such external perturbations may grow in amplitude while propagating from the left boundary. We will impose harmonic external modulations of the ion density at the left boundary in the form $n_i(0) = n_{i0}\left(1 + r\sin 2\pi f_{ext} t\right)$, where f_{ext} is the modulation frequency, with $r = 0.15$. We consider the 1-D continuum model, Eqs. (3.1,3.2) with $v_i = 10v_a$, $n_{i0}/n_{a0} = 0.05$, $l_0 = 1.31\,\mathrm{cm}$, Fig. 3.1a, with the simulation length $15l_0$. Since velocities of neutrals and ions are different, there are two natural modes that can be excited during the external modulations, with the wavelengths given with $\lambda_a = v_a/f_{ext}$ and $\lambda_i = v_i/f_{ext}$. We consider four values of the driving frequencies $f_{ext}l_0/v_a = (0.1, 0.5, 1, 10)$. For these values, the corresponding natural wavelengths of the neutral and ion characteristic wavelengths are $\lambda_a = (10, 2, 1, 0.1)l_0$ and $\lambda_i = (100, 20, 10, 1)l_0$, respectively.

The resulting response of the system of Eqs. (3.1,3.2) under the external modulations of

(a) $f_{ext}l_0/v_a = 0.1$

(b) $f_{ext}l_0/v_a = 0.5$

(c) $f_{ext}l_0/v_a = 1$
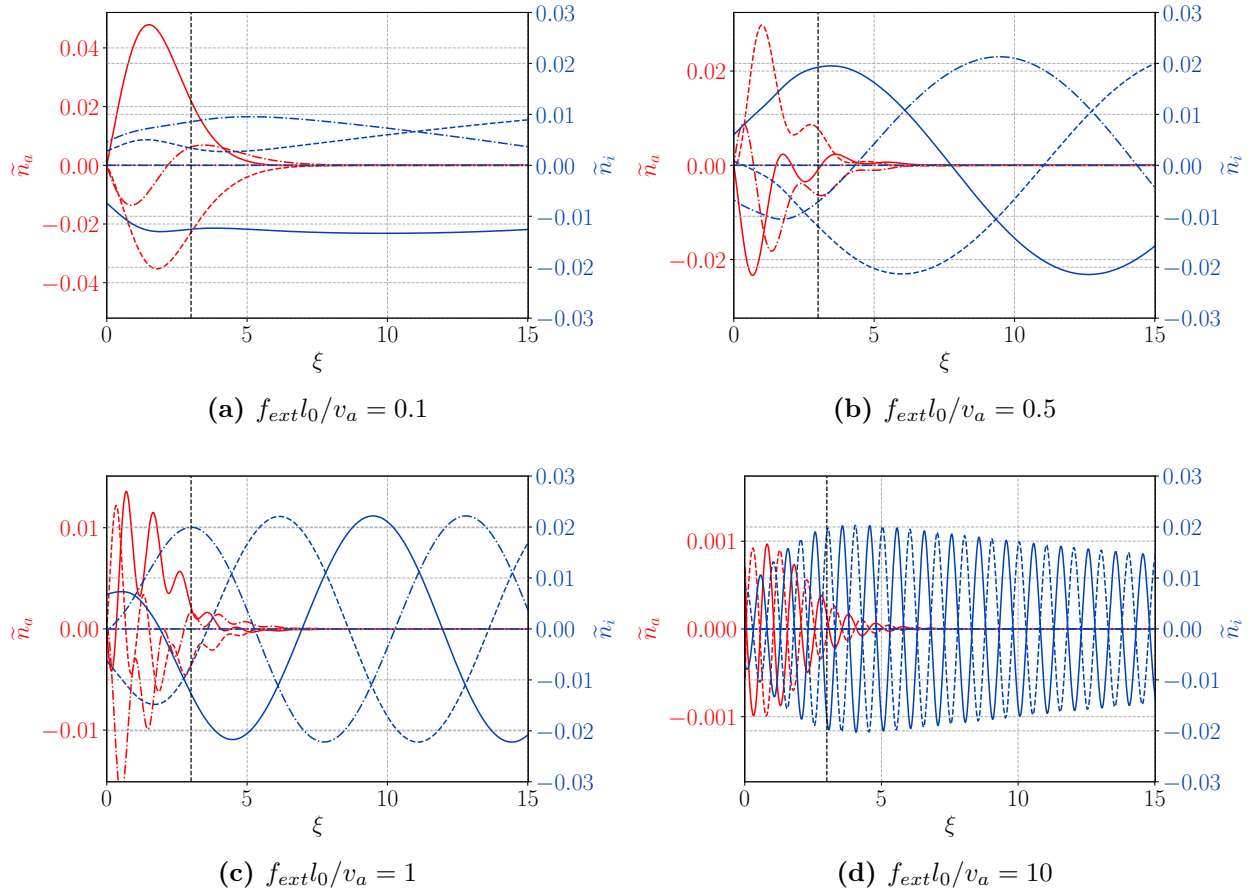
(d) $f_{ext}l_0/v_a = 10$

Figure 3.2: Instantaneous profiles of perturbed ion $\widetilde{n}_i$ (blue) and neutral $\widetilde{n}_a$ (red) densities for the various driving frequencies $f_{ext}l_0/v_a = (0.1, 0.5, 1, 10)$, shown, respectively, in (a), (b), (c), (d). Three consecutive time snapshots $t_1 < t_2 < t_3$ are shown for each variable, depicted with the dot dashed line, dashed line, and solid line, respectively; they divide one oscillation period in 3 equal intervals. Crossing point (of stationary ion and atom densities profiles) location is shown with the black dashed line.

the ion density is presented in Fig. 3.2 for the perturbed variables, defined as $\widetilde{n} = n - n_{st}$, where n_{st} is the corresponding stationary solution. It can be noted that in all cases ion density perturbations grow in absolute values before reaching the crossing point and leaving the ionization region, whereas the amplitude of neutral density perturbations decays, which is expected in the ionization region. Note that while the absolute value of the perturbations of the ion density seems increasing, the relative value $\widetilde{n}/n_{st}$ does not grow. Thus, in the presence of external ion density perturbations in the near-anode region, the system exhibit externally driven oscillations that are advected along the channel but show a limited increase of the amplitude. However, the atom response is slightly more complicated and besides the natural mode can exhibit the nonlinear response (on ion natural wavelength). It is also affected by the atom stationary profile (Fig. 3.1a), as atom perturbations decay rapidly after the crossing point. It is seen that for the low frequency perturbations the natural atom mode is excited (Fig. 3.2a), while for the higher frequencies the ion characteristic wavelengths become more and more dominant in the atom response (seen gradually through Figs. 3.2b-3.2d). We remind that the amplitude of the ion density perturbations was fixed in these cases. The amplitude of the neutral density perturbations is maximal for the lower frequencies. We have also investigated the case when the neutral density was modulated at the left boundary. Such a system shows similar behaviour and does not show the unstable modes.

3.6 Ionization oscillations in the 1-D continuous model with the ion back-flow in the near anode region

As it was discussed in the previous section, the reduced fluid model, described with Eqs. (3.1, 3.2), with spatially uniform profiles of v_i, v_a, and β is stable. Here we will show that the same system with spatial dependence of v_i, when v_i is negative near the anode, the so-called ion back-flow, becomes unstable and exhibit self-consistent oscillations. The ion back-flow region naturally forms in the presheath, a quasineutral region near the anode with the negative electric field due to the electron diffusion [67, 68, 69, 70]. The positive density gradient near the anode creates a strong electron flow to the anode. To maintain ambipolarity (the total current remains uniform), the ion back-flow current occurs to compensate the increase of the

electron current. The current ambipolarity is required to keep plasma quasineutral. This process is somewhat similar to the formation of the electric field in the presheath region near the plasma boundary where the electric field is induced to accelerate ions toward the boundary (up to the Bohm velocity) to balance electron and ion losses.

In this configuration the only fixed boundary condition is a value of the neutral density on the left, as their characteristics travel strictly to the right (atom velocity is a positive constant). Ion density boundary condition is free on the left, $\partial_x^2 n_i(0) = 0$. First, we consider the simple configuration with the velocity profile v_i as a strictly linear function of the position. The ionization rate β is taken uniform. One might argue the constant β is an unrealistic assumption for a typical Hall thruster where electron energy near the anode is low due to higher mobility, shaping the β profile; we consider these effects in Section 3.7 in the comparison with the full fluid model. Recombination of plasma at the anode is not included here: the ion flux converted to the neutral flux at the anode is not added to the neutral flow. It can also be included, increasing the amplitude of oscillations, but it is not required for the existence of the oscillations. An example of such oscillations shown for a typical Hall thruster parameters (the stationary plasma thruster "SPT 100" [7]), with the channel length 3 cm, ionization rate $\beta = 9 \times 10^{-14}\,\mathrm{m^3 s^{-1}}$, $v_a = 150\,\mathrm{m/s}$. Atom density at the anode n_{a0} is fixed according to $n_{a0} v_a = \dot{m}/A m_a$, assuming $\dot{m} = 5\,\mathrm{mgs^{-1}}$, Xenon atom mass, and $A = 12.75\pi\ \mathrm{cm^2}$. For the simplicity, we assumed the linear ion flow velocity profile $v_i = (2.5x - 1.5)$ km/s (x is in [cm]), with the ion back-flow extent $L_b = 0.6$ cm. The resulting time and space evolution of ion and atom densities is shown in Fig. 3.3. The observed frequency is 12.8 kHz, in the range of the values observed in experiments and simulations for breathing mode.

Now, for the same setup with ion velocity profile in the form $v_i = (2.5x - 1.5)$ km/s (x is in [cm]), we will show effects of the amplitude of the ionization rate β, which is still assumed uniform here for simplicity. The ionization rate coefficient β needs to be sufficiently large to support plasma discharge. Interestingly, in addition to a threshold β value for the discharge to exist, there is also a threshold between stable and oscillatory plasma behaviour. In the oscillatory regime, there is a value of β when the amplitude of the oscillations is the largest (note that here we assume that β is constant along the channel). It shouldn't be of surprise,
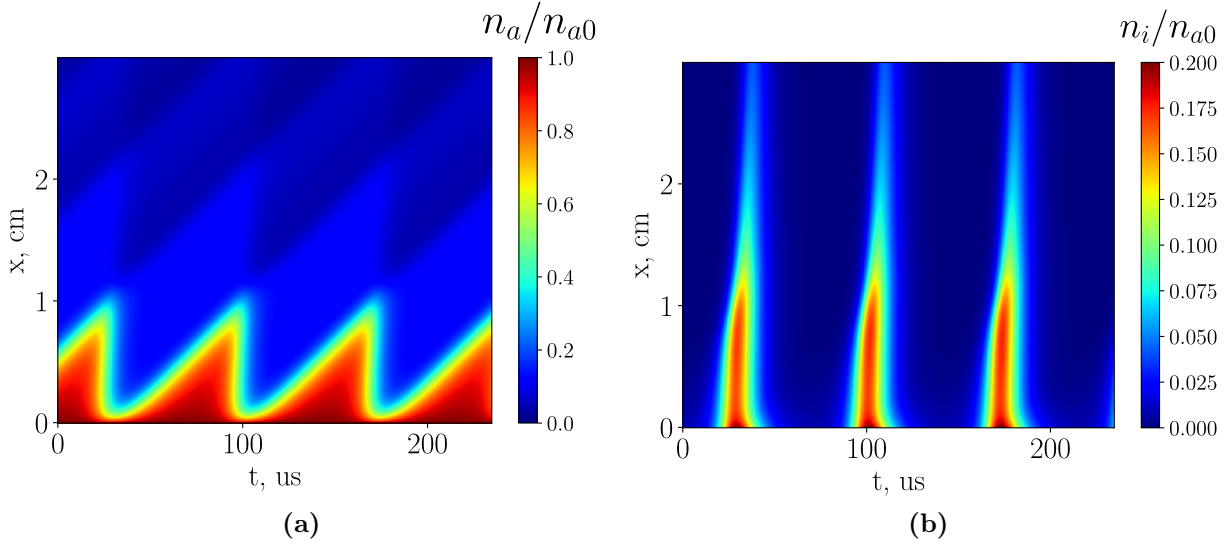
Figure 3.3: Evolution in space and time of atom (a) and ion (b) density, normalized to n_{a0}.

as when the values of β are too high, the ionization takes place immediately near the left end and so both density profiles have maximum values at the left end. The dependency of the oscillation amplitude on β is shown in Fig. 3.4a, where the peak-to-peak amplitude of the averaged in space density $\langle n_i \rangle_x(t)$ is shown.

The frequency dependence on β is presented in Fig. 3.4b. If the ion back-flow region is very short, i.e. $v_i(0) \approx 0$, the ionization mostly will occur at the anode for the same reasons, and there would not be enough spatial separation between high and low atom density points. Dependencies, similar to those shown in Figs. 3.4a and 3.4b, are also observed for different values of the ion back-low extent L_b. They follow the same scaling as presented below in Figs. 3.5b and 3.6.

The effect of the ion back-flow region is investigated further for our reduced model by taking the ion velocity profiles with a variable ion back-flow extent. The Fig. 3.5a shows the velocity profiles taken as parabolas specified with the three points, $v_i(0) = -1.5\,\text{km/s}$, $v_i(L) = 20\,\text{km/s}$, and $v_i(L_b) = 0\,\text{km/s}$, where L_b is the length of the ion back-flow region, the distance from the anode to the transition point where the ion velocity reverse its sign. The value of L_b was varied, with the system length set to $3\,\text{cm}$, the ionization rate $\beta = 5 \times 10^{-14}\,\text{m}^3/\text{s}$, atom flow velocity $v_a = 150\,\text{m/s}$. Simulations using these velocity profiles reveal that oscillation

71
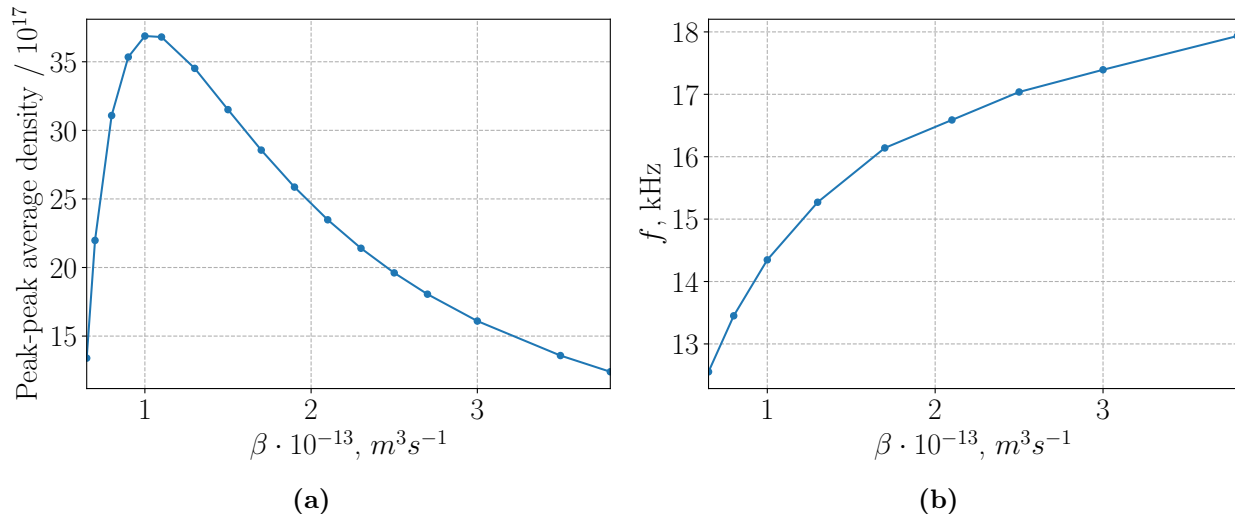
Figure 3.4: Peak-to-peak values of averaged in space ion density $\langle n_i \rangle_x(t)$ as a function of ionization rate (a). The main frequency component of observed oscillations as a function of the ionization rate (b).

frequency scales with the atom fly-by frequency v_a/L_b in the back-flow region, Fig. 3.5b. The oscillations amplitude decreases with decreasing L_b and the oscillations disappear for $L_b \to 0$, as shown in Fig. 3.6. Also, no oscillations were observed for monotonically increasing ion velocity profiles with $v_i(0) \geq 0$.

Zero-dimensional predator-prey models predict that the frequency depends on the exhaust ion velocity. Here, we show that for our model this effect is very small and, mostly, the back-flow region "defines" the frequency. Fig. 3.7a shows the family of the ion velocity profiles, constructed in a similar manner (by a parabola) but keeping the back-flow length the same $(1\,\text{cm})$ and varying $v_i(L) = (14, 18, 22, 26)$ km/s. The resulting frequency for all these profiles was found to be close to 10 kHz, Fig. 3.7b, predicted by the previous example in Fig. 3.5b with the $L_b = 1\,\text{cm}$.

The mechanism of the oscillations can be considered in three main stages, starting from a stationary state in Fig. 3.1a, but with the ion velocity back-flow region. In the first stage we observe enhanced ionization process in the region of plasma stagnation ($v_i \approx 0$). The ionization process in this stage may be approximated as $\dot{n}_i = \beta n_i n_a$, $\dot{n}_a = -\beta n_i n_a$ (where n_i, n_a are some average plasma and atom densities, respectively, in that region). In this stage, effects of atom inflow and ion outflow are relatively small here. The ionization

(a)

(b)
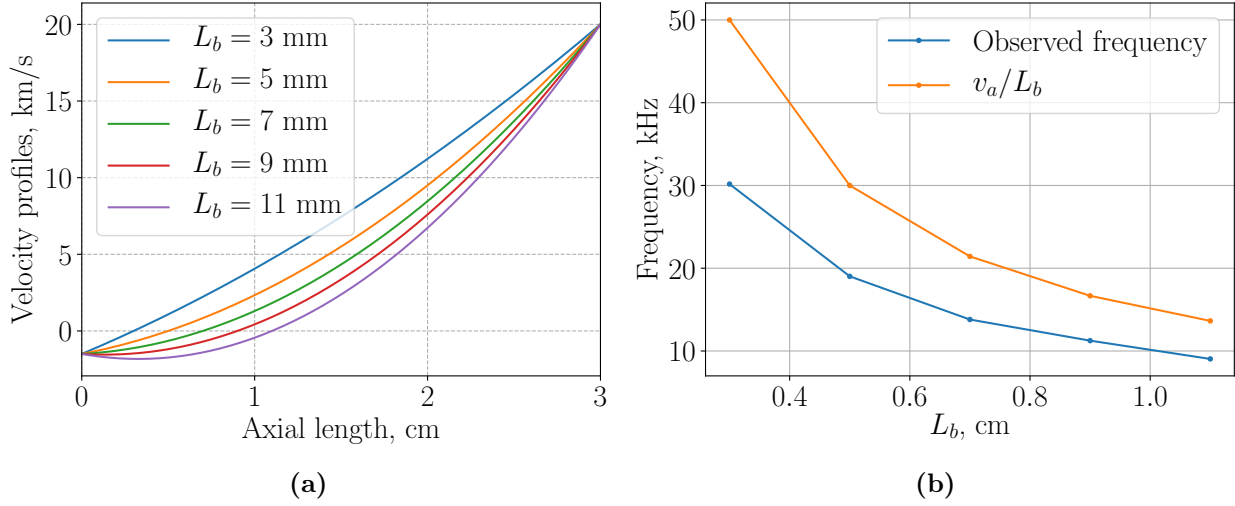
Figure 3.5: Velocity profiles (a) for a variable ion back-flow region L_b while the exhaust velocity is fixed to $20\,\mathrm{km/s}$ ($300\,\mathrm{eV}$ is a typical ion energy in the exhaust plume of SPT100 [7]). The corresponding frequency (b) as a function of L_b in compare with neutral flyby frequency of v_a/L_b in the backflow region.
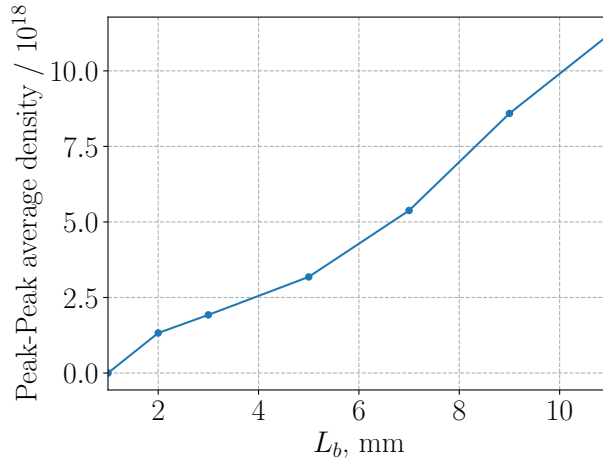
Figure 3.6: Peak-to-peak values of averaged in space ion density $\langle n_i \rangle_x(t)$ as a function of the ion back-flow region L_b. Oscillations disappear as $L_b = 1\,\mathrm{mm}$ goes to zero.
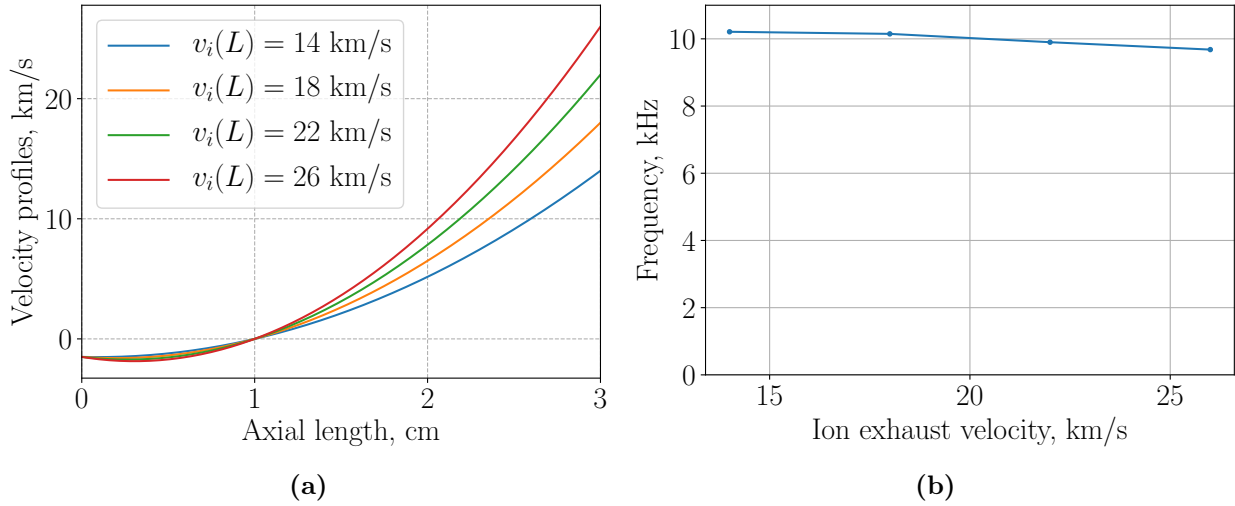
Figure 3.7: Velocity profiles (a) and corresponding frequency (b) as a function of $v_i(L)$, for the variable ion exhaust velocity $v_i(L)$ while keeping the back-flow region L_b constant.

proceeds with the exponential rise plasma density $n_i \sim \exp(\beta n_a t)$ and depletion of atom density. In the second stage, the newly created plasma peak splits and partially moves to the anode (via back-flow) wiping down the rest of atoms near the anode. Finally, in the third stage, the system enters the period of "regeneration" with both plasma and atom densities low, while atoms slowly fill the region near the anode. The atom density remains higher than the ion density, and the ion density balance is predominantly follows the equation $\dot{n}_i = \beta n_i n_a - \gamma_{loss} n_i$, where $\gamma_{loss} n_i$ represents the ion advection losses via the back-flow. In this quasistationary state, there is no exponential rise of ionization but slow inflow of atoms (to the right) filling this region toward the stagnation region. The third stage is also the slowest and defines the breathing mode period, hence the backflow lengths defines the period (Fig. 3.5b). Additionally, if the recombination at the anode is included, it increases a number of atoms injected to the system for the stage three, and it increases the amplitude of the oscillations.

3.7 Reduced vs full self-consistent model

In this section we compare the reduced and full models for the breathing modes, and demonstrate that our simple reduced model, Eqs. (3.1,3.2), reproduces well the results from the full self-consistent time-dependent model [90]. First, we give a brief description of the full fluid self-consistent model for low-frequency ionization oscillations.

3.7.1 Full self-consistent model

The full model of low-frequency axial plasma dynamics in Hall thruster is considered in electrostatic and quasineutral approximation for three species: neutrals, ions, and electrons. Our model is fully fluid both for the ion, neutral, and electron components. The electron equations in general are similar to those used in Refs. [53, 55]. The full fluid model consists of time-dependent PDE equations for neutral atom density n_a, plasma density n (ion and electron), ion flow velocity v_i, and electron temperature T_e:

$$\frac{\partial n_a}{\partial t} + v_a \frac{\partial n_a}{\partial x} = -\beta n_a n, \tag{3.17}$$

$$\frac{\partial n}{\partial t} + \frac{\partial}{\partial x}(n v_i) = \beta n_a n, \tag{3.18}$$

$$\frac{\partial v_i}{\partial t} + v_i \frac{\partial v_i}{\partial x} = \frac{e}{m_i} E + \beta n_a (v_a - v_i), \tag{3.19}$$

$$\frac{3}{2} \frac{\partial}{\partial t}(n T_e) + \frac{5}{2} \frac{\partial}{\partial x}(n v_{ex} T_e) + \frac{\partial q_e}{\partial x} = n v_{ex} E - n n_a \mathrm{K} - n \mathrm{W}, \tag{3.20}$$

where the electric field E is obtained from the electron momentum balance equation

$$v_{ex} = -\mu_e E - \frac{\mu_e}{n_e} \frac{\partial(n T_e)}{\partial x}, \tag{3.21}$$

obtained with neglected electron inertia, where μ_e is the electron mobility across the magnetic field (described below). Quasineutrality condition, along with the constraint $\int_L E dx = U_0$ (U_0 is the applied potential) leads to the total current $J_T = en(v_i - v_e)$

$$J_T = \frac{U_0 + \int_0^L \left(\frac{v_i}{\mu_e} + \frac{1}{n} \frac{\partial p_e}{\partial x} \right) dx}{\int_0^L \frac{dx}{en\mu_e}}, \tag{3.22}$$

75

which is spatially uniform but may oscillate in time. Other quantities in the system (3.17-3.20) are the constant atom flow velocity v_a, the ionization rate coefficient β (obtained with BOLSIG+ [83] for Maxwellian EEDF using SIGLO database [82]), the elementary charge e, the electron mass m_e, the ion (Xenon) mass $m_i = 131.293\,\mathrm{amu}$, the anomalous energy loss coefficient [53] W, the collisional energy loss coefficient K (also via BOLSIG+), and the electron heat flux given by

$$q_e = -\frac{5}{2}\mu_e n T_e \frac{\partial T_e}{\partial x}.$$
(3.23)

The electron transport across magnetic field is described in the form of the magnetized mobility

$$\mu_e = \frac{e}{m_e \nu_m} \frac{1}{1 + \omega_{ce}^2/\nu_m^2},$$
(3.24)

where ν_m the total electron momentum exchange collision frequency, $\omega_{ce} = eB/m_e$ is the electron cyclotron frequency. In this model ν_m is represented in the form as was adopted in Ref. [52],

$$\nu_m = \nu_{en} + \nu_{walls} + \nu_B,$$
(3.25)

where the electron-neutral collision frequency ν_{en}, electron-wall collision frequency ν_{walls}, and anomalous Bohm frequency ν_B are given with:

$$\nu_{en} = k_m n_a,$$
(3.26)

$$\nu_{walls} = \alpha 1 \times 10^7 \,[\mathrm{s}^{-1}],$$
(3.27)

$$\nu_B = (\beta_a/16)\, eB/m_e.$$
(3.28)

where $k_m = 2.5 \times 10^{13}\,\mathrm{m}^{-3}\mathrm{s}^{-1}$, α and β_a are adjusting constants. The profile of external magnetic field B is shown if Fig. 3.8a, with the channel's exit in the peak of magnetic field intensity, given by $B = B_0 \exp\left(-(x - l)^2/2\delta_B^2\right)$, where $l = 2.5\,\mathrm{cm}$ is the channel length and δ_B defines a magnetic field profile width. This model use different parameters inside $(x < l)$ and outside $(x \geq l)$ the channel [61, 52, 99], the near wall conductivity contribution (3.27) $\alpha_{in} = 0.2$, $\alpha_{out} = 0$, and the anomalous contribution (3.28) is set to $\beta_{a,in} = 0.1$, $\beta_{a,out} = 1$. The anomalous electron energy loss coefficient [53] W is modeled as

$$\mathrm{W} = \nu_\varepsilon \varepsilon \exp\left(-U/\varepsilon\right),$$
(3.29)

76

where $\varepsilon = 3/2T_e$, $U = 20\,\mathrm{V}$, and ν_ε is electron energy anomalous loss coefficient. A constant mass flow rate $\dot{m}$ determines the value of n_a at the boundary together with the recombination of plasma that flows to the anode, hence the boundary condition:

$$n_a(0) = \frac{\dot{m}}{m_i A v_a} - \frac{n v_i(0)}{v_a}, \qquad (3.30)$$

where A is the anode surface area of a thruster. Bohm type condition for ion velocity can be imposed at the anode $v_i(0) = -b_v\sqrt{T_e/m_i}$, where $b_v = 0$–1 is the Bohm velocity factor which can be varied. Both anode and cathode electron temperature are fixed with $T_e(0) = T_e(L) = 2$ eV. All other boundary conditions are free (spatial second derivative is zero).

Following the LANDMARK benchmark [36] Test Case 3, we use the parameters that result in bulk low-frequency oscillations, with the electron energy anomalous loss coefficient inside the channel $\nu_{\varepsilon,\mathrm{in}} = 10^7$ s^{-1} and outside $\nu_{\varepsilon,\mathrm{in}} = 0.4 \cdot 10^7$ s^{-1}. The resulting plasma currents evolution shown in Fig. 3.8b, assuming the typical inner and outer radius of a Hall thruster ("SPT 100" [7]) $R_1 = 3.5\,\mathrm{cm}$, $R_2 = 5\,\mathrm{cm}$, respectively. The input atom mass flow used in the simulation is $\dot{m} = 5\,\mathrm{mgs}^{-1}$ corresponds to $I = \dot{m}q_e/m_i = 3.67\,\mathrm{A}$. The average ion current (to the exit plane) is $3.68\,\mathrm{A}$ which is consistent with the mass flow rate. The electron current (to the exit plane) is of the same order (or slightly larger). Other simulation parameters for this test case are: $\delta_{B,in} = 1.1\,\mathrm{cm}$, $\delta_{B,out} = 1.8\,\mathrm{cm}$, $A = \pi(R_2^2 - R_1^2)$, $b_v = 1$.

The self-consistent fluid model used here is essentially based on the formulations and parameters suggested in Refs. [53, 60, 52, 99], also see the LANDMARK benchmark [36]. The fluid model has been compared against the hybrid model [52, 100]; both models demonstrate similar results [90].

3.7.2 Comparison of the reduced model with predictions of the full self-consistent model

We compare now results of the full fluid model (in the regime described above), with the reduced model. In the full model the ion velocity profile v_i and the ionization rate β profile are self-consistent variables, and for the reduced model we take averaged in time profiles of these variables, Figs. 3.9a and 3.9b. We also include the ion back-flow recombination to the
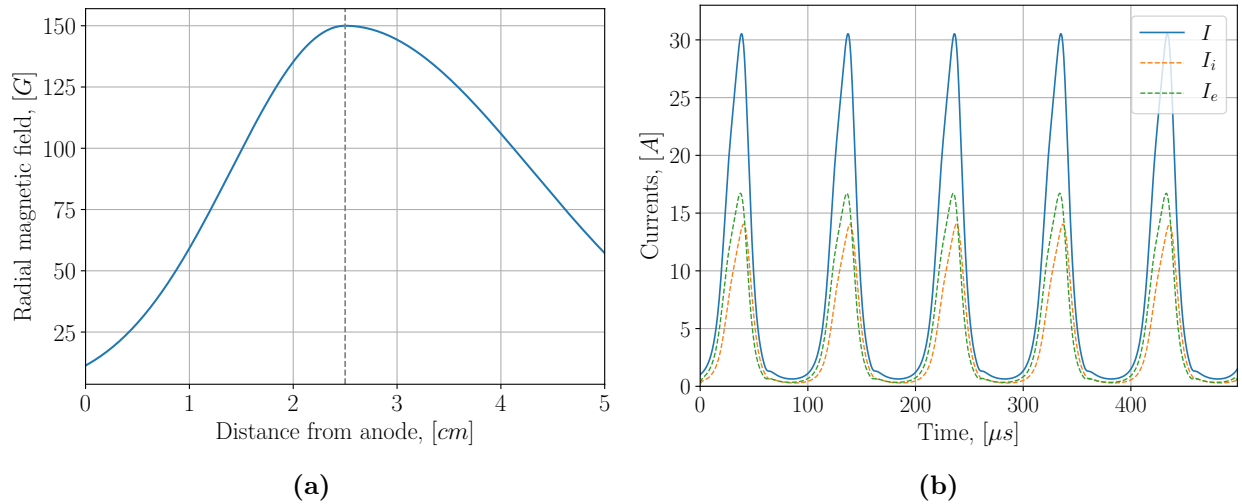
Figure 3.8: The magnetic field profile (a) used in full fluid and hybrid simulations, with the channel exit located 2.5 cm from anode (dashed line). Low-frequency oscillations in time (b) of total current I, ion current I_i (at $x = 5$ cm), and electron current I_e (at $x = 5$ cm) in the full fluid model using specified parameters.

atom boundary condition at the anode in the reduced model, described by Eq. (3.30), in agreement with the full model.

Time evolution of n_a, n_i, and the source $S = \beta n_a n_i$, are shown in Figs. 3.10a, 3.10d, and 3.10g, respectively. The same quantities from the reduced model are shown in Figs. 3.10b, 3.10e, and 3.10h. It is seen that the reduced model results in oscillatory behaviour, qualitatively reproducing the breathing mode oscillations, but with much higher amplitudes (about one order) of evolving variables. The observed natural frequency in this model is also higher, 14.9 kHz, compared to 10.2 kHz in the full model.

The observed discrepancy can be explained by the absence of the electron temperature evolution and lack of self-consistent ionization rate dynamics in the reduced model which is known to affect the breathing mode characteristics, e.g. Ref. [101]. One observation is that the average position of the source term S in our reduced model is closer to the anode (Fig. 3.10h) (compared with the full model) that results in higher frequency. Higher amplitude may also be explained by the shift of the ionization source toward the region with higher ion back-flow velocity so that more ions return to the anode and recombine enhancing the positive feedback loop. We found that simply lowering the values of the ionization rate, precisely by taking 0.82β of the original averaged β profile (shown in Fig. 3.9b) agrees with
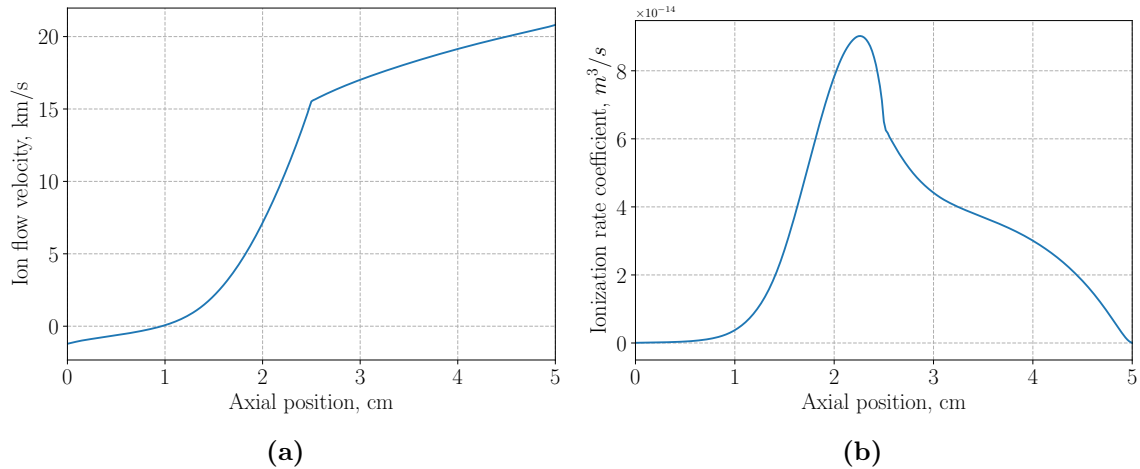
Figure 3.9: Ion velocity (a) and ionization rate (b) coefficient profiles obtained from the full fluid model as time-averaged over a few oscillation periods. They are used in the reduced model as fixed profiles in time.

the full model much closer, see Figs. 3.10c, 3.10f, and 3.10i, with the oscillation frequency of 11.8 kHz. While our intention is not really to achieve full quantitative agreement, this exercise shows the sensitivity to the temperature effects. It is also possible that the strong nonlinear dependence of the ionization rate on temperature may suggest some weighting average for the ionization rate. We leave the investigation of the proper averaging technique for future work.

To show that the atom velocity v_a plays a defining role in the observed oscillation frequency, the full and reduced model (lower β) were compared against each other, Fig. 3.11. Both full and reduced (with lower β) model show approximately linear behaviour for the frequency, again suggesting the feedback loop mechanism supported by ion back-flow and advection of the neutral atoms. Interestingly, the ion current amplitudes are comparable between the full and reduced (lower β) models, Fig. 3.12.

3.8   Discussion and conclusions

In this paper, we have proposed a reduced continuum 1-D model with the ion velocity profile that has an ion back-flow (toward the anode) region. The model consists of two one-dimensional equations for coupled dynamics of the ion and neutral densities. While the 0-D
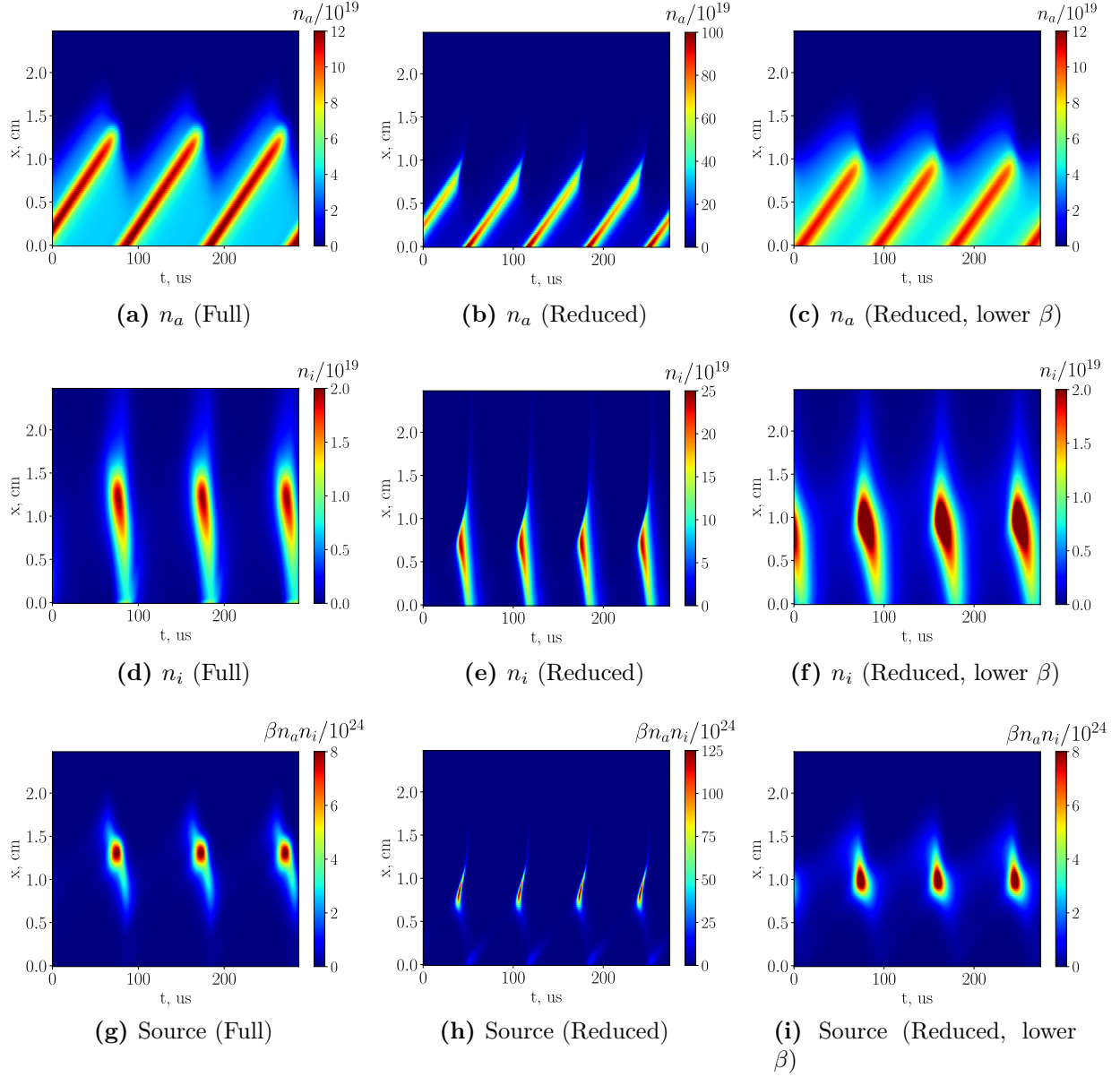
Figure 3.10: Neutral density (a,b,c), ion density (d,e,f), and ionization source $\beta n_i n_a$ (g,h,i) for the full fluid model, the reduced model, and the reduced model with lower values of β (see captions). Density values are normalized to $1 \times 10^{19}\,\mathrm{m}^{-3}$, and source values to $1 \times 10^{24}\,\mathrm{m}^{-3}\mathrm{s}^{-1}$. The spatial domain is limited to channel region only, $2.5\,\mathrm{cm}$ from the anode.
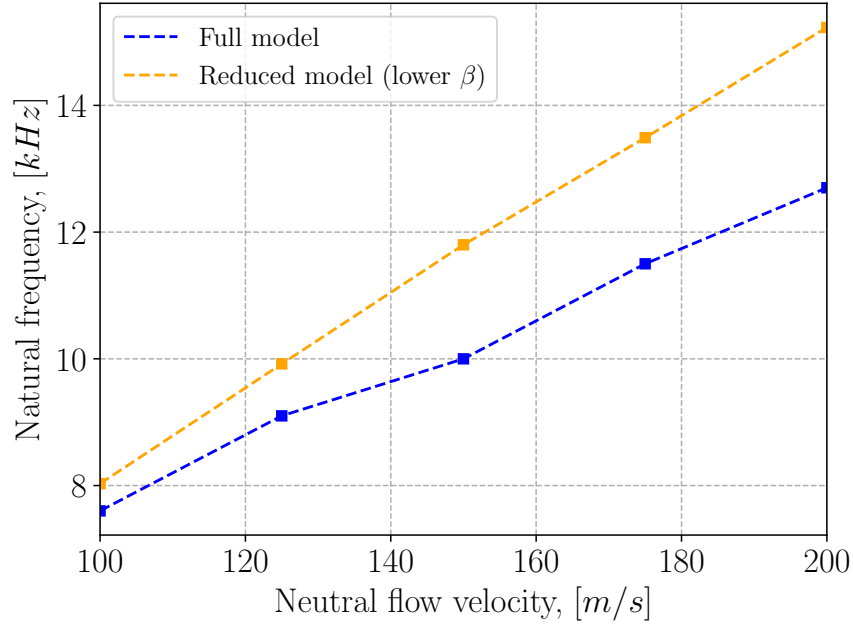
Figure 3.11: Oscillation frequency as a function of neutral velocity in full and reduced (with lower β) fluid models.

(a) (b)
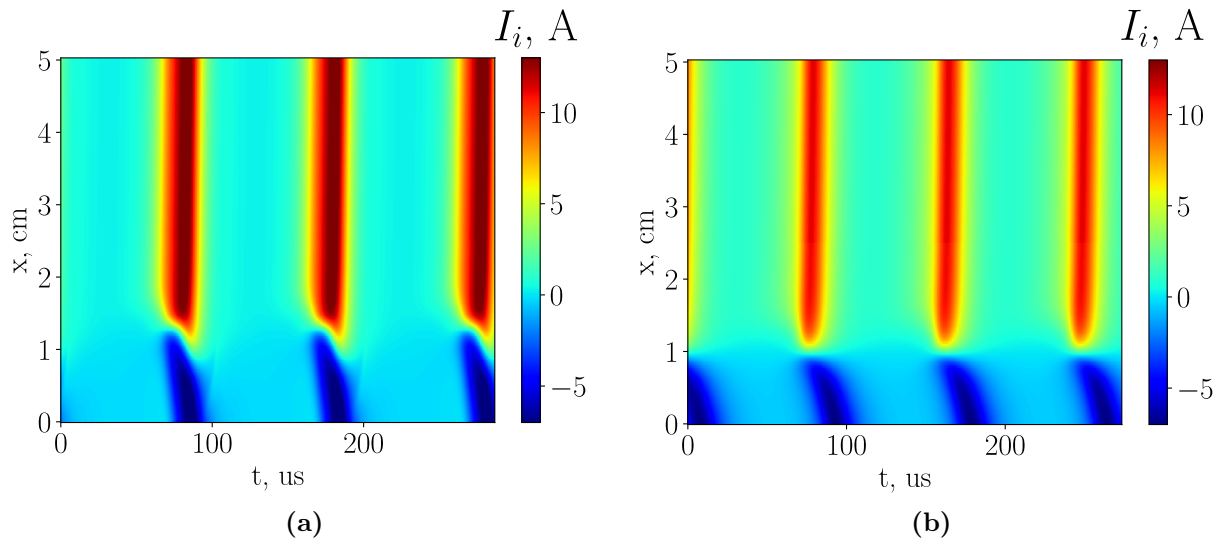
Figure 3.12: Temporal and spatial ion current dynamics in full model (a) and reduced model with lower β (b), in Amperes (assuming cross section area $A = 12.75\pi$ cm^2).

simplification of this model, commonly referred to as the predator-prey model, shows the oscillations, the continuum 1-D model with a uniform ion velocity and boundary conditions typical of Hall thruster show damped modes converging to the analytical stationary state. Under externally imposed perturbations at the left boundary, the 1-D continuum model shows limited convective amplification of the perturbation (in the region where the local value of the neutral density is smaller than plasma density) and subsequent convection (with a slow amplitude decay) where the ion and neutral density perturbations are mostly decoupled. Therefore the models with the uniform ion velocity, in the absence of additional effects e.g. such as temperature variations [47], do not predict the excitation of the breathing modes.

The key element of the proposed continuum model is the ion velocity profile that has an ion back-flow (toward the anode) region. As it is shown here, such a system becomes unstable and shows self-consistent nonlinear oscillations. The comparison between this reduced model and the full self-consistent fluid model shows very similar characteristics for oscillations of the ion and neutral densities, and ion current. We have investigated the scaling of the frequency and amplitude of the oscillations as a function of the width of the back-flow region and neutral flow velocity which show generic v_a/L_b dependence both in the reduced and full models. These results suggest that the presence of the ion back-flow region may be a critical condition for the breathing mode oscillations and the overlap of this region with the ionization region creates the closed feedback loop necessary for the instability. These results also indicate that the electron dynamics, in particular diffusion, which leads to the appearance of the back-flow region, is important for the breathing mode. A number of full models, reporting the breathing mode oscillations, include the electron diffusion either explicitly via the electron fluid equations, such as full fluid [55] or hybrid [52] formulations, or via full kinetic treatment as in the full kinetic (particle-in-cell) treatment [81]. The ion back-flow near the anode occurs as a result of the electron diffusion ensuring the current conservation to maintain quasineutrality. The ion stagnation in the back-flow region triggering enhanced ionization is suggested as the mechanism for the instability. It is also worth noting that the electron diffusion is also a reason for the appearance of the singular sonic point where the ion velocity is equal to the local sound velocity, $v_i = c_s$. The smooth (regular) solution is obtained when the sonic point is made regular by imposing some constraints on the current, mass flow

rate, and plasma parameters. These constraints made singular point regular and play an important role for the existence and characteristics of stationary solutions [69, 67, 102, 51]. As it was shown in [90, 103] the constraints indeed define the stability of the resulting profile and characteristic frequency of the breathing mode.

One has to note, however, that low frequency ionization oscillations were also observed in the models without the electron diffusion, and hence, without back-flow region [53, 104, 105, 106, 76]. It has been suggested [50] that the high frequency oscillations due to the resistive axial modes [50, 107, 108] is a driving mechanism for a breathing mode. Alternative mechanisms may be based on the temperature dependence of the ionization coefficient [47], other electron temperature effects [109], and/or more complex interactions between the low frequency modes involving ionization and higher frequency modes in the ion transit time frequency range as it was suggested earlier [110, 90]. The simulations with the full model also demonstrate the existence of two different regimes of the breathing mode [90], the so-called solo regime, where only the low frequency mode present, and the regime with coexisting low frequency and the high frequency ion transit time oscillations. The breathing mode oscillations reproduced by our reduced model are similar to the solo regime, but are different from the modes coexisting with high-frequency ion transit time oscillations. The existence and nature of the breathing mode together with the well pronounced high-frequency mode is an interesting question that will be addressed in future studies with the full model.

In summary, we would like to conclude that the importance of the reduced models is not only in their ability to predict reasonably well some essential features of the ionization modes in Hall thrusters but also, and perhaps, even more importantly, in pointing to some important physics involved in the modes excitation and characteristics. The reduced models typically involve a smaller number of adjustable parameters compared to the full models, e.g. as the values of the anomalous mobility are poorly known. Therefore, the tests of the properties and consequences of the reduced models in the experiments [97, 88, 89, 87] could be an effective approach to test the crucial physics responsible for the breathing modes oscillations.

Acknowledgments

Chapter 4

Plasma flow in the magnetic mirror with a recycling wall

4.1 Introduction

Large linear fusion devices often use the magnetic expander (diverging magnetic field) on its ends to distribute the output heat loads over the larger area [111]. It is called a divertor for a linear fusion device. It serves a similar purpose as divertors in closed toroidal systems but with a simpler construction and it is easily scalable for higher power outputs. The schematic of a linear fusion device with the divertor and the wall is shown in Fig. 4.1, where the "source" (or core) represents an arbitrary plasma confinement configuration, e.g. field-reverse configuration (FRC) [112]. Hot plasma from the source leaks and accelerates through the mirror throat and hits the wall. The direct electric contact with a material wall can be used to control the overall potential (called biasing) and improve stability and confinement [111]. This study aims to reproduce the possible dynamical plasma flow effects in magnetic expander on time scales of ion bounce motion in such divertor configuration (neglecting ion gyro-rotation and higher frequencies), especially due to the effects associated with neutral atoms and collisions. Charge exchange (CX) and ionization create additional ion sources in the near-wall region and lead to a turbulent behaviour (instability caused by counter-streaming ions). Since we are not accounting for a detailed electron model, possible effects of electron-electron streaming instabilities can not be observed. Slow plasma beams near the wall decrease the overall potential drop and may lead to increased electron heat losses (due to lower potential barrier entrapping electrons inside the core) and cooling of the core plasma [113]. A closed particle drift in axisymmetric magnetic configurations, or the rotation in the

azimuthal direction (may cause azimuthal currents and diamagnetic effects), is not taken into account.

The light ions bombarding the material wall can induce a whole zoo of neutral atoms of various energies. First, ions can be reflected via the backscattering from the material surface, returning predominantly in the neutral state [114]; in our model, they all assumed neutral. These reflected neutrals are of relatively high energy (which is some fraction of bombarded ion energy), and thus we will call them energetic neutrals. Then, the cold atoms and molecules are emitted via the desorption process. Desorbed atoms are of the wall temperature and thus constitute the cold component. Desorbed molecules may undergo ionization and their further dissociation creating the so-called Franck-Condon atoms, of $1\,\mathrm{eV} - 4\,\mathrm{eV}$ energy (about the energy of dissociation). In the energy range, Franck-Condon atoms stand between cold atoms (of wall temperature) and energetic atoms due to reflection. Cold atoms have a larger tendency to accumulate in the near-wall region. The CX and ionization can effectively create a source of cold ions and electrons near the wall flowing in the opposite direction (to the original plasma flow from the core). It is shown that a sufficiently dense cold ion beam (in the opposite direction to the original ion flow) triggers an instability that results in turbulent behaviour near the wall. As for the energetic neutral atoms, they quickly leave the system without significant effects on the plasma flow (due to its low density).

In the present study, we focus on a more accurate model of atom yield from the recycling wall and the study of its effects on the plasma flow. For this purpose, a simple and fast hybrid model was developed that includes drift-kinetic ions, kinetic neutral atoms, and fluid (Boltzmann) electrons. The plasma flow is modeled in the paraxial approximation [115], resolving the particle dynamics along the magnetic field line with two-dimensional effects (such as acceleration due to mirror force) via the conservation of magnetic flux. It includes an emitting source (diffusive or specular reflection) for ions, model of atom recycling from the material wall with the main atom sources, and the most probable collision processes (CX and ionization). Heavy particles are modeled with the particle-in-cell (PIC) method. The collision processes are simulated with the direct simulation Monte Carlo (DSMC), which, for ion-neutral collisions (CX) occurs self-consistently with their distribution function shapes, according to the supplied cross-section information. For ionization, the constant collision
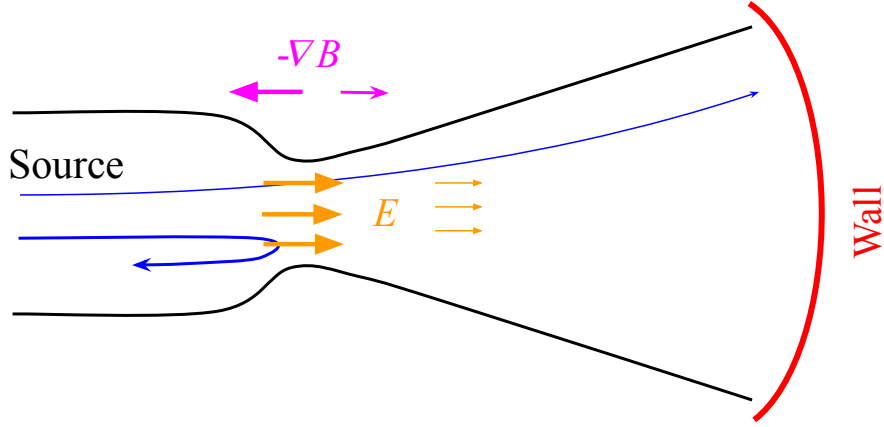
Figure 4.1: Magnetic divertor region schematic for a linear fusion device. Plasma escaping the throat of the mirror expands and reaches the wall. Magnetic mirror force confines the source particles and accelerates those escaping into the expander. Quasineutral plasma forms the electrostatic potential (shown in orange), increasing ion losses and confining electrons. Ions showed schematically with blue trajectories.

rate is assumed due to isotropic electrons. For a large part of the simulated domain, mean free paths for collision processes will be large, on the scale of system size and higher; thus, the DSMC method is justified in this regime.

This model is implemented in Fortran and MPI. The initial version was inspired by the hybrid code developed by G. Hagelaar (LAPLACE, France) for the axial simulation of Hall thrusters (used in Sec. 2). It was rewritten and adapted for the plasma acceleration in a magnetic nozzle by M. Jimenez. It was later rewritten from scratch with added parallelization and other features by two of us. The atom transport and DSMC collisions (CX and ionization) were added as a part of my internship project at TAE Technologies.

4.2   Hybrid drift-kinetic model

Plasma flow is considered in the one-dimensional flux tube with the variable cross-section in the so-called paraxial approximation, where the radial component of the magnetic field B_r is much smaller than the axial B_z. The model accounts for two-dimensional effects related to compression and decompression of the plasma flux tube close to the axis. Electrons are considered in the Boltzmann approximation with full plasma quasineutrality over the whole
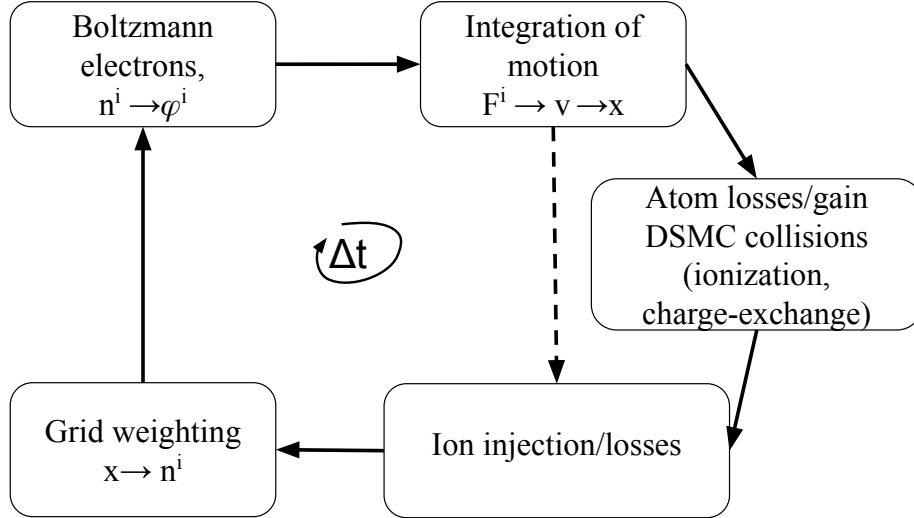
Figure 4.2: Main steps for one time iteration in the hybrid drift-kinetic model. DSMC module usually skips some number of time steps (if collision frequencies are low).

domain (missing sheath potential drop), thus we focus on low-frequency plasma dynamics. We consider ions in the drift-kinetic approximation, i.e. following its gyrocenters on time scales larger than the ion gyro-frequency (averaged over gyrofrequency), and on spatial scales larger than the ion gyroradius (neglecting gyroradius effects). The time scale of interest here is the bounce motion of an ion in the large magnetic nozzle system, $\tau \sim v_z/L$, e.g. for ion energies $\sim 100\,\text{eV}$ and $L \sim 1\,\text{m}$, $\tau \sim 1\,\mu\text{s}$. We assume that the magnetic moment is well conserved for ions i.e. $\rho_i < L_B \equiv (\nabla B/B)^{-1}$ (magnetic field is close to homogeneous per single ion rotation).

A single time iteration consists of injection of ions, evaluating plasma density, calculating the potential profile via the Boltzmann relation, and integrating particle motions. When the ions reach the material wall, neutral atoms are emitted in accordance with the atom transport model (see Section 4.2.3). Collisions are processed at the constant time steps Δt_{coll} (which is typically larger than the simulation time step), but we let collisional cells coincide with the PIC cells of size Δx^1. Schematic representation of time iteration is shown in Fig. 4.2. The schematic of material wall transport and possible collision processes is shown in Fig. 4.3.

---

[1]Collision processes should satisfy $\Delta x/\lambda_{mfp} \ll 1$ and $\Delta t_{coll}\nu_{coll} \ll 1$, where λ_{mfp} and ν_{coll} are average mean free path and average collision frequency, respectively [116].
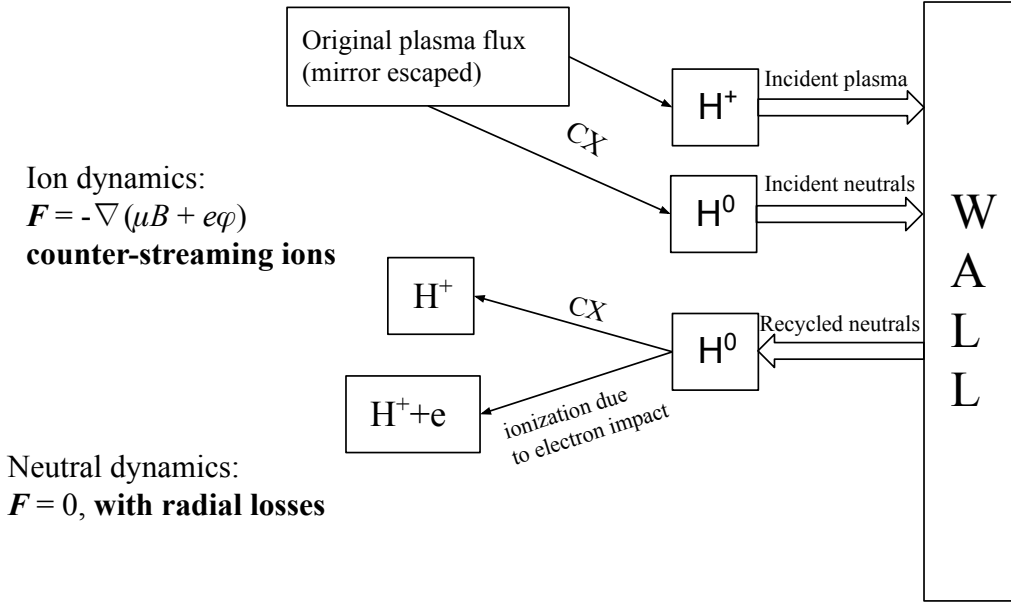
Figure 4.3: General schematic of atom transport with possible collision processes.

4.2.1 Ion dynamics

Ions are modeled in the drift-kinetic approximation. It implies the averaging over the ion gyrofrequency (neglecting slower time dynamics), and considering spatial scales larger than the ion gyroradius. With the magnetic moment conservation, ion gyrocenters experience the electric field force and the mirror force:

$$m_i \frac{dv_z}{dt} = eE_z - \mu \frac{\partial B}{\partial z}, \tag{4.1}$$

where the magnetic moment $\mu = m_i v_\perp^2 / 2B = \text{const}$. The ion distribution function f_i follows

$$\frac{\partial f_i}{\partial t} + v_z \frac{\partial f_i}{\partial z} + \frac{dv_z}{dt} \frac{\partial f_i}{\partial v_z} = \mathcal{C}_{i,a}\left(f_i, f_a\right), \tag{4.2}$$

where the collision operator $\mathcal{C}_{i,a}$ describes effects due to ionization and CX events, it depends on both ion and atom distribution functions. We omit analytical form for $\mathcal{C}_{i,a}$, it is accounted with the DSMC algorithm.

Source wall

Ions are injected from the left wall (source) with the half-Maxwellian distribution parallel to magnetic field lines and isotropic Maxwellian for its perpendicular component:

$$f_i\left(v_z, v_\perp\right) = \frac{4n_0}{\sqrt{\pi}V_{Tz}V_{T\perp}^2} \exp\left(-\frac{v_z^2}{V_{Tz}^2}\right) v_\perp \exp\left(-\frac{v_\perp^2}{V_{T\perp}^2}\right) \tag{4.3}$$

with $v_z > 0$. While in z-direction we inject only in the half-space, an additional factor of "2" ensures $n_0 = \int f_i \mathrm{d}v_z \mathrm{d}v_\perp$. Here v_{Tz} and $v_{T\perp}$ are parallel and perpendicular thermal velocities, respectively, defined as $v_T = \sqrt{2T/m}$ (m is the ion mass), where the corresponding temperatures defined as

$$T_z = 2\int mv_z'^2 f \mathrm{d}v_z \mathrm{d}v_\perp, \tag{4.4}$$

$$T_\perp = \frac{1}{2}\int mv_\perp^2 f \mathrm{d}v_z \mathrm{d}v_\perp, \tag{4.5}$$

where $v_z' = v_z - V_z$ (V_z is the average flow velocity).

Particles may be reflected back by the magnetic mirror force or the electrostatic potential and reach the source wall. By default, we consider the simple absorption (source) wall. Another option is to return these particles into the system, either with the pure specular reflection (keeping the same magnetic moment and $v_z = -v_z$) or perform the diffuse reflection (sample new velocities). Diffuse reflection imitates the collisional filling of the loss cone in the source. A combination of both reflection regimes on the source wall (specular and diffusive) is also possible.

4.2.2 Electron dynamics

During relatively slow ion bounce motion in the magnetic mirror, electron Coulomb collisions quickly fill the electron loss cone and cause higher electron losses. It allows to consider Maxwellian and isotropic electrons and, in the simplest case, use Boltzmann relation for electrons [16]. Plasma quasineutrality gives rise to the electrostatic potential slowing electron losses but expands the ion loss region in the velocity space (recall Fig. 1.5). Note that the extent of this potential structure is much larger than the Debye length.

The goal is to exploit the simple electron model, starting from the Boltzmann relation, then include the finite electron current due to collisional effects (ionization). Future work is left to include heating and dissipating effects for electrons (heat fluxes, collisional losses).

Current-free Boltzmann electrons

The simplest model is Boltzmann electrons, where the electric field is obtained from the electron momentum:

$$0 = -enE - T_e \nabla_z n, \tag{4.6}$$

and, additionally, the full quasineutrality is assumed, $n = n_e = n_i$. In this approximation the density gradient generates the electric field that enforces equilibrium electron current (no net force). Collisions are neglected in the electron momentum exchange; thus, the electron current is undefined (infinite) in pure Boltzmann approximation.

Electron current and biasing

In the presence of high-density neutral regions (near the wall), electron-neutral (e-n) collisions may not be negligible in the electron momentum balance. For $T_e = 200\,\text{eV}$, the ionization rate is $\beta_{ion} = 2.1 \times 10^{-14}\,\text{m}^3\text{s}^{-1}$ [117], and the estimated collision frequency due to ionization is $\nu_{en} = \beta_{ion} n_a = 2.1 \times 10^6\,\text{s}^{-1}$ (for $n_a = 1 \times 10^{19}\,\text{m}^{-3}$). Finally, the electron mean free path estimated as $\lambda_e \sim v_{Te}/\nu_{en} \approx 3\,\text{m}$. It is comparable to the density inhomogeneity length $L_n \sim 1\,\text{m}$. Adding the electron-neutral collisional friction to Eq. (4.6) results in

$$-en_e E_z - \nabla_z p_e - m_e n_e \nu_{en} v_{ez} = 0, \tag{4.7}$$

where the atom flow velocity is neglected[2]. The electron flux is

$$n_e v_{ez} = \frac{e}{m_e \nu_{en}} n_e \nabla_z \phi - \frac{1}{m_e \nu_{en}} \nabla_z p_e. \tag{4.8}$$

With the full quasineutrality, $n_e = n_i$, combining ion and electron continuity equations, one obtains the divergence-free total current $j_z = e(nv_i - nv_e)$:

$$\nabla_z (j_z/B) = 0, \tag{4.9}$$

---

[2]High atom flow velocity may occur near the magnetic throat but the atom density there is orders lower than near the wall and the collisional friction is negligible.

which can be inverted to evaluate the electrostatic potential. The equation for the potential reads

$$\nabla_z \left(\frac{1}{B} \left[nv_i - \frac{e}{m_e \nu_{en}} n \nabla_z \phi + \frac{1}{m_e \nu_{en}} \nabla_z p_e \right] \right) = 0, \tag{4.10}$$

and can be solved with the fixed boundaries (Dirichlet condition), e.g. $\phi(0) = 0$, $\phi(L) = V$. Another option is to fix the total current at some location, e.g. at the entrance $j_z(0) = j_{z0}$; effectively it specifies the boundary condition for $\nabla_z \phi(0)$ (Neumann condition).

4.2.3 Neutral transport

When light atoms hit a solid wall, they can be scattered from the material surface (after one or multiple collisions) at a large enough angle to be effectively reflected. Another possibility is entrapping inside the wall. In both cases, the energy lost by the incident particle due to interaction with the wall can lead to the sputtering process (ejecting material atoms from the surface). However, the reflection events dominate over sputtering for light ions like Hydrogen (notable sputtering is caused by heavier ions). For example, the maximum particle yield is only about 1% for De^+ (Deuterium ion) and 0.3% for H^+ (Hydrogen ion) for bombardment of the titanium wall [118]. Thus, we will neglect the sputtering in the neutral transport modeling. Besides the reflection, we include desorbed atoms (cold, of wall temperature), and more energetic ones created due to molecular desorption and its further ionization and dissociation, so-called Franck-Condon atoms of $1\,\text{eV} - 4\,\text{eV}$. The latter are included via a parameter without an actual model of the molecular dissociation. Due to the general difficulties for accurate accounting of complex chemistry processes on the wall, the desorption process is modeled empirically and controlled by the sticking coefficient and other parameters (details are given below). We start with the reflection process.

Reflection

The reflection coefficients are available in the literature [114], calculated from both experiments and simulations for a wide range of incident particles and materials. They are mainly available as integral yield coefficients for the fraction of reflected particles R_N and the fraction of reflected energy R_E (relative to the corresponding number and energy of incident
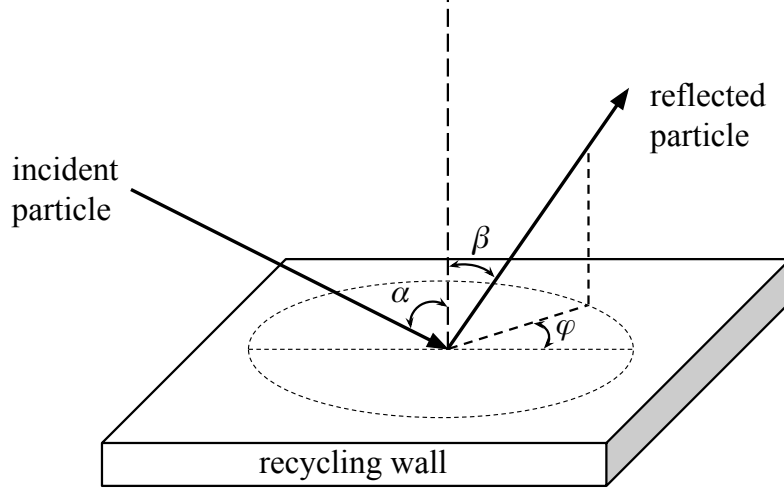
Figure 4.4: Definition of angles for the reflection problem with incident and reflected particle (this figure is drawn similarly as in Ref. [119]).

particles). Higher-dimensional information, such as the distribution function of the reflected population (depends on the incident energy and incident angle), is only available for a limited number of studies (and in the reduced form, as will be shown later), caused by a lack of such data. While it is easier to collect it from a computer simulation, these simulations have to be verified with the corresponding experimental data, which is costly and slow.

The following notation is used (following Ref. [119]) for the reflection problem. The distribution function of reflected particles $f_R(E_0, \alpha; E, \beta, \phi)$ is a function of energy E, the reflected polar angle β and the reflected azimuthal angle ϕ; it depends on the incident energy E_0 and the incident polar angle α, see Fig. 4.4 (both α, β are measured with respect to the surface normal).

Definitions of the number reflection coefficient R_N and the energy reflection coefficient R_E:

$$R_N = \frac{1}{N_0} \int f_R(E_0, \alpha; E, \beta, \phi) dE \sin \beta d\beta d\phi, \tag{4.11}$$

$$R_E = \frac{1}{E_0 N_0} \int f_R(E_0, \alpha; E, \beta, \phi) E dE \sin \beta d\beta d\phi, \tag{4.12}$$

where N_0 and E_0 are the incident number of particles and their energy. It is seen that

$$R_N/R_E = E_0/\bar{E}_R, \tag{4.13}$$

where $\bar{E}_R$ is the average energy of the reflected particles. As expected, the relation between R_N and R_E only contains information on average reflected energy. One can use R_N and R_E to model atoms with discrete energy levels $\bar{E}_R$. Coefficients R_N, R_E are still functions of (E_0, α), but typically evaluated at normal incidence angle $\alpha = 0°$, only as functions of the incident energy, which is useful for many applications. In our setup, the perpendicular pressure of incident particles is low (in the end of expander region), and the normal incidence is acceptable. The semi-empirical formula was proposed for both R_N, R_E which can be used for a wide range of materials [114]:

$$R_N \text{ (or } R_E) = \frac{A_1 \ln A_2 \epsilon + e}{1 + A_3 \epsilon^{A_4} + A_5 \epsilon^{A_6}}, \tag{4.14}$$

where $A_1 - A_6$ are the fitting parameters (they differ for R_N and R_E), e is the base of natural logarithms, and ϵ is the Tomas-Fermi reduced energy (sometimes Firsov screening length is used, giving 10% smaller ϵ [119]). The reduced energy ϵ is the function of the incident particle energy E_0, its mass ratio with target material nuclei μ, and electric charges of both the incident particle and the target nuclei (its atomic number) [114]. Coefficients $A_1 - A_6$ depend on the value of the mass ratio μ [114]. The reflection coefficients given by Eq. (4.14) are shown in Figs. 4.5a and 4.5b, for the Hydrogen ion and various wall materials. A small difference is seen between the results for Ti and Fe as a material wall occurs due to their close atomic numbers.

Even though we assume the normal incidence, it is worth noting that the scaling $\epsilon \cos^2 \alpha$ can be used to include the dependence on the incident angle [119], simply by the substitution $\epsilon \rightarrow \epsilon \cos^2 \alpha$ in Eq. (4.14). For example, a high yield, up to 100% can be expected for the grazing angles ($\alpha \approx 90°$), as they mainly interact with the surface atoms, and almost any scattering event will lead to reflection.

A potential problem with utilizing only the R_E coefficient and thus ignoring the shape of the distribution function for the reflected particles rises due to ignoring possible lower energy particles in the distribution function. Slow atoms tend to accumulate near the wall and potentially have a stronger effect on the accelerated plasma flow (as shown in the results). The simplest extension to R_E coefficient (adding one degree of freedom) would be the energy distribution function $F_E(E)$ of the reflected particles (still integrated over polar and azimuthal
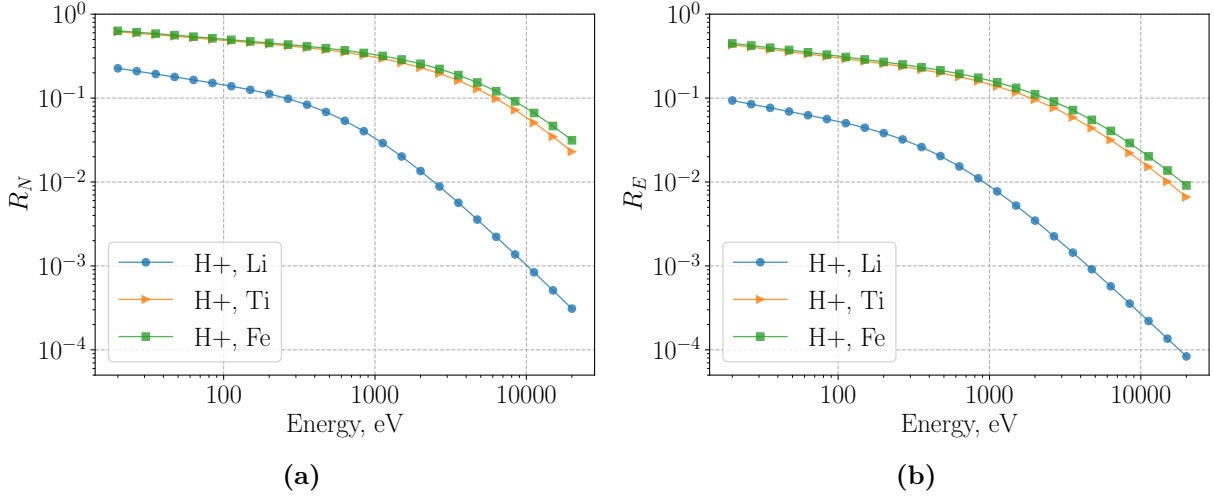
Figure 4.5: Total (integral) reflection coefficients R_N (a) and R_E (b) as a function of normal incident energy (in eV) for Hydrogen ion bombarding material wall (Li, Ti, or Fe), obtained from Eq. (4.14) with appropriate coefficients taken from Ref. [114].

angles), defined as

$$F_E(E) = \int f_R(E_0, \alpha; E, \beta, \phi) dE \sin \beta d\beta d\phi, \tag{4.15}$$

where F_E depends on the incident energy E_0 and the incident angle α. The empirical relation for F_E is proposed in Ref. [120]:

$$F_E = A \left[\left(C + D(E/E_0)^2 \right) \left(B - E/E_0 \right) + \exp \left(-(E/E_0 - B)^2 / 2\sigma^2 \right) \right], \tag{4.16}$$

where B, C, D, σ are the fitting parameters, available for the following pairs: (H^+, Cu), (He^+, Cu), (He^+, Ni), for the incident energies $1\,\mathrm{keV}$, $5\,\mathrm{keV}$, and the incident angles of $(0, 40, 60, 70, 80)°$ [120]. The coefficient A in Eq. (4.16) is found via

$$\int_0^{E_0} F_E dE = N_0 R_N, \tag{4.17}$$

where N_0 is the number of incident particles, and R_N can be evaluated from Eq. (4.14). The example distributions F_E produced for the three different incident energies are depicted in Fig. 4.6, for the (H^+, Cu), normal incidence, and $1\,\mathrm{keV}$ incident energy. Here R_N coefficients were chosen according to the Eq. (4.16) for Hydrogen ions bombarding titanium wall, with the non-positive function values capped to zero. The total distribution is simply the sum of three, which can be used for further sampling of reflected particles. We use this model for the
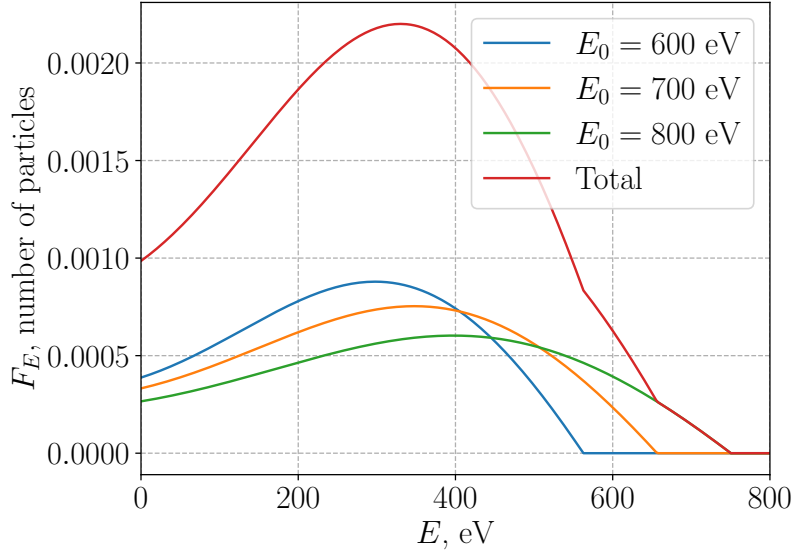
Figure 4.6: Examples of the reflected energy distribution function F_E for neutrals according to model in Ref. [120], for three incident particles with energies $600, 700, 800$ eV, where coefficients in Eq. (4.16) are for (H^+, Cu) (Hydrogen ions bombards Cu wall); incident particle number $N_0 = 1$.

energy distribution of the reflected atoms in the following way. On each time step, a number of incident macroparticles bombarding the wall effectively define the total distribution by adding all individual F_E, given by Eq. (4.16). Then it is used to sample atom energies (details on parallel and perpendicular velocities are following) with the numerical cumulative distribution function method. Even though we are interested in the normal incidence, it is worth noting that for the grazing angles, the shape of the distribution function F_E peaks near the incident energy (for the same reasons discussed above for the incident angle distribution) [120].

The polar angle β essentially defines the ratio of parallel and perpendicular energy of the reflected crowd. In our hybrid drift-kinetic model, the azimuthal angle ϕ is not resolved (included in the perpendicular velocity). Hence, we are interested only in β and assume the isotropic distribution for the azimuthal angle ϕ. Both experiments and simulations suggest that the cosine distribution is a good approximation for the reduced energies below $\epsilon \approx 10$, according to Ref. [119]. For example, for the pair (H^+, Ti) this range translates to incident energies below $20\,\text{keV}$ which suffice our needs. Thus, we proceed by sampling the energy from the distribution F_E using Eq. (4.16) and then sampling the angle β for every particle

from the cosine distribution.

Finally, as one could expect, there is evidence that not all of the reflected particles are in the neutral state, as shown in Ref. [119] based on the experiment with Hydrogen bombarding the stainless steel. Less than 15% of reflected particles are charged for the incident energies below $10\,\text{keV}$ (the fraction increases for higher energies), and less than for $1\,\text{keV}$. It suggests that a parameter can be introduced to control the charge state of reflected particles.

Note that some ions from the original flow neutralize due to CX with slow atoms (especially near the wall) and bombard the wall. These fast neutrals accounted in the same path as ions, and thus, contributes to the overall reflection rate [119].

Desorption, sticking coefficient

Additionally to relatively high-energy reflected particles, low-energy atoms "peels off" the wall due to desorption. Due to their low velocity, these atoms can quickly accumulate in the near-wall region and significantly affect plasma acceleration. Compared to the reflection model described above, the desorption process will be modeled with a more qualitative, empirical approach. Desorbed atoms are split into two components: wall-temperature (cold) atoms and Franck-Condon (FC) atoms (with energies $1\,\text{eV} - 4\,\text{eV}$, close to dissociation energy). The idea is that during the particles-wall bombardment, in the equilibrium, the following processes can occur:

$$1 = P_r + P_d + P_a, \tag{4.18}$$

where P_r is the reflection ratio (same as R_N coefficient, given previously), P_d is the total desorption ratio, and P_a is the adsorption ratio (also called sticking coefficient). We assign the constant isotropic temperatures for the low-energy (cold) and the FC atoms, $T_{a,c}$ and $T_{a,FC}$, respectively. The desorbed output further split with the coefficient P_{FC} (0–1), defining the probability of injecting a Franck-Condon atom[3]. For the total number of recycled particles (reflected and desorbed), Eq. (4.18), the parameter $\mathcal{R} = P_d + R_N$ is introduced similarly to the DEGAS neutral model [121]; it effectively replaces P_a coefficient ($P_a = 1 - \mathcal{R}$). Note, that according to this model, the number of desorbed atoms depends on R_N ($P_d = \mathcal{R} - R_N$),

---

[3]Using rejection method: a random number $0 \leq r \leq 1$ is sampled: if $r \leq P_{FC}$, then atom with the temperature $T_{a,FC}$ sampled, otherwise with $T_{a,c}$.

L_z (m)	Γ_0 (m^{-2}s^{-1})	T_e (eV)	T_i (eV)	$\mathcal{R}$	P_{FC}	$T_{a,c}$ (eV)	$T_{a,FC}$ (eV)
3.0	3×10^{23}	200	50	0.95	0.5	0.1	2.0

Table 4.1: Simulation parameters for the radial loss effects.

which evaluates consistently with incoming bombarding particle flux. If R_N becomes smaller (e.g., due to increased incident energy, Fig. 4.5a), the number of desorbed atoms increases.

Radial losses

Atoms from all sources described above can escape the simulation volume in the radial direction (which is not resolved, but the particle's perpendicular velocity allows to estimate its radial dynamics). We add this effect by assigning the virtual radial coordinate to every atom with the initial value $r = 0$ m. Whenever a particle crosses the radial length L_r, it is removed. First and foremost, the radial losses cause the significant drop of atom density stepping from the wall. It can be seen in the simulations without collisions, only in the presence of accelerated plasma flow and atoms caused by it in the equilibrium. Parameters of the simulations are given in Tab. 4.1, with the various radial loss coefficients $L_r = (1, 5, 10, 25)$ cm. The resulting atom densities are shown in Fig. 4.7, where the second half of the channel is shown (region from the mirror throat to the wall). Obviously, the losses significantly increase when the $L_r \ll L_z$ (for isotropic atom population). Note that R_N coefficient for the reflected yield, Eq. (4.14), is evaluated for Hydrogen ions bombarding the titanium wall.

More detailed effects of the radial losses on the specific atom populations is shown for the case with $L_r = 10$ cm (this value is used for all future simulations with collisions), on figures with the atom distribution function f_a in a few two-dimensional slices of its phase space (which in general is four-dimensional, $f_a = f_a(z, r, v_z, v_\perp)$). Fig. 4.8a shows the distribution of atoms in (r, z)-space. In Fig. 4.8b its shape in the space $(v_\perp, z)$ reveals the "chopping" effect of the finite length L_r, i.e. only particles with the smallest perpendicular energy can reach the left boundary. In Fig. 4.9a, $f_a(z, v_z)$ shows that the cold atom component is able to reach deeper into the channel. Finally, Fig. 4.9b shows $f_a(v_z, v_\perp)$ in the right-most cell near the wall ($z = L$), where the radial losses did not contribute yet.
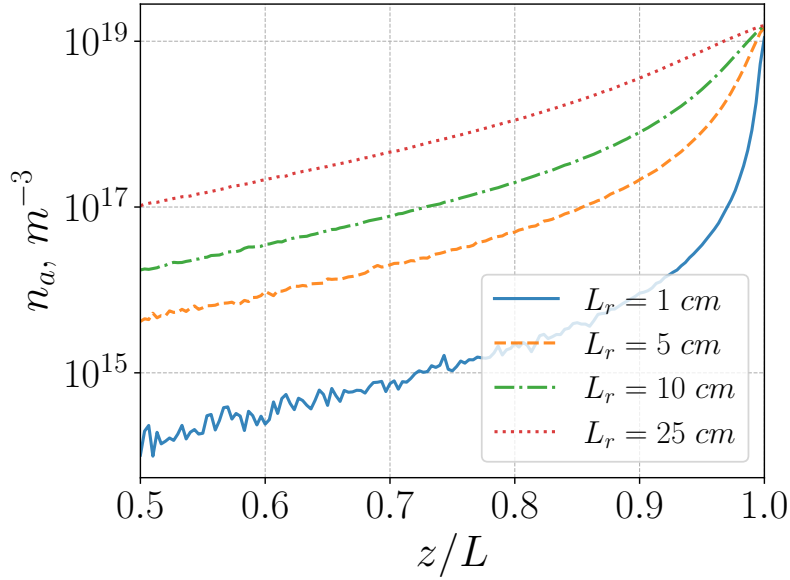
Figure 4.7: Atom density profiles for the various radial loss coefficients L_r (radial "wall"), demonstrating pure radial loss effect (without collisions).

(a)

(b)
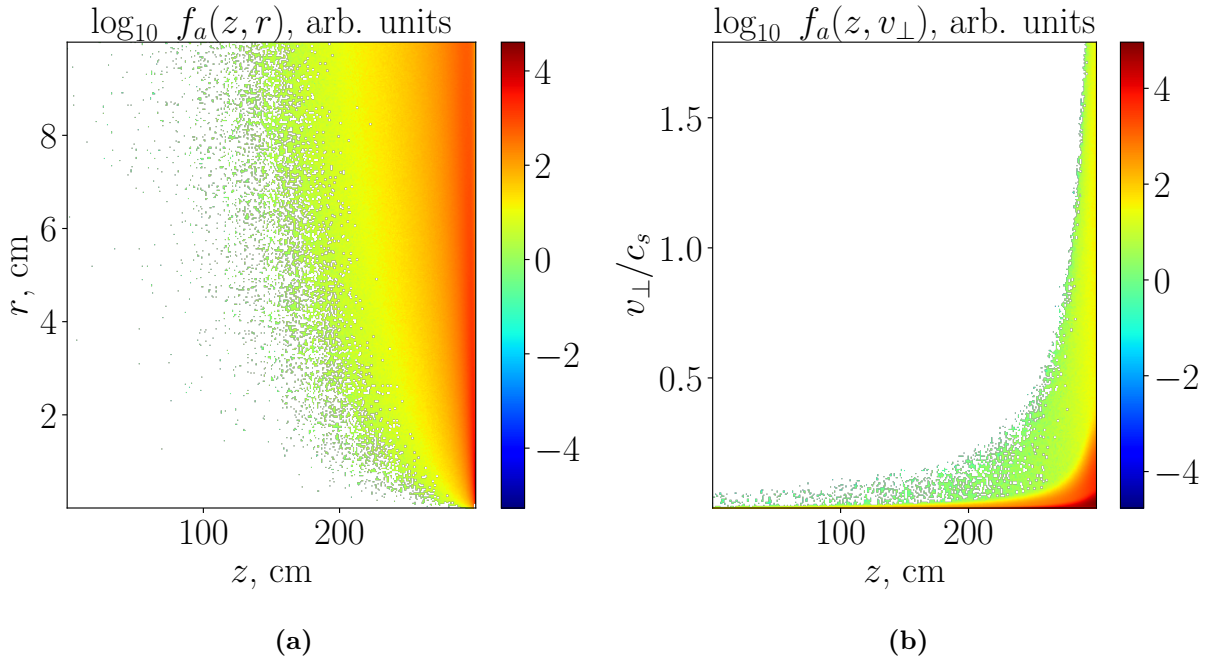
Figure 4.8: Effect of radial atom losses with $L_r = 10$ cm shown in (z, r)-space (a) and $(z, v_\perp)$-space (b). Note that atom distribution function (arb. units) shown in logarithmic scale. Atoms with higher perpendicular velocities (mostly those from reflected population) leave the system faster (exactly in $L_r/v_\perp$ seconds) and thus slow atom component penetrates deeper into the channel (b).

(a)   **(b)**
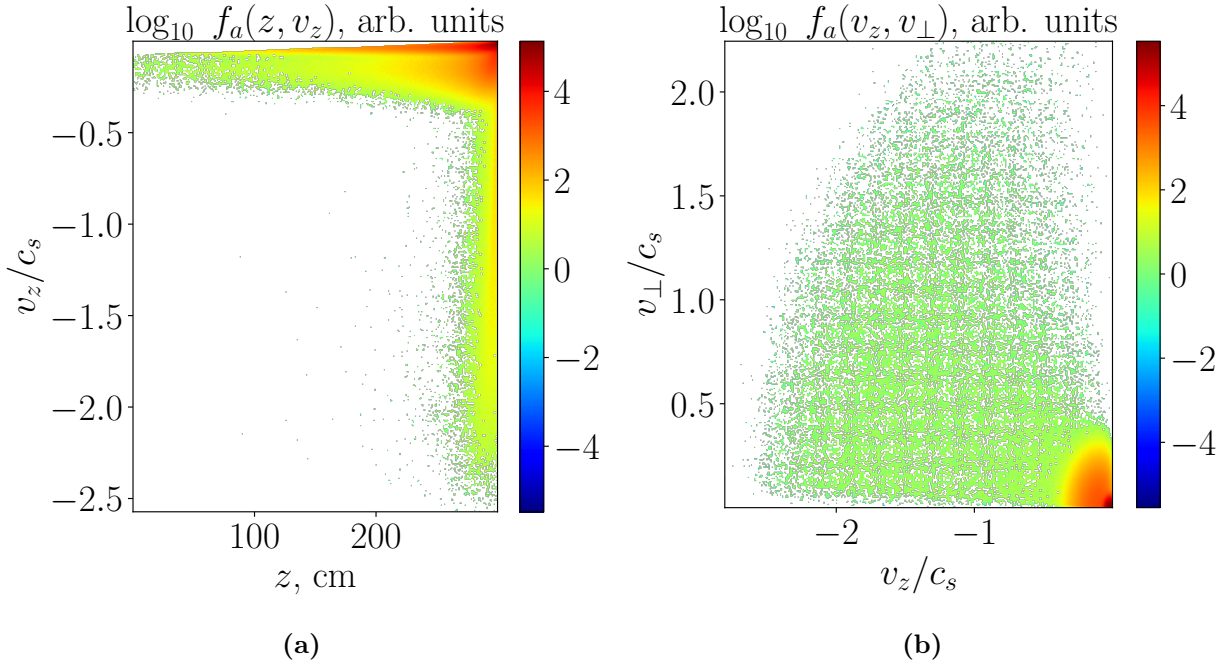
Figure 4.9: Effect of radial atom losses with $L_r = 10\,\mathrm{cm}$ shown in (z, v_z)-space (a) and $(z, v_\perp)$-space (b) at the end wall, $z = L$.
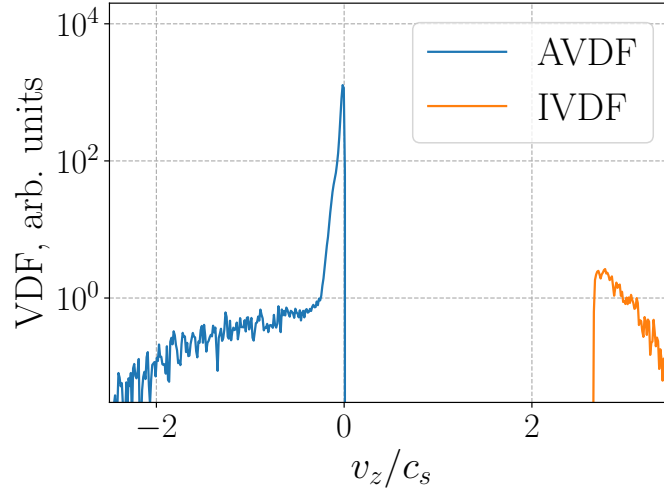
Figure 4.10: Velocity distribution functions for ions and atoms at the wall ($z = L$). Reflection (due to ion backscattering) leads to the higher-energy tail of distribution function, while atoms due to desorption tend to accumulate, contributing to high atom density.
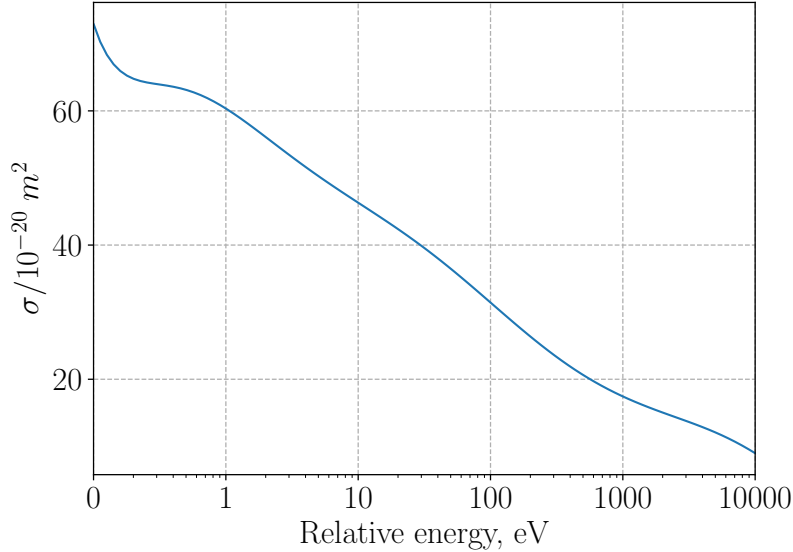
Figure 4.11: Charge-exchange cross-section for collision $(\mathrm{H}^+, \mathrm{H}) \to (\mathrm{H}, \mathrm{H}^+)$ (both neutrals are in ground state), reaction 3.1.8 in Ref. [117].

4.2.4 Collisions

In the presence of the atom conglomerate described above, collisions between plasma species and neutrals will occur (especially near the wall). Most probable events include charge exchange (CX) due to ion-neutral and ionization due to electron-neutral collisions. Direct simulation Monte Carlo (DSMC) algorithm is implemented for handling collisions with the null collision method [116]. Since ions and neutrals are both kinetic, CX collisions will be processed consistently with their distribution functions. For ionization, since electrons assumed isotropic, $T_e = \mathrm{const}$, the constant value of the ionization rate is used, $\beta = \langle \sigma v \rangle = 3.1 \times 10^{-13}\,\mathrm{m^3 s^{-1}}$ (averaged over Maxwellian distribution for $T_e = 200\,\mathrm{eV}$) [117]. CX cross-sections for ion-neutral collisions, $(\mathrm{H}^+, \mathrm{H}) \to (\mathrm{H}, \mathrm{H}^+)$ taken from Ref. [117], reaction 3.1.8, shown in Fig. 4.11.

Besides the statistical error present in DSMC (minimized by the increased number of particles), there are spatial and time constraints that can lead to notable errors if violated [116]. They are associated with the average mean free path λ and collision frequency ν. $\Delta x_{coll} \ll \lambda$ and $\Delta t_{coll} \ll 1/\nu$ constraints. As it will be shown in the results, the smallest values for λ well exceed the cell size (the smallest Knudsen numbers are ~ 0.1). We further

assume that collisional cells coincide with PIC cells $\Delta x_{coll} = \Delta x$ (and call them just cells)[4]. Also, the sub-cycling (integer) parameter $N_{sub,c}$ is introduced for collisional time step, relating it to the simulation time step as $\Delta t_{coll} = N_{sub,c}\Delta t$.

Since collisions are calculated in every collisional cell, some particle tracking tool is required for efficient operation on particles corresponding to given cells. For this purpose, the following particle tracking structure was implemented (generally, PIC structures that store information about particles, such as coordinates and velocities, do not perform any sorting in space, and it would be highly inefficient to use them for locating particles). The idea is to use a two-dimensional structure that will store global particle indices for corresponding cells (where a particle is currently located). Additionally, it stores the number of particles in the corresponding cell. Then, during the DSMC process, it would be easy to access and sample some number of particles (in a given cell) to check for a possible collision event. The presence of large-scale difference in plasma density profile (and constant particle weight, like in our approach) will make very wasteful use of memory if one uses a two-dimensional array. In the magnetic mirror configuration, a large portion of particles are confined before the magnetic throat, and near the wall, we may have particle density orders smaller than in the source. Effectively, we implemented a two-dimensional array with the variable-size second dimension; see the schematic in Fig. 4.12.

Finally, we briefly describe the DSMC algorithm with the null collision method. We denote n_t - the density of target particles (neutrals), and N_i is the number of incident particles. The null collision method allows to avoid going through every possible pair of colliding particles, evaluating individual probabilities and testing for a collision (e.g., by rejection method), which is very costly. Instead, the maximum collision frequency ν_{max} is estimated over whole range of the parameter space (coordinate x and the relative velocity v_r) [116]

$$\nu_{max} = \max_{x,v_r} n_t \sigma(v_r) v_r = \max_x (n_t) \max_{v_r} (\sigma(v_r) v_r) \qquad (4.19)$$

where σ is the cross-section and depends on v_r. Then the maximum fraction of collisions

---

[4]In higher dimensional, more demanding simulations, one could benefit from implementing a separate collisional grid, possibly non-uniform and/or adaptive to local values of λ.

taking place during Δt_{coll} is [116]

$$P_{max} = 1 - \exp{(-\nu_{max}\Delta t_{\text{coll}})}, \tag{4.20}$$

which includes real collisions and null collisions. With known P_{max} one can simply sample this fraction of particles and test for a collision type (among which is the null collision event, i.e. collision does not occur). Instead of choosing the maximum collision frequency over all space, Eq. (4.19), here it is assumed spatially dependent

$$\nu_{max}(x) = n_t(x) \max_{v_r}{(\sigma(v_r)v_r)}, \tag{4.21}$$

varied with the local target density n_t. The value of $\max_{v_r}(\sigma(v_r)v_r)$ gets updated every time the larger value is observed. If there are few collision types, the total maximum collision frequency is simply

$$\nu_{\text{tot}} = \sum_i (\sigma v_r)_{max,i}, \tag{4.22}$$

where $(\sigma v)_{max,i}$ is the estimate of maximum collision rate for i-th reaction. It is then substituted to Eq. (4.20) to evaluate number of particle to sample. The number of possible collisions N_c in a given cell is

$$N_c = \lceil PN_p \rceil, \tag{4.23}$$

which is rounded to integer (ceiling operation); to compensate the rounding error, the correction (increase in this case) of the total collision frequency ν_{tot} is applied [35]:

$$\nu'_{\text{tot}} = \frac{N_c}{N_p \Delta t_{\text{coll}}}, \tag{4.24}$$

where N_p is the number of incident particles. After that we select randomly N_c colliding pairs and calculate $(\sigma(v_r)v_r)_j$ for j^{th} collision type and evaluate the collision probability as $p_j = (\sigma(v_r)v_r)_j / (\sigma(v_r)v_r)'_{\text{max},j}$ (prime indicates corrected value). With all probabilities known, the rejection method is applied to decide on a type of occurred collision. We ensure that if a neutral particle is ionized, it could not be used for the CX in the same collision time step. At the same time, no such restriction posed on the repeated CX or ionization followed by CX.
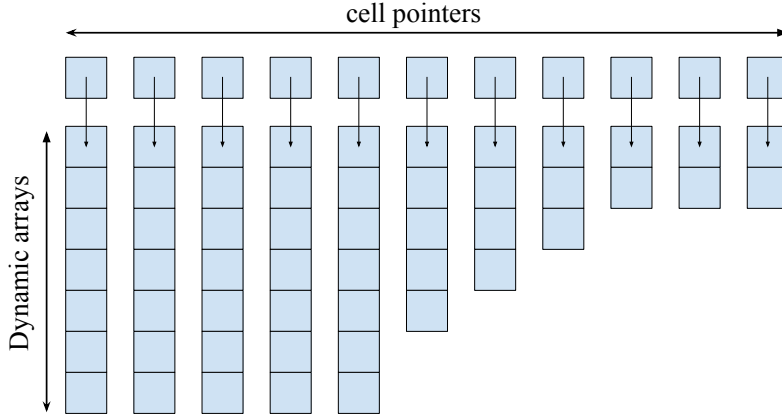
Figure 4.12: Schematic representation of data structure used for particle tracking required for DSMC. The array of pointers of cells number size is allocated first. Then, a dynamic array is allocated for each pointer, storing global particle indices (integers) corresponding to this cell. The array size is controlled with the standard table-doubling algorithm; thus, it adjusts to the local number density profile.

4.3 Results

Since the atom model has many empirical parameters, here we focus on establishing the main effects and discuss its mechanisms. Hydrogen (with atomic mass 1.008) is assumed for ion and neutral species. In all the following simulations, the magnetic field intensity is given by

$$B = a + b \exp\left(-\frac{(z - z_0)^2}{\delta_B^2 L^2}\right), \tag{4.25}$$

where $a = 0.1\,\mathrm{T}$, $b = 0.6\,\mathrm{T}$, $z_0 = L_z/2$, $\delta_B = 0.15$, hence the mirror ratio $R = 7$. The profile of the magnetic field is shown in Fig. 4.13.

First, plasma acceleration without atoms (and collisions) is shown to demonstrate the skeleton of this model. The chosen parameters are following: system length $3\,\mathrm{m}$, constant electron temperature $T_e = 200\,\mathrm{eV}$, injected (half-Maxwellian) ion temperature $T_i = 100\,\mathrm{eV}$, injected flux $\Gamma_0 = 1 \times 10^{23}\,\mathrm{m}^{-2}\mathrm{s}^{-1}$. The result is the stationary quasineutral plasma flow with a fraction of injected ions reflected due to the mirror force, with established quasineutral potential structure. Ion (plasma) density shown in Fig. 4.14a is normalized to the injected density

$$n_0 = \Gamma_0/v_0, \tag{4.26}$$
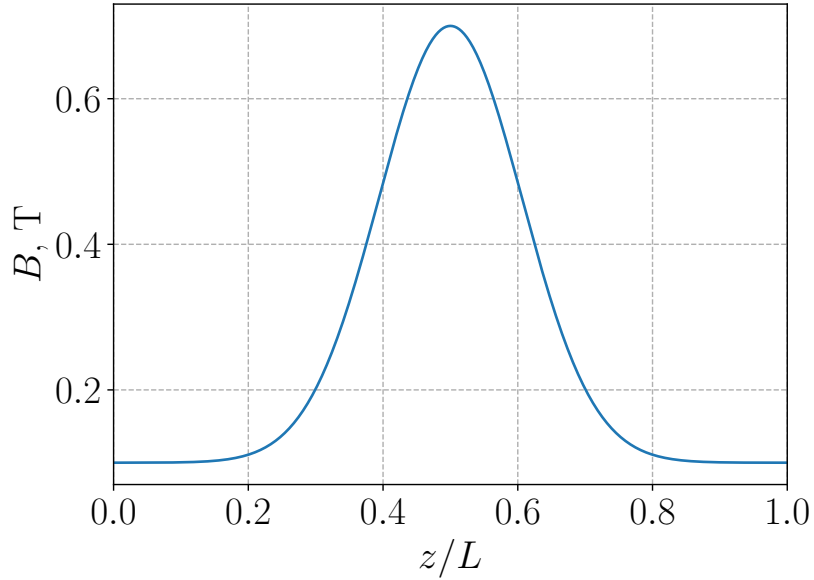
Figure 4.13: Converging-diverging magnetic field profile with the magnetic throat at the center, with mirror ratio $R = 7$, given by Eq. (4.25).

where $v_0 = v_{Ti}/\sqrt{\pi}$ is the average flow velocity for the half-Maxwellian distribution, Eq. (4.3). Its value on the left boundary in the range 1–2 indicates the fraction of reflected ions. The established total electrostatic potential drop is about 3.7 electron temperatures (i.e. $e\Delta\phi/T_e$) which is $\sim$700 V, Fig. 4.14b. The electrostatic potential here establishes according to the Boltzmann electron model, Eq. (4.6), resembling the density shape. As will be shown in the simulations with neutral transport, plasma density will increase in the expander region (mainly close to the wall) as the new sources are effectively introduced via ionization and CX. This will lead to the overall drop in the potential, which may be interpreted as poor electron confinement in the source region.

Below we present the base case with collisions, defining the main sources of particles (both ions and neutrals) near the wall and their main effects. After that, we demonstrate how various parameters affect the overall solution, such as core ion temperature, the fraction of desorbed atoms (cold vs. Franck-Condon), and the sheath effect.
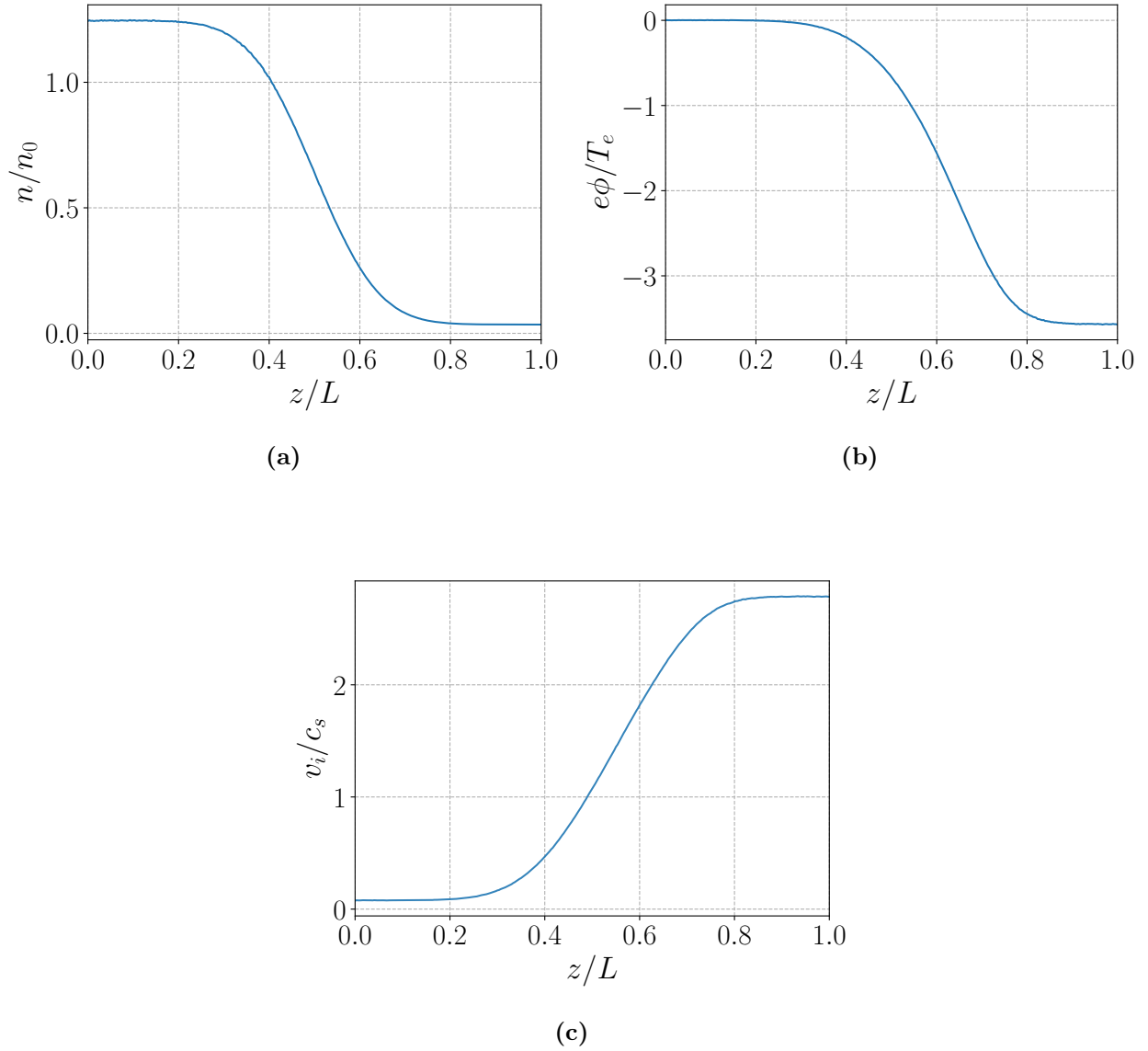
Figure 4.14: Spatial profiles of plasma density (a), electrostatic distribution (b), and ion velocity (c) in whole domain for the case without atoms, pure plasma acceleration. Note the transition through ion-sound velocity at around the maximum of magnetic field (at the center); it is not precise ($v_i/c_s = 1$) due to our definition of $c_s^2 \equiv T_e/m_i$, neglecting ion temperature.

L_z (m)	Γ_0 (m^{-2}s^{-1})	T_e (eV)	T_i (eV)	$\mathcal{R}$	P_{FC}	$T_{a,c}$ (eV)	$T_{a,FC}$ (eV)
3.0	3×10^{23}	200	100	0.95	0.5	0.1	1.0

Table 4.2: Simulation parameters for the base case with collisions.

4.3.1 Base case with collisions

Here, in addition to the full atom transport model (with radial losses), we include collisions due to the CX and the ionization process, simulated with the DSMC algorithm. As noted before, for isotropic electron temperature $T_e = \text{const} = 200\,\text{eV}$, the fixed ionization rate is used, $\beta = 3.1 \times 10^{-13}\,\text{m}^3\text{s}^{-1}$ [117]. CX cross-sections for ion-neutral collisions, taken from Ref. [117], reaction 3.1.8. The full list of parameters for this case is given in Tab. 4.2. This case will be refereed as Base case in further experiments.

The main macroscopic quantities for this case presented in Figs. 4.15a-4.15c. Electrostatic potential drops $\Delta\phi$ decrease about two times (compared with the case with no atoms) due to additional plasma sources (density) near the wall created by interaction with atoms.

The mean free path for atoms is smaller than that for ions, due to the low average velocity of atoms, and higher collision frequency (colliding with ions (CX) and electrons (ionization)). We define the mean free path for atoms as

$$\lambda_a = \frac{v_a}{n\left(\langle\sigma v\rangle_{CX} + \langle\sigma v\rangle_{ion}\right)} \tag{4.27}$$

where v_a is the atom flow velocity, $\langle\sigma v\rangle$ denotes the average collision frequency in a cell (CX or ionization). In practice, collision rates can be obtained as $\langle\sigma v\rangle = S/n_a n_i$, where S [m^{3}s^{-1}] is the source term, n is the plasma number density, n_a is the atom density.
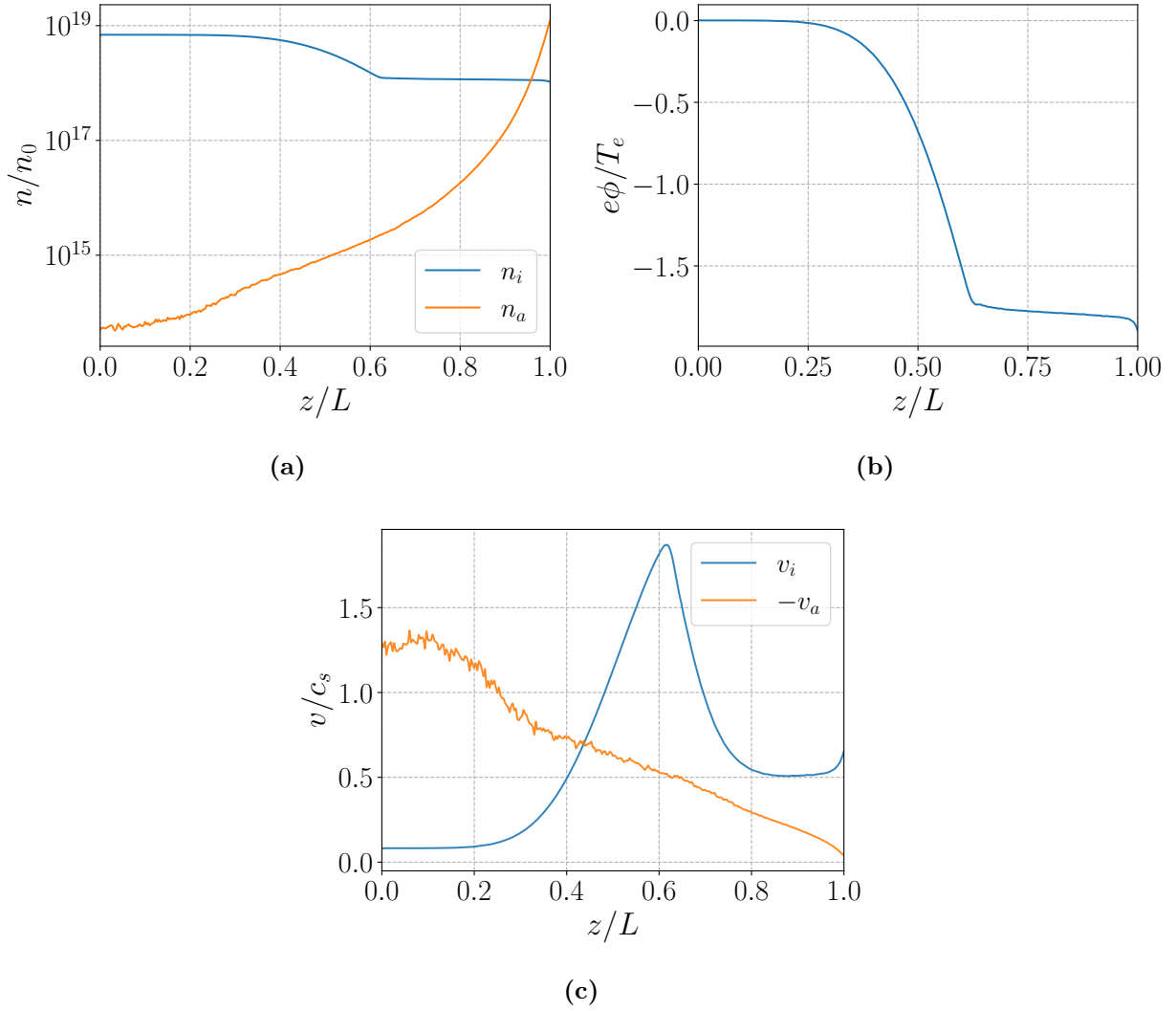
Figure 4.15: Spatial profiles of plasma and atom density (a), electrostatic potential (b), and flow velocities of ions and atoms (c). Note that on average fast atoms were able to penetrate and reach the source and left wall, contrary to the test run without collisions, where we saw many slow atoms reach the source (who were lost here due to shorter mean free path).

The mean free path for ions is similar:

$$\lambda_i = \frac{v_i}{n_a \langle \sigma v \rangle_{CX}}, \tag{4.28}$$

with the ion flow velocity v_i and atom number density n_a. Both λ_a, λ_i are depicted in Fig. 4.16a in the near-wall region. As expected, λ_a is smaller, but both species near the wall

are in the transition flow regime (Knudsen numbers between 0.1 and 10). The collision rate for CX collisions is about $4 \times 10^{-14}\,\mathrm{m^3/s}$, two times of that for ionization, Fig. 4.16b.
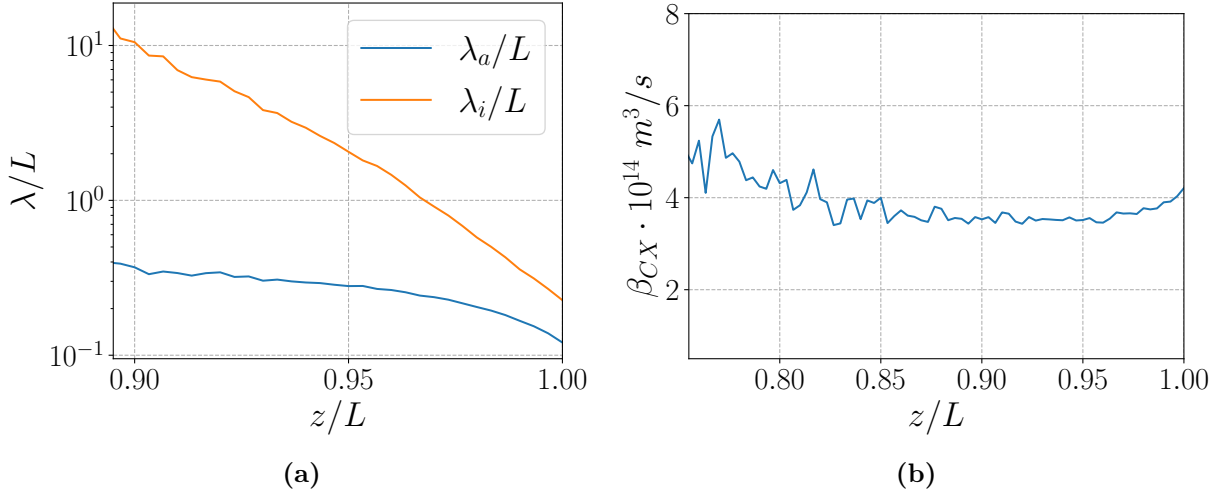
Figure 4.16: Knudsen number parameter for atoms and ions (a) and collision rate due to charge exchange (b). Note, that ionization collision rate is fixed to $\beta_i = 2.1 \times 10^{-14}\,\mathrm{m^3/s}$ due to isothermal electrons.

As we saw previously, the near-wall processes lead to a non-trivial atom source with atoms in a wide energy range (depicted in Figs. 4.8a-4.9b). The main components are relatively energetic reflected atoms, slower Franck-Condon atoms, and cold atoms of wall temperature. Due to a shorter mean free path, cold atoms accumulate, responsible for high atom density near the wall. With collisions, this picture becomes more complex, as seen in the plot of the atom velocity distribution function (AVDF) in Fig. 4.17b. CX collisions create one more atom component, fast atoms (of fast ion velocity) hitting the wall. As for ions, besides being accelerated through the mirror ion flux, high-density slow ion sources appear due to CX and ionization; see Fig. 4.17a for the ion velocity distribution function (IVDF). The slice of the IVDF and the AVDF in the close vicinity to the wall ($0.95L$) is shown in Fig. 4.18. The slow ion beam is effectively trapped (for one ion bounce motion) in this region as it reflects by the magnetic mirror force and the electric field.
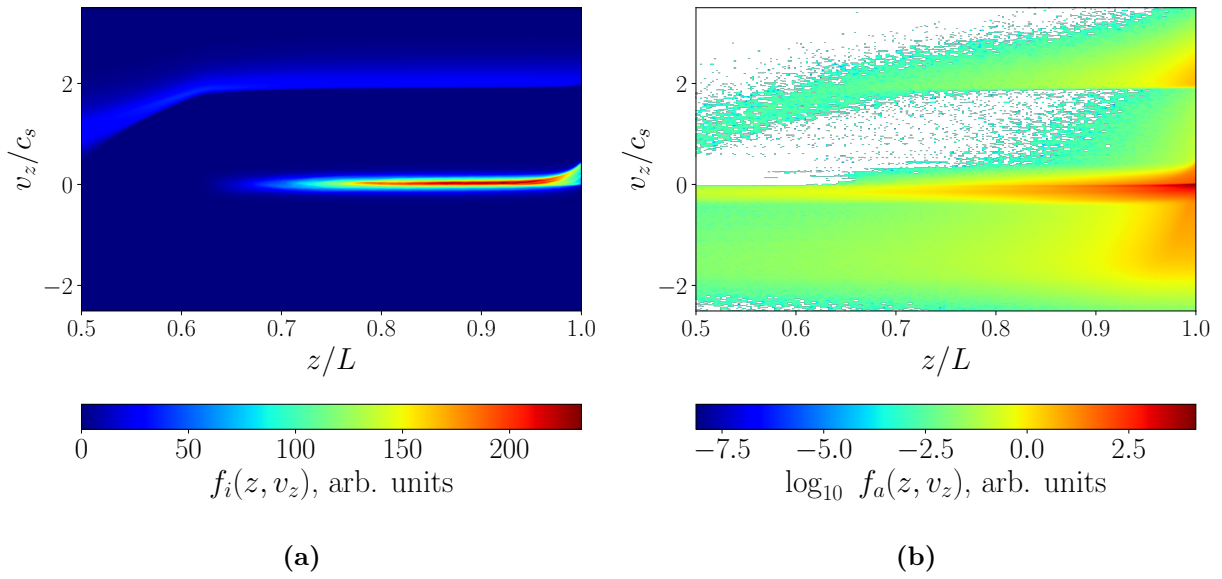
Figure 4.17: Instantaneous plots of velocity distribution functions for ions (a) and atoms (b) in (z, v_z)-space.
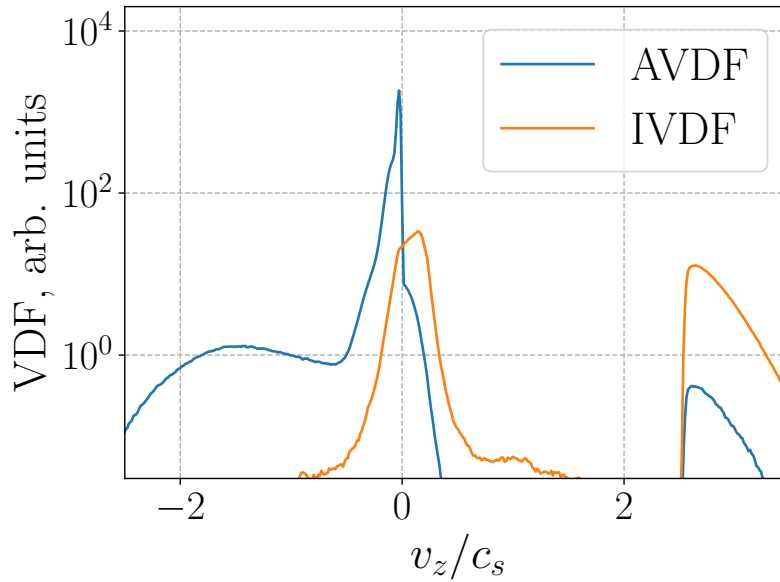
Figure 4.18: Velocity distribution functions for ions and atoms close to the wall (at $z = 0.95L$).

4.3.2 Ion temperature effect
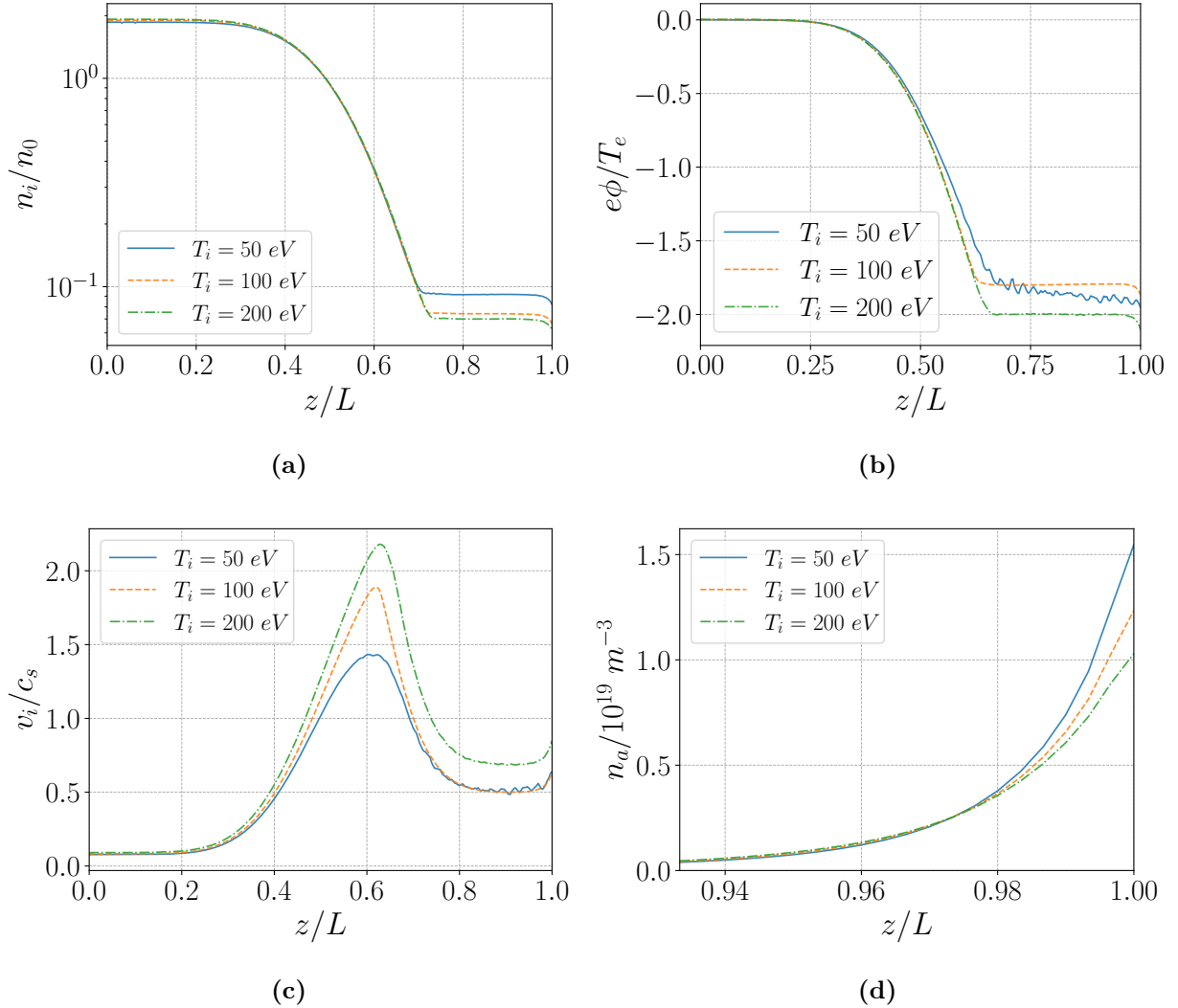
Figure 4.19: Spatial profiles of plasma density (a), electrostatic potential (b), ion velocity (c), and atom density (d). Note that atom density profile is shown in the near-wall region, its value drop significantly into the channel and thus no collision effects become negligible.

Increasing the ion temperature of the source was suggested previously [111] as the way to reduce atom density near the recycling wall, based on the analytical estimates for a stationary model. Here we present results for various injected ion temperatures $T_i = (50, 100, 200)$ eV, keeping other parameters the same as in Base case, Tab. 4.2. It is noted that the increased ion

temperature improves the ion confinement, reducing the ratio of escaped particles reaching the wall. This is mainly responsible for a lower yield near the wall. Figs. 4.19a-4.19d show the resulted profiles for macroscopic variables. The atom density decreases with the increase of ion temperature; this results in a lower plasma density near the wall. As a result, the electrostatic potential drop across the whole domain is also larger for a higher temperature.
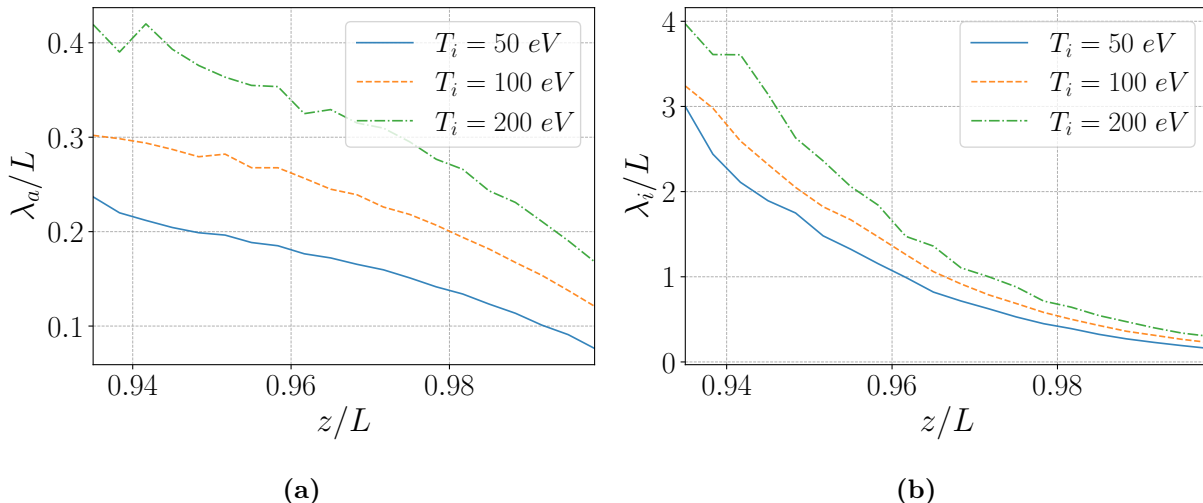
Figure 4.20: Knudsen number for atoms (a) and ions (b) near the wall.

4.3.3 Instability induced by charged-exchange interactions with cold atoms

We demonstrate the cases that result in ion-ion streaming instabilities. The counter-streaming ion configuration is created by the accelerated original ion flow and the cold ion source (due to CX and ionization) near the wall. The density of the cold ion source is proportional to the atom density near the wall, which in turn is higher for the cold atom component, cold desorbed atoms of wall temperature. In this model, it is controlled via the fraction of the Franck-Condon atoms parameter P_{FC}. It is varied as $P_{FC} = (0.2, 0.5, 0.8)$, while all other parameters are kept the same as in Base case. The instability develops for $P_{FC} = 0.2$, with the largest number of the cold atoms, see IVDF and AVDF in Figs. 4.21a-4.21a. IVDF is also plotted in the logarithm scale for better visualization, Fig. 4.22.
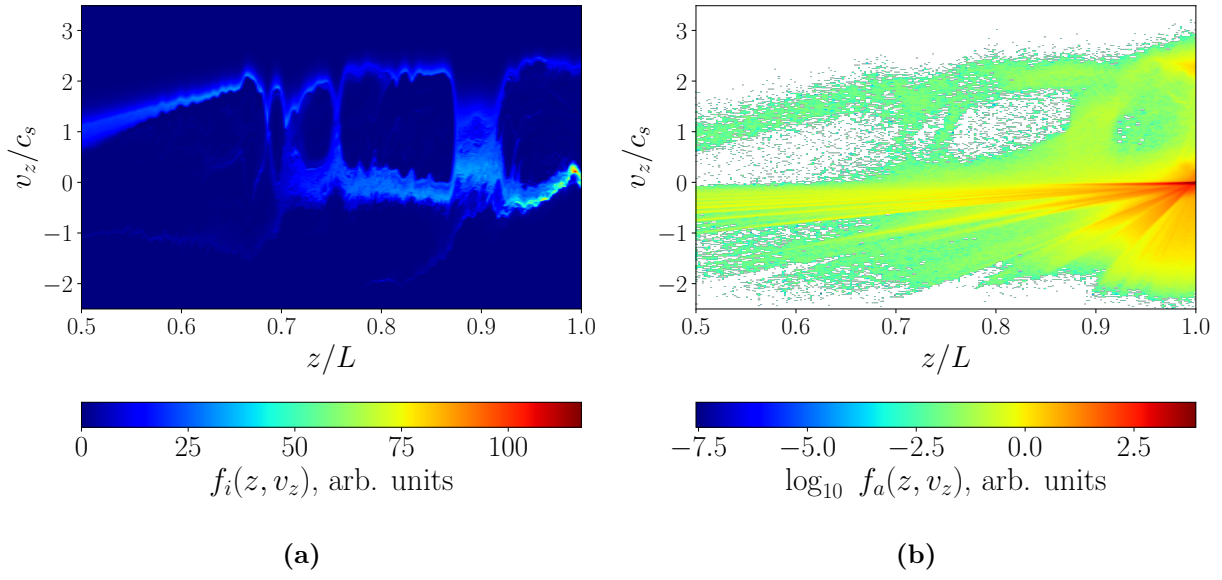
Figure 4.21: Instantaneous plots of velocity distribution functions for ions (a) and atoms (b) in (z, v_z)-space, case for low fraction of Franck-Condon atoms, $P_{FC} = 0.2$.
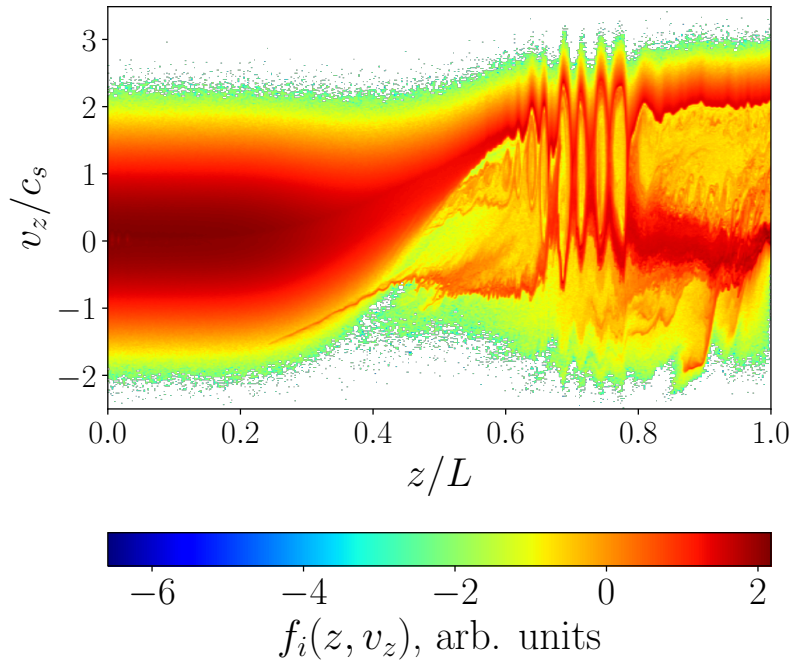
Figure 4.22: Instantaneous plot of velocity distribution function for ions (z, v_z)-space (shown in logarithmic scale), case for low fraction of Franck-Condon atoms, $P_{FC} = 0.2$.

When the cold atom component is reduced with $P_{FC} = 0.8$, the flow is stabilized, see the AVDF and the IVDF plots in Figs. 4.23a and 4.23b. It is worth pointing out that the exact quantity of the cold atoms is hard to predict in experiments.

The time-dependent behaviour of the main plasma parameters for these cases is demonstrated with the media files supplemented with the dissertation; the files are also available online at drive.google.com (hyperlink). The files are named `nozzle_all_atoms_pfc0d.mp4`, where `d` represents the tenth decimal place for the fraction P_{FC}.

The time-dependent evolution is shown for the following quantities, see Fig. 4.24. The top left and top middle figures show the ion distribution function and the atom distribution function, respectively. The top right figure shows the ion and atom densities, the left bottom is for the ion flow velocity, and the middle bottom is for the electrostatic potential. The right bottom figure shows the ion and atom velocity distributions near the recycling wall ($z = L$). Note, that x-axes represent the spatial coordinate along a magnetic field line, normalized to the system length on the phase space figures and in meters elsewhere.

(a) (b)
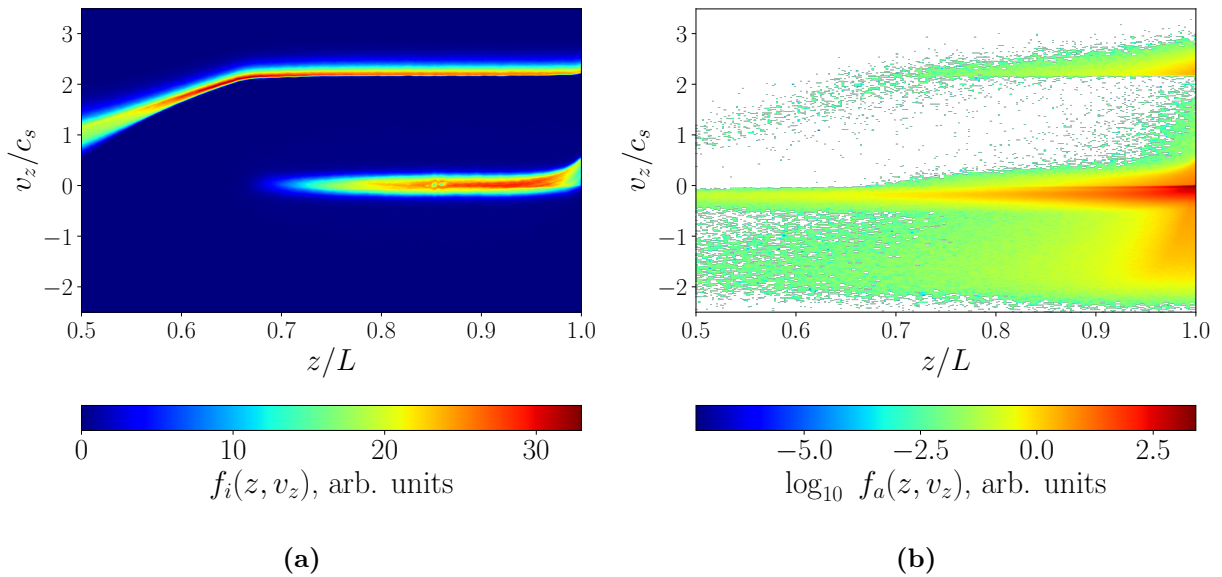
Figure 4.23: Instantaneous plots of velocity distribution functions for ions (a) and atoms (b) in (z, v_z)-space, case for high fraction of Franck-Condon atoms, $P_{FC} = 0.8$.
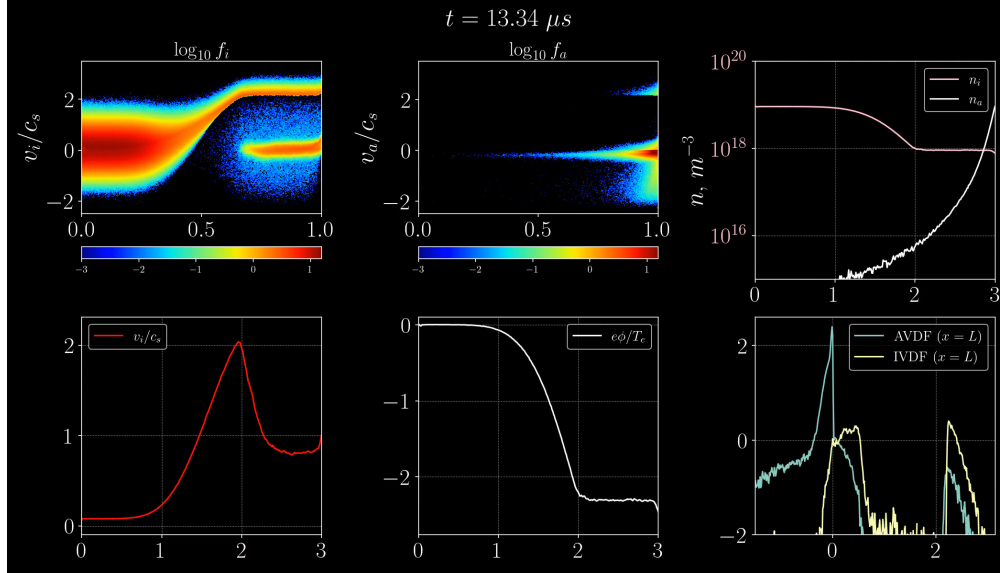
Figure 4.24: Single video frame from supplementary video files demonstrating temporal evolution of the main plasma quantities for the variable fraction of Franck-Condon atoms P_{FC}.

4.3.4 Sheath effect

This model does not resolve the Debye sheath near the wall with assumed quasineutrality. It is included as a parameter $\Delta\phi_D$ and its effect is studied with the three cases: $\Delta\phi_D = (0, 500, 1000)$ V (other parameter are identical to Base case). The added sheath further accelerates ions upon their wall bombardment. This leads to decrease of reflection yield R_N (see Fig. 4.14), thus increasing slow desorbed atoms, due to the balance Eq. (4.18). As we saw previously, the accumulation of cold atoms near the wall can initiate ion-ion instability. Both cases with added sheath increase atom density near the wall and trigger the ion-ion streaming instability. Spatial profiles show a close agreement between these cases, Figs. 4.25a and 4.25b.

4.4 Summary and conclusions

Divertors for linear fusion devices are commonly designed as magnetic mirrors on both ends of a device [112, 122]. They help confine the plasma and control the output power (spreading
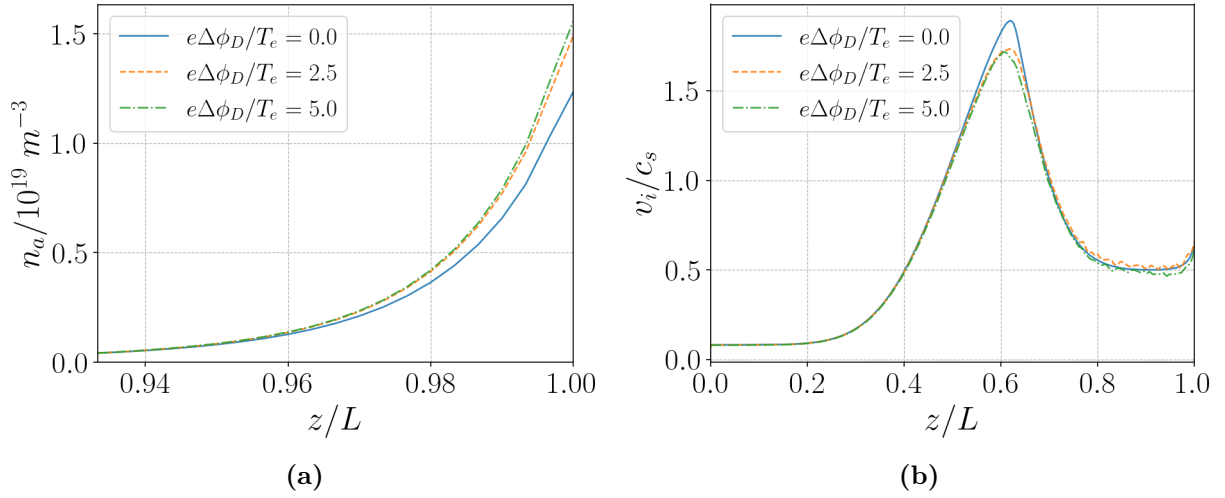
Figure 4.25: Spatial profiles of atom density near the wall (a) and ion velocity in the whole domain (b), demonstrating effect of sheath potential near recycling wall.

the energy flux into the larger wall area) by the diverging magnetic field lines – expander. Thus, some plasma-wall contact is unavoidable and, in some cases, can be used to control plasma potential in the whole system by wall biasing (e.g., for stabilization, confinement). It is possible due to high electron mobility along magnetic field lines, making the system global and potentially vulnerable to the perturbations near the wall. Plasma-wall interaction leads to many effects. Here we focus on the effects related to the recycling of incoming ions. A population of neutral atoms near the wall leads to additional ionization and plasma sources that affect the plasma flow by decreasing the overall potential drop and excitation of instabilities.

For this study, we constructed a hybrid model with drift-kinetic ions, kinetic atoms, and the Boltzmann model for electrons. The atom transport includes relatively fast reflected components and slower atoms due to the surface desorption. Atom collisions, charge exchange (CX) with ions, and ionization by electron impact are also included. It is shown that atoms due to desorption has the most significant direct effect due to small mean free paths. They contribute to creating a high-density cold plasma source near the wall. The ions in this source cannot penetrate deeply into the system as being reflected with both electric field and the magnetic mirror force. Such an ion source decreases the overall plasma potential, which is generally harmful to the whole device (increases electron losses from the source).

One of the findings of this work is the possible excitation of the ion-ion streaming insta-bility, leading to a high turbulence zone near the wall. The instability generally is triggered with the sufficiently high density of the cold plasma source. For example, the direct way is to increase the ratio of the cold atoms near the wall, leading to the high-density cold plasma source, which is demonstrated in the results of this work. Thus, other mechanisms leading to the increased cold atom population can potentially trigger the instability.

The overall number of recycled atoms is proportional to the incoming plasma flux (minus portion defined by a sticking coefficient); thus, its reduction is beneficial for both confinement and reduction of emitted atoms. We show that with the same incoming plasma flux but increased ion temperature (in the source), the flux on the wall is smaller [115], and the atom recycling also decreases. Thus, the plasma source generated near the wall is of relatively low density, and the decrease in plasma potential drop (over the whole channel) is relatively low.

Among the whole population of atoms, reflected particles have large mean free paths and thus low density; they are almost transparent for the original ion beam. But in the equilibrium wall model, they affect the overall recycled balance, Eq. (4.14), thus "controlling" the portion of desorbed atoms. This indirect mechanism is demonstrated in the example with added sheath potential (on the recycling wall). Higher sheath potential increases ion bombardment energy and thus decreases the reflection coefficient R_N (Fig. 4.5a). We show that, indeed, it can lead to the excitement of the ion-ion streaming instability: increased density of cold atoms caused the cold ion beam with higher density.

Chapter 5

Summary and conclusion

Plasma physics is a broad subject with numerous applications in the laboratory and nature. Weakly coupled plasma is subject to complex collective effects (on time scales larger than plasma frequency and length scales larger than Debye length) that bring a variety of wave and nonlinear processes. In this thesis, I considered several nonlinear phenomena of interest for electric propulsion (such as Hall thrusters) and fusion applications. Emphasis is on the dynamic behaviour of plasma flow and instabilities, taking into account ionization and other atomic processes such as charge exchange (CX) interaction.

A comprehensive numerical study of the low-frequency axial dynamics of Hall thrusters was presented in Chapter 2. Breathing modes are low-frequency bulk plasma oscillations observed in most Hall thrusters. They are commonly recognized today as having a clear ionization footprint and scaling with atomic fly-by times, thus resulting in low-frequency 5-50 kHz oscillations (atom flow with $\sim 150\,\mathrm{m/s}$ in $\sim 1\,\mathrm{cm}$ channel). Plasma and neutral density exhibit periodic replacements due to ionization, accompanied by oscillations of the total current, thrust, and other important plasma parameters. Two models, full fluid and hybrid, were employed to capture the low-frequency modes within the benchmarking LANDMARK project [36]. We identified two regimes with the breathing modes present: one with the pure breathing mode of high-amplitude, and the second regime where the breathing mode is of lower amplitude co-exist with the higher frequency resistive modes. Both models confirmed these two regimes. During the benchmark study, it was shown that the ion pressure could not be neglected in the fluid model in the presence of the resistive modes (for their accurate representation). Additionally, the ion heating effect caused by the resistive modes was observed, suggesting that the ion energy balance equation should be resolved in the fluid model. For the case with the pure (solo) breathing mode, it was found that near-anode dynamics

play a key role; it was investigated further.

In Chapter 3 we propose a mechanism for the solo breathing mode regime, highlighting the importance of the ion backflow region, which complements the common picture of the ionization nature of breathing modes. The ion backflow is the region with a negative ion velocity near the anode (with a negative electric field); it is formed due to the large contribution of the electron diffusion to the total current. Using a simplified (reduced) fluid model, employing only continuity equations for ions and atoms (resolving time and axial space coordinates), we show that the ion backflow gives rise to periodic low-frequency oscillations that scale with the size of the ion backflow region. Feeding our reduced model with the actual velocity and ionization rate profiles from more complete models (obtained in the previous Chapter), we show confident similarity in the density behaviours, thus isolating the mechanism for ion and atom dynamics in the presence of a large presheath region. This region is similar to the presheath region near the plasma-wall boundary, but the mechanism is different. The presheath obtained in this model occurs in a purely quasineutral plasma. The electric field toward the anode appears due to a density gradient in the anode region providing the additional current, so the negative electric field is induced to maintain quasineutrality. This study demonstrates that electron diffusion cannot be ignored in models of axial dynamics of a Hall thruster. A presence of a self-consistent presheath region can destabilize low-frequency modes. Standard zero-dimensional predator-prey models miss this mechanism and do not predict the instabilities.

Dynamic behaviour of plasma flow is important for many other applications, in particular for open-mirror-based fusion systems. A particular topic considered in Chapter 4 is related to a divertor in open-ended large-scale fusion devices. The converging-diverging magnetic field (magnetic mirror) is used to confine the plasma in the fusion core. Inevitably, plasma leakage (losses in a magnetic mirror) through the ends of the mirror trap create flows accelerated to supersonic velocities (in established global electrostatic potential structure). The plasma (ion) flow to the wall is accompanied by the wall recycling process in which ions bombarding the wall are neutralized and returned back to plasma. Then the near-wall region becomes contaminated with neutral atoms of various energy. These neutrals can interact with ions via the CX process resulting in the ion streams of different energy, which modifies

the global electric field and produce two-stream instabilities. The hybrid model with drift-kinetic ions, fluid (Boltzmann) electrons, and kinetic neutral atoms was developed to study such processes, global plasma flow in the magnetic mirror, and near-wall atomic interactions. CX and ionization collisions are simulated via the direct simulation Monte Carlo (DSMC) method. The collision events in this setup are rare, with Knudsen numbers in the range 0.1-10. Thus, the DSMC method is justified for the accurate evaluation of collision rates in regimes with non-Maxwellian distributions. We demonstrate its initial capabilities on a few test cases of divertor configuration and full atom transport model. The model predicts some results reported before, e.g. that high ion energy in the source reduces the neutral emission and improves confinement. Additionally, we demonstrate a possible development of the ion-ion streaming instability due to the low-energy ion source arising via neutral CX and ionization. It is shown that a large fraction of slow atoms (due to desorption) present near the wall effectively triggers the instability. Thus removal of this atom component can be beneficial for the device operation.

Results of additional exploratory studies related to Hall thruster modeling are presented in Appendices. In Appendix A a model of dynamic anomalous electron mobility is formulated, which explicitly takes into account the dependence of electron mobility on the local value of the electric field. In Appendix B one-dimensional fluid model extension is presented, supplementing electron inertial effects to the drift-diffusion electron model. Appendix C the system of full nonlinear fluid equations with ionization is formulated for two-dimensional case (axial-azimuthal). In Appendix D, a simple control algorithm based on the proportional-derivative controller is demonstrated; its proof of principle is shown for stabilization of the breathing mode by modulation of the applied potential.

References

[1] W. Crookes. On radiant matter. *Journal of the Franklin Institute*, 108(5):305–316, 1879.

[2] R. Fitzpatrick. *Plasma physics: an introduction*. CRC Press, Boca Raton, 2014.

[3] A.I. Morozov. *Introduction to plasma dynamics*. CRC Press, Boca Raton, 2012.

[4] K.E. Tsiolkovsky. Investigation of outer space using reactive devices (in Russian). *Nauchno-filosofskij i literaturnyj zhurnal, № 5*, 1903. Available online: tsiolkovsky.org [Accessed: 6-February-2022].

[5] K.E. Tsiolkovskiy. Works of rocket technology. *NASA Technical Translation, TTF-243, NASA*, 1965. Available online: tsiolkovsky.org [Accessed: 6-February-2022].

[6] D.M. Goebel and I. Katz. *Fundamentals of electric propulsion: ion and Hall thrusters*, volume 1. John Wiley & Sons, Hoboken, 2008.

[7] A.I. Morozov and V.V. Savel'ev. Fundamentals of stationary plasma thruster theory. In *Reviews of Plasma Physics*, pages 203–391. Springer, 2000.

[8] J.-P. Boeuf. Tutorial: Physics and modeling of Hall thrusters. *Journal of Applied Physics*, 121(1):011101, 2017.

[9] G.S. Janes and R.S. Lowder. Anomalous electron diffusion and ion acceleration in a low-density plasma. *The Physics of Fluids*, 9(6):1115–1123, 1966.

[10] J.C. Adam, J.-P. Boeuf, N. Dubuit, M. Dudeck, L. Garrigues, D. Gresillon, A. Heron, G.J.M. Hagelaar, V. Kulaev, N. Lemoine, S. Mazouffre, J. Perez Luna, V. Pisarev, and S. Tsikata. Physics, simulation and diagnostics of Hall effect thrusters. *Plasma Physics and Controlled Fusion*, 50(12):124041, Nov 2008.

[11] T. Lafleur, S.D. Baalrud, and P. Chabert. Theory for the anomalous electron transport in Hall effect thrusters. I. insights from particle-in-cell simulations. *Physics of Plasmas*, 23(5):053502, 2016.

[12] D. Bohm. The characteristics of electrical discharges in magnetic fields. *Qualitative Description of the Arc Plasma in a Magnetic Field*, 1949.

[13] Wikipedia. Nuclear binding energy – Wikipedia, the free encyclopedia. `http://en.wikipedia.org/wiki/Nuclear_binding_energy#Nuclear_binding_energy_curve`, 2022. [Online; Accessed: 13-January-2022].

[14] F.F. Chen. *Introduction to plasma physics*. Springer Science & Business Media, 2012.

[15] F.R.C. Diaz. The VASIMR rocket. *Scientific American*, 283(5):90–97, 2000.

[16] D.D. Ryutov. Open-ended traps. *Phys. Usp.*, 31(4):300–327, 1988.

[17] A.I. Smolyakov, A. Sabo, P. Yushmanov, and S. Putvinskii. On quasineutral plasma flow in the magnetic nozzle. *Physics of Plasmas*, 28(6):060701, 2021.

[18] B.A. Wetherton, A. Le, J. Egedal, C. Forest, W. Daughton, A. Stanier, and S. Boldyrev. A drift kinetic model for the expander region of a magnetic mirror. *Physics of Plasmas*, 28(4):042510, 2021.

[19] F.H. Ebersohn, J.P. Sheehan, A.D. Gallimore, and J.V. Shebalin. Kinetic simulation technique for plasma flow in strong external magnetic field. *Journal of Computational Physics*, 351:358–375, 2017.

[20] J.A. Bittencourt. *Fundamentals of plasma physics*. Springer Science & Business Media, New York, 2004.

[21] J.H. Whealton, R.W. McGaffey, and P.S. Meszaros. A finite difference 3-D Poisson-Vlasov algorithm for ions extracted from a plasma. *Journal of Computational Physics*, 63(1):20–32, 1986.

[22] F. Engelmann, M. Feix, E. Minardi, and J. Oxenius. Nonlinear effects from Vlasov's equation. *The Physics of Fluids*, 6(2):266–275, 1963.

[23] O. Koshkarov, G. Manzini, G.L. Delzanno, C. Pagliantini, and V. Roytershteyn. The multi-dimensional Hermite-discontinuous Galerkin method for the Vlasov-Maxwell equations. *Computer Physics Communications*, 264:107866, 2021.

[24] E.A. Frieman and Liu Chen. Nonlinear gyrokinetic equations for low-frequency electromagnetic waves in general plasma equilibria. *The Physics of Fluids*, 25(3):502–508, 1982.

[25] F.H. Harlow, M. Evans, and R.D. Richtmyer. A machine calculation method for hydrodynamic problems. Technical report, Los Alamos Scientific Laboratory of the University of California, 1955.

[26] J.U. Brackbill. Introduction to Harlow's scientific memoir. *Journal of Computational Physics*, 195(2):413–413, 2004.

[27] J. Dawson. One-dimensional plasma model. *The Physics of Fluids*, 5(4):445–459, 1962.

[28] C.K. Birdsall and A.B. Langdon. *Plasma physics via computer simulation*. CRC press, Boca Raton, 2018.

[29] A.Y. Aydemir. A unified monte carlo interpretation of particle simulations and applications to non-neutral plasmas. *Physics of Plasmas*, 1(4):822–831, 1994.

[30] A. Tavassoli, O. Chapurin, M. Jimenez, M. Papahn Zadeh, T. Zintel, M. Sengupta, L. Couëdel, R.J. Spiteri, M. Shoucri, and A. Smolyakov. The role of noise in PIC and Vlasov simulations of the buneman instability. *Physics of Plasmas*, 28(12):122105, 2021.

[31] B.D. Dudson, M.V. Umansky, X.Q. Xu, P.B. Snyder, and H.R. Wilson. BOUT++: A framework for parallel plasma fluid simulations. *Computer Physics Communications*, 180(9):1467–1480, 2009.

[32] B.D. Dudson et al. BOUT++. `https://github.com/boutproject/BOUT-dev`, 2022.

[33] B.D. Dudson, A. Allen, G. Breyiannis, E. Brugger, J. Buchanan, L. Easy, S. Farley, I. Joseph, M. Kim, A.D. McGann, et al. BOUT++: Recent and current developments. *Journal of Plasma Physics*, 81(01):365810104, 2015.

[34] A.C. Hindmarsh, P.N. Brown, K.E. Grant, S.L. Lee, R. Serban, D.E. Shumaker, and C.S. Woodward. SUNDIALS: Suite of nonlinear and differential/algebraic equation solvers. *ACM Transactions on Mathematical Software (TOMS)*, 31(3):363–396, 2005.

[35] G. Hagelaar. Modelling methods for low-temperature plasmas, 2008. Habilitation thesis.

[36] Low temperAture magNetizeD plasMA benchmaRKs. `https://www.landmark-plasma.com/`, 2018. [Accessed: 26-March-2021].

[37] O. Chapurin, A.I. Smolyakov, G. Hagelaar, Boeuf J.-P., and Y. Raitses. Fluid and hybrid simulations of the ionization instabilities in Hall thruster, 2022. arXiv 2201.11280.

[38] A.I. Smolyakov, O. Chapurin, W. Frias, O. Koshkarov, I. Romadanov, T. Tang, M. Umansky, Y. Raitses, I.D. Kaganovich, and V.P. Lakhin. Fluid theory and simulations of instabilities, turbulent transport and coherent structures in partially-magnetized plasmas of discharges. *Plasma Physics and Controlled Fusion*, 59(1):014041, 2016.

[39] S. Janhunen, A. Smolyakov, O. Chapurin, D. Sydorenko, I. Kaganovich, and Y. Raitses. Nonlinear structures and anomalous transport in partially magnetized E×B plasmas. *Physics of Plasmas*, 25(1):011608, 2018.

[40] S. Janhunen, A. Smolyakov, D. Sydorenko, M. Jimenez, I. Kaganovich, and Y. Raitses. Evolution of the electron cyclotron drift instability in two-dimensions. *Physics of Plasmas*, 25(8):082308, 2018.

[41] W. Villafana, F. Petronio, A.C. Denig, M.J. Jimenez, D. Eremin, L. Garrigues, F. Taccogna, A. Alvarez-Laguna, J.-P. Boeuf, A. Bourdon, P. Chabert, T. Charoy, B. Cuenot, K. Hara, F. Pechereau, A. Smolyakov, D. Sydorenko, A. Tavant, and O. Vermorel. 2D radial-azimuthal particle-in-cell benchmark for E×B discharges. *Plasma Sources Science and Technology*, 30(7):075002, jul 2021.

[42] M. Jimenez. 2D3V Particle-in-cell simulations of Electron Cyclotron Drift Instability and anomalous electron transport in E×B plasmas. Master's thesis, University of Saskatchewan, 2021.

[43] I.D. Kaganovich, A. Smolyakov, Y. Raitses, E. Ahedo, I.G. Mikellides, B. Jorns, F. Taccogna, R. Gueroult, S. Tsikata, A. Bourdon, J.-P. Boeuf, M. Keidar, A.T. Powis, M. Merino, M. Cappelli, K. Hara, J.A. Carlsson, N.J. Fisch, P. Chabert, I. Schweigert, T. Lafleur, K. Matyash, A.V. Khrabrov, R.W. Boswell, and A. Fruchtman. Physics of E×B discharges relevant to plasma propulsion and similar technologies. *Physics of Plasmas*, 27(12):120601, 2020.

[44] Y.B. Esipchuk, A.I. Morozov, G.N. Tilinin, and A.V. Trofimov. Plasma oscillations in closed-drift accelerators with an extended acceleration zone. *Soviet Physics Technical Physics*, 18:928, 1974.

[45] J. Fife, M. Martinez-Sanchez, J. Szabo, J. Fife, M. Martinez-Sanchez, and J. Szabo. A numerical study of low-frequency discharge oscillations in Hall thrusters. In *33rd Joint Propulsion Conference and Exhibit*, page 3052, 1997.

[46] S. Barral and E. Ahedo. On the origin of low frequency oscillations in Hall thrusters. *AIP Conference Proceedings*, 993(1):439–442, 2008.

[47] K. Hara, M. J Sekerak, I.D. Boyd, and A.D. Gallimore. Perturbation analysis of ionization oscillations in Hall effect thrusters. *Physics of Plasmas*, 21(12):122103, 2014.

[48] O. Chapurin, A.I. Smolyakov, G. Hagelaar, and Y. Raitses. On the mechanism of ionization oscillations in Hall thrusters. *Journal of Applied Physics*, 129(23):233307, 2021.

[49] T. Lafleur, P. Chabert, and A. Bourdon. The origin of the breathing mode in Hall thrusters and its stabilization. *Journal of Applied Physics*, 130(5):053305, 2021.

[50] S. Chable and F. Rogier. Numerical investigation and modeling of stationary plasma thruster low frequency oscillations. *Physics of Plasmas*, 12(3):033504, 2005.

[51] K. Makowski, Z. Peradzynski, S. Barral, and Michel A. Dudeck. Review of the plasma fluid models in stationary plasma thrusters. *High Temperature Material Processes: An International Quarterly of High-Technology Plasma Processes*, 5(2), 2001.

[52] G.J.M. Hagelaar, J. Bareilles, L. Garrigues, and J.-P. Boeuf. Modelling of stationary plasma thrusters. *Contributions to Plasma Physics*, 44(5-6):529–535, 2004.

[53] J.-P. Boeuf and L. Garrigues. Low frequency oscillations in a stationary plasma thruster. *Journal of Applied Physics*, 84(7):3541–3554, 1998.

[54] S. Barral, Z. Peradzynski, K. Makowski, and Michel A. Dudeck. Fluid model of Hall thruster-comparison with hybrid model. *High Temperature Material Processes: An International Quarterly of High-Technology Plasma Processes*, 5(2), 2001.

[55] S. Barral and E. Ahedo. Low-frequency model of breathing oscillations in Hall discharges. *Physical Review E*, 79(4):046401, 2009.

[56] V. Giannetti, M.M. Saravia, L. Leporini, S. Camarri, and T. Andreussi. Numerical and experimental investigation of longitudinal oscillations in Hall thrusters. *Aerospace*, 8(6):148, 2021.

[57] A.I. Morozov and V.V. Savel'ev. One-dimensional hybrid model of a stationary plasma thruster. *Plasma Physics Reports*, 26(10):875–880, 2000.

[58] A. Shashkov, A. Lovtsov, and D. Tomilin. A one-dimensional with three-dimensional velocity space hybrid-PIC model of the discharge plasma in a Hall thruster. *Physics of Plasmas*, 24(4):043501, 2017.

[59] Gavrikov M.B. and Taiurskii A.A. Hybrid model of a stationary plasma thruster (in Russian). *Preprints Keldysh Institute of Applied Mathematics*, (0):35–47, 2021.

[60] G.J.M. Hagelaar, J. Bareilles, L.B.J.P. Garrigues, and J.-P. Boeuf. Two-dimensional model of a stationary plasma thruster. *Journal of Applied Physics*, 91(9):5592–5598, 2002.

[61] G.J.M. Hagelaar, J. Bareilles, L. Garrigues, and J.-P. Boeuf. Role of anomalous electron transport in a stationary plasma thruster simulation. *Journal of Applied Physics*, 93(1):67–75, 2003.

[62] A.A. Litvak and Nathaniel J. Fisch. Resistive instabilities in Hall current plasma discharge. *Physics of Plasmas*, 8(2):648–651, 2001.

[63] E. Fernandez, M.K. Scharfe, C.A. Thomas, N. Gascon, and M.A. Cappelli. Growth of resistive instabilities in E×B plasma discharge simulations. *Physics of Plasmas*, 15(1):012102, 2008.

[64] O. Koshkarov, A.I. Smolyakov, I.V. Romadanov, O. Chapurin, M.V. Umansky, Y. Raitses, and I.D. Kaganovich. Current flow instability and nonlinear structures in dissipative two-fluid plasmas. *Physics of Plasmas*, 25(1):011604, 2018.

[65] A.I. Morozov and V.V. Savel'ev. One-dimensional hydrodynamic model of the atom and ion dynamics in a stationary plasma thruster. *Plasma Physics Reports*, 26(3):219–224, 2000.

[66] Gavrikov M.B. and Taiurskii A.A. Some mathematical questions of plasma ionization (in Russian). *Preprints Keldysh Institute of Applied Mathematics*, (94):1–48, 2021.

[67] A. Cohen-Zur, A. Fruchtman, J. Ashkenazy, and A. Gany. Analysis of the steady-state axial flow in the Hall thruster. *Physics of Plasmas*, 9(10):4363–4374, 2002.

[68] E. Ahedo and J. Rus. Vanishing of the negative anode sheath in a Hall thruster. *Journal of Applied Physics*, 98(4):043306, 2005.

[69] L. Dorf, V. Semenov, and Y. Raitses. Anode sheath in Hall thrusters. *Applied Physics Letters*, 83(13):2551–2553, 2003.

[70] L. Dorf, Y. Raitses, and N.J. Fisch. Experimental studies of anode sheath phenomena in a Hall thruster discharge. *Journal of Applied Physics*, 97(10):103309, 2005.

[71] A. Smolyakov, O. Chapurin, I. Romadanov, Y. Raitses, I. Kaganovich, G. Hagelaar, and J.-P. Boeuf. Stationary profiles and axial mode oscillations in Hall thrusters. In *AIAA Propulsion and Energy 2019 Forum*, pages 4080–4080, 2019.

[72] C.K. Birdsall. Particle-in-cell charged-particle simulations, plus Monte Carlo collisions with neutral atoms, PIC-MCC. *IEEE Transactions on plasma science*, 19(2):65–85, 1991.

[73] K.L. Cartwright, J.P. Verboncoeur, and Charles K. Birdsall. Loading and injection of maxwellian distributions in particle simulations. *Journal of Computational Physics*, 162(2):483–513, 2000.

[74] N.B. Meezan, W.A. Hargus Jr, and M.A. Cappelli. Anomalous electron mobility in a coaxial Hall discharge plasma. *Physical Review E*, 63(2):026410, 2001.

[75] W.A. Hargus and M.A. Cappelli. Interior and exterior laser-induced fluorescence and plasma measurements within a Hall thruster. *Journal of Propulsion and Power*, 18(1):159–168, 2002.

[76] K. Hara, I.D. Boyd, and V.I. Kolobov. One-dimensional hybrid-direct kinetic simulation of the discharge plasma in a Hall thruster. *Physics of Plasmas*, 19(11):113508, 2012.

[77] J.J. Szabo. *Fully kinetic numerical modeling of a plasma thruster*. PhD thesis, Massachusetts Institute of Technology, 2001.

[78] F. Taccogna, S. Longo, M. Capitelli, and R. Schneider. Plasma flow in a Hall thruster. *Physics of Plasmas*, 12(4):043502, 2005.

[79] H. Liu, B. Wu, D. Yu, Y. Cao, and P. Duan. Particle-in-cell simulation of a Hall thruster. *Journal of Physics D: Applied Physics*, 43(16):165202, apr 2010.

[80] T. Charoy. *Numerical study of electron transport in Hall thrusters*. PhD thesis, Institut polytechnique de Paris, 2020.

[81] P. Coche and L. Garrigues. A two-dimensional (azimuthal-axial) particle-in-cell model of a Hall thruster. *Physics of Plasmas*, 21(2):023503, 2014.

[82] SIGLO database. `www.lxcat.net/SIGLO`. [Retrived: June-2013].

[83] G.J.M. Hagelaar and L.C. Pitchford. Solving the boltzmann equation to obtain electron transport coefficients and rate coefficients for fluid models. *Plasma Sources Science and Technology*, 14(4):722, 2005.

[84] V. Zhurin, J. Kahn, H. Kaufman, K. Kozubsky, and M. Day. Dynamic characteristics of closed drift thrusters. In *23rd International Electric Propulsion Conference*, 1993.

[85] J.M. Fife. *Hybrid-PIC modeling and electrostatic probe survey of Hall thrusters*. PhD thesis, Massachusetts Institute of Technology, 1998.

[86] C. Wang, L. Wei, and D. Yu. A Basic Predator-Prey Type Model for Low Frequency Discharge Oscillations in Hall Thrusters. *Contributions to Plasma Physics*, 51(10):981–988, 2011.

[87] E.T. Dale and B. Jorns. Frequency scaling of the Hall thruster breathing mode. In *AIAA Propulsion and Energy 2019 Forum*, 2019.

[88] E.T. Dale and B.A. Jorns. Two-zone Hall thruster breathing mode mechanism, Part I: Theory. In *36th International Electric Propulsion Conference, University of Vienna, Austria*, 2019.

[89] E.T. Dale and B.A. Jorns. Two-zone Hall thruster breathing mode mechanism, Part II: Experiment. In *36th International Electric Propulsion Conference, University of Vienna, Austria*, 2019.

[90] A. Smolyakov, O. Chapurin, I. Romadanov, Y. Raitses, and I. Kaganovich. Theory and modelling of axial mode oscillations in Hall thruster. In *AIAA Propulsion and Energy 2019 Forum*, 2019.

[91] N. Yamamoto, T. Nakagawa, K. Komurasaki, and Y. Arakawa. Discharge plasma fluctuations in Hall thrusters. *Vacuum*, 65(3-4):375–381, 2002.

[92] N. Yamamoto, K. Komurasaki, and Y. Arakawa. Discharge current oscillation in Hall thrusters. *Journal of Propulsion and Power*, 21(5):870–876, 2005.

[93] N. Yamamoto, S. Yokota, K. Watanabe, A. Sasoh, K. Komurasaki, and Y. Arakawa. Suppression of discharge current oscillations in a Hall thruster. *Transactions of the Japan Society for Aeronautical and Space Sciences*, 48(161):169–174, 2005.

[94] K. Hara and K. Kubota. Direct kinetic simulation of ion acoustic turbulence in cathode plume. In *35th International Electric Propulsion Conference, Atlanta, Georgia, IEPC-2017-496*, 2017.

[95] L.Q. Wei, L. Han, D.R. Yu, and N. Guo. Low-Frequency Oscillations in Hall Thrusters. *Chinese Physics B*, 24(5):055201, 2015.

[96] Y. Raitses, D. Staack, A. Dunaevsky, and N.J. Fisch. Operation of a segmented Hall thruster with low-sputtering carbon-velvet electrodes. *Journal of Applied Physics*, 99(3):036103, 2006.

[97] I. Romadanov, Y. Raitses, and A. Smolyakov. Hall thruster operation with externally driven breathing mode oscillations. *Plasma Sources Science and Technology*, 27(9):094006, 2018.

[98] N.J. Fisch, Y. Raitses, L.A. Dorf, and A.A. Litvak. Variable operation of Hall thruster with multiple segmented electrodes. *Journal of Applied Physics*, 89(4):2040–2046, 2001.

[99] G.J.M. Hagelaar. Modelling electron transport in magnetized low-temperature discharge plasmas. *Plasma Sources Science and Technology*, 16(1):S57, 2007.

[100] HALL Ion Sources simulation software. `https://www.hallis-model.com/`. [Accessed: 26-March-2021].

[101] L. Wei, C. Wang, K. Han, and D. Yu. Effect of ionization distribution on the low frequency oscillations mode in Hall thrusters. *Physics of Plasmas*, 19(1), 2012.

[102] E. Ahedo, P. Martinez-Cerezo, and M. Martinez-Sanchez. One-dimensional model of the plasma flow in a Hall thruster. *Physics of Plasmas*, 8(6):3058–3068, 2001.

[103] I.V. Romadanov, A.I. Smolyakov, E.A. Sorokina, V.V. Andreev, and N.A. Marusov. Stability of ion flow and role of boundary conditions in a simplified model of the ExB plasma accelerator with a uniform electron mobility. *Plasma Physics Reports*, 46(4):363–373, 2020.

[104] A.I. Morozov and V.V. Savel'ev. One-dimensional hydrodynamic model of the atom and ion dynamics in a stationary plasma thruster. *Plasma Physics Reports*, 26(3):219–224, 2000.

[105] A.I. Morozov and V.V. Savel'ev. One-dimensional hybrid model of a stationary plasma thruster. *Plasma Physics Reports*, 26(10):875–880, 2000.

[106] K. Hara and K. Hanquist. Test cases for grid-based direct kinetic modeling of plasma flows. *Plasma Sources Science & Technology*, 27(6), 2018.

[107] E. Fernandez, M.K. Scharfe, C.A. Thomas, N. Gascon, and M.A. Cappelli. Growth of resistive instabilities in exb plasma discharge simulations. *Physics of Plasmas*, 15(1):012102, 2008.

[108] O. Koshkarov, A.I. Smolyakov, I.V. Romadanov, O. Chapurin, M.V. Umansky, Y. Raitses, and I.D. Kaganovich. Current flow instability and nonlinear structures in dissipative two-fluid plasmas. *Physics of Plasmas*, 25(1):011604, 2018.

[109] D. Staack, Y. Raitses, and N.J. Fisch. Temperature gradient in Hall thrusters. *Applied Physics Letters*, 84(16):3028–3030, 2004.

[110] J. Kurzyna, K. Makowski, Z. Peradzynski, A. Lazurenko, S. Mazouffre, and M. Dudeck. Where is the breathing mode? High voltage Hall effect thruster studies with EMD method. *AIP Conference Proceedings*, 993(1):443–446, 2008.

[111] D.D. Ryutov, P.N. Yushmanov, D.C. Barnes, and S.V. Putvinski. Divertor for a linear fusion device. *AIP Conference Proceedings*, 1721(1):060003, 2016.

[112] M.W. Binderbauer, T. Tajima, L.C. Steinhauer, E. Garate, M. Tuszewski, L. Schmitz, H.Y. Guo, A. Smirnov, H. Gota, D. Barnes, et al. A high performance field-reversed configuration. *Physics of Plasmas*, 22(5):056110, 2015.

[113] D.D. Ryutov. Axial electron heat loss from mirror devices revisited. *Fusion science and technology*, 47(1T):148–154, 2005.

[114] E.W. Thomas, R.K. Janev, and J. Smith. Scaling of particle reflection coefficients. *Nuclear Instruments and Methods in Physics Research Section B: Beam Interactions with Materials and Atoms*, 69(4):427–436, 1992.

[115] M. Jimenez, A. Smolyakov, O. Chapurin, and P. Yushmanov. Kinetic effects in plasma flow in the magnetic nozzle, 2022 forthcoming.

[116] V. Vahedi and M. Surendra. A monte carlo collision model for the particle-in-cell method: applications to argon and oxygen discharges. *Computer Physics Communications*, 87(1):179–198, 1995. Particle Simulation Methods.

[117] R.K. Janev, W.D. Langer, E. Evans Jr, and D.E. Post Jr. *Elementary processes in hydrogen-helium plasmas: cross sections and reaction rate coefficients*. Springer-Verlag, Berlin, Heidelberg, New York, London, Paris, Tokyo, 2012.

[118] ALADDIN database. `https://www-amdis.iaea.org/ALADDIN/`. [Retrieved: Jan-2022].

[119] W Eckstein and H Verbeek. Reflection of light ions from solids. In *Data Compendium for Plasma-Surface Interactions*, pages 12–12. Nucl. Fusion special issue, 1984.

[120] Y. Xia, X. Xu, C. Tan, L. Mei, H. Yang, and X. Sun. Reflection of light ion from solid surfaces studied by monte carlo simulation and transport theory. *Journal of applied physics*, 69(1):439–446, 1991.

[121] D. Stotler and C. Karney. Neutral gas transport modeling with DEGAS 2. *Contributions to Plasma Physics*, 34(2-3):392–397, 1994.

[122] A. Beklemishev, A. Anikeev, V. Astrelin, P. Bagryansky, A. Burdakov, V. Davydenko, D. Gavrilenko, A. Ivanov, I. Ivanov, M. Ivantsivsky, et al. Novosibirsk project of gas-dynamic multiple-mirror trap. *Fusion Science and Technology*, 63(1T):46–51, 2013.

[123] S. Peter Gary and J.J. Sanderson. Longitudinal waves in a perpendicular collisionless plasma shock: I. cold ions. *Journal of Plasma Physics*, 4(4):739–751, 1970.

[124] M. Lampe, W.M. Manheimer, J.B. McBride, J.H. Orens, K. Papadopoulos, R. Shanny, and R.N. Sudan. Theory and simulation of the beam cyclotron instability. *Physics of Fluids (1958-1988)*, 15(4):662–675, 1972.

[125] J.C. Adam, A. Héron, and G. Laval. Study of stationary plasma thrusters using two-dimensional fully kinetic simulations. *Physics of Plasmas*, 11(1):295–305, 2004.

[126] R. Chodura. A hybrid fluid-particle model of ion heating in high-Mach-number shock waves. *Nuclear Fusion*, 15(1):55, 1975.

Appendix A

Dynamic anomalous resistivity (Chodura)

The Bohm mobility was used in our models for electron anomalous current in the axial model of a Hall thruster. The anomalous current is often due to azimuthal microinstabilities, e.g. electron-cyclotron drift instability [123, 124, 125, 11, 39, 40, 42]. The semi-empirical Chodura anomalous resisitivity was proposed earlier [126], which can be expressed as the collision frequency

$$\nu_{ch} = c\omega_{pi}\left(1 - \exp\left(-\frac{V_d}{fc_s}\right)\right), \tag{A.1}$$

where $\omega_{pi} = \sqrt{e^2 n/\varepsilon_0 m_i}$, $V_d = E/B$, $c_s = \sqrt{T_e/m_i}$, c and f are free parameters. The anomalous collision frequency depends on the electric field, plasma density, and electron temperature that all are dynamic variables. The Chodura collision frequency can be added in the same way as Bohm diffusion, into classical cross-field mobility expression, Eq. (3.24). One can account ν_{ch} only for a region in space with $v_d/c_s > 1$. One can also introduce a time lag of the order $1/\omega_{pi}$, as a typical time required for such instabilities to grow.

Appendix B

Electron inertia

Account for electron inertia effects is important for more accurate prediction of the resistive modes [64].

$$\frac{\partial \mathbf{v}_e}{\partial t} + \mathbf{v}_e \cdot \nabla \mathbf{v}_e = \frac{e}{m_e} \nabla \phi - \omega_{ce} \mathbf{v}_e \times \mathbf{b} - \frac{1}{n_e m_e} \nabla p_e - \nu \mathbf{v}_e, \tag{B.1}$$

One evaluates the electron drift velocity from Eq. (B.1) by multiplying by $\mathbf{b} \times$:

$$\mathbf{v}_{e\perp} = \mathbf{v}_E + \mathbf{v}_{pe} - \frac{\nu}{\omega_{ce}} \mathbf{b} \times \mathbf{v}_\perp - \frac{1}{\omega_{ce}} \left(\frac{\partial \mathbf{v}_e}{\partial t} + \mathbf{v}_e \cdot \nabla \mathbf{v}_e \right), \tag{B.2}$$

which, expanded in a small parameter $1/\omega_{ce}$ gives [38]:

$$\mathbf{v}_{e\perp} = \mathbf{v}_E + \mathbf{v}_{pe} + \mathbf{v}_I + \mathbf{v}_\nu, \tag{B.3}$$

where in the right-hand side the drifts due to ExB, magnetic, inertial, and due to collisions, respectively, expressed as

$$\mathbf{v}_E = \frac{e}{\omega_{ce} m_e} \mathbf{b} \times \nabla \phi, \tag{B.4}$$

$$\mathbf{v}_{pe} = \frac{1}{\omega_{ce} n_e m_e} \mathbf{b} \times \nabla p_e, \tag{B.5}$$

$$\mathbf{v}_\nu = \frac{\nu}{\omega_{ce}} \mathbf{b} \times \left(\mathbf{v}_E + \mathbf{v}_{pe} \right), \tag{B.6}$$

$$\mathbf{v}_I = -\frac{1}{\omega_{ce}} \mathbf{b} \times \left[\frac{\partial}{\partial t} \left(\mathbf{v}_E + \mathbf{v}_{pe} \right) + \left(\mathbf{v}_E + \mathbf{v}_{pe} \right) \cdot \nabla \left(\mathbf{v}_E + \mathbf{v}_{pe} \right) \right], \tag{B.7}$$

with $\mathbf{v}_e \approx \mathbf{v}_E + \mathbf{v}_{pe}$ used in the inertial drift velocity. Diagram with directions of drift velocities is shown in Fig. B.1.
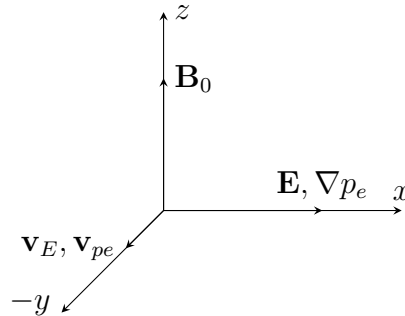

Figure B.1: Drift directions.

Neglecting density gradients in other than axial direction, with electric field along x-direction, and magnetic field along z, we have:

$$v_{ex} = v_{Ix} + v_{\nu x},$$

(B.8)

where

$$v_{Ix} = -\frac{1}{\omega_{ce}} \frac{\partial}{\partial t} \left(\mu_e E_x - \frac{\mu_e}{en_e} \frac{\partial p_e}{\partial x} \right),$$

(B.9)

and thus

$$v_{ex} = \mu_e E_x - \frac{\mu_e}{en_e} \frac{\partial p_e}{\partial x} - \frac{1}{\omega_{ce}} \frac{\partial}{\partial t} \left(\mu_e E_x - \frac{\mu_e}{en_e} \frac{\partial p_e}{\partial x} \right),$$

(B.10)

where $\mu_e = \nu c / \omega_{ce} B_0$. Quasineutrality leads to divergence-free total current

$$\frac{\partial}{\partial x} \left[n\mu_e E_x - \frac{\mu_e}{e} \frac{\partial p_e}{\partial x} + nv_i - \frac{\partial}{\partial t} \left(n\mu_e E_x - \frac{\mu_e}{e} \frac{\partial p_e}{\partial x} \right) \right] = 0,$$

(B.11)

obtained by the addition of electron and ion continuity equations. Now, with some rearrangement one can write

$$\frac{\partial \eta}{\partial t} = \eta + \frac{\partial}{\partial x} (nv_i),$$

(B.12)

where

$$\eta = \frac{\partial}{\partial x} (n\mu_e E_x - \frac{\mu_e}{e} \frac{\partial p_e}{\partial x}),$$

(B.13)

rewritten for potential the inversion problem is

$$\eta = -n\mu_e \frac{\partial^2 \phi}{\partial x^2} - \frac{\mu_e}{e} \frac{\partial^2 p_e}{\partial x^2},$$

(B.14)

where ϕ is found by inverting Eq. (B.14) with the boundary conditions $\phi(0) = U_0$, $\phi(L) = 0$.

In summary, compared to the axial model without electron inertia, here we obtain an additional time-dependent equation (B.12) and inversion problem for the potential is modified to Eq. (B.14).

Appendix C

Two-dimensional extension (axial-azimuthal) of fluid model with ionization

One-dimensional fluid model for the axial direction of a Hall thruster, developed in Chapters 2,3, use the phenomenological model for anomalous electron current. Here we formulate two-dimensional equations that include the azimuthal (periodic) direction. The goal is to capture the physics of electron current more accurately, with the instabilities in the azimuthal direction defining the axial electron mobility. Previously, nonlinear axial-azimuthal fluid simulations were performed for perturbed variables [38], assuming constant gradients within stationary equilibrium profiles, also without neutral dynamics and ionization processes.

Here I present the mathematical formulation of the 2-D fluid model in full variables, with neutral atoms and ionization. Here the electron energy is assumed constant; it should be included in the time-dependent element of the model, similarly to Eq. (2.6). Cartesian coordinates x, y, z represent the axial, azimuthal, and radial direction of a Hall thruster, respectively. Ion dynamics described with the continuity and the momentum balance equations:

$$\frac{\partial n_i}{\partial t} + \nabla \cdot (n_i \mathbf{v}_i) = \beta n_n n_i, \tag{C.1}$$

$$\frac{\partial \mathbf{v}_i}{\partial t} + \mathbf{v}_i \cdot \nabla \mathbf{v}_i = \frac{e}{m_i} \mathbf{E} + \beta n_n \mathbf{v}_i. \tag{C.2}$$

Electrons are represented only with the momentum balance equation (neglecting inertia):

$$0 = eE_x - \frac{\partial_x p_e}{n_i} + \omega_{ce} v_y + \nu v_x, \tag{C.3}$$

$$0 = eE_y - \frac{\partial_y p_e}{n_i} - \omega_{ce} v_x + \nu v_y, \tag{C.4}$$

which results into

$$\mathbf{v}_e = \mu_{e\wedge} \mathbf{E} \times \mathbf{B} + \mu_e \mathbf{E} - \frac{\mu_e}{n_i} \nabla p_e - \frac{\mu_{e\wedge}}{n_i} \nabla p_e \times \mathbf{B}, \tag{C.5}$$

where

$$\mu_{e\wedge} = \frac{e^2}{m_e^2 \nu^2} \frac{1}{1 + \omega_{ce}^2/\nu^2} = \frac{e}{m\nu} \mu_e, \tag{C.6}$$

and μ_e is the classical expression for cross-field electron mobility (3.24). If ionization frictional force $\beta n_n \mathbf{v}_e$ is included in Eqs. (C.3,C.4), ionization frequency βn_n adds up to ν, so $\nu \to \nu + \beta n_n$. Also, it can be noted that in absence of collisional effects ($\nu = 0$), Eq. (C.5) reduces to $\mathbf{v}_e = \mathbf{v}_E + \mathbf{v}_{pe}$, where v_E is the E $\times$ B drift velocity, v_{pe} is the diamagnetic drift velocity.

Continuing with the model, subtracting electron and ion continuity equations and including the Poisson equation $\nabla^2\phi = 4\pi e\,(n_i - n_e)$ gives

$$\frac{1}{4\pi e}\frac{\partial \nabla^2\phi}{\partial t} + \nabla \cdot (n\mathbf{v}_e - n\mathbf{v}_i) = 0, \tag{C.7}$$

and substituting electron drift velocity (C.5) one can solve

$$\frac{1}{4\pi e}\frac{\partial \eta}{\partial t} - n\mu_e\eta - \nabla\,(n\mu)\cdot\nabla\phi + \nabla\cdot(\mu_e\nabla p_e) - B_0\{n\mu_{e\wedge},\phi\} - $$
$$-B_0\{\mu_{e\wedge},p_e\} - \nabla\cdot(n\mathbf{v}_i) = 0, \tag{C.8}$$

where the operator $\{.\}$ denotes the Poisson brackets. Along with time dependent equations for $\eta = \nabla^2\phi$, it needs to be inverted (with proper boundary conditions) for evaluation of potential ϕ. The full normalized system of equations: (stars are omitted, normalization scheme is given below)

$$\frac{\partial n_n}{\partial t} + \mathbf{v}_a \cdot \nabla n_n = -\beta n_n n_i, \tag{C.9}$$

$$\frac{\partial n_i}{\partial t} + \nabla \cdot (n_i\mathbf{v}_i) = \beta n_n n_i, \tag{C.10}$$

$$\frac{\partial \mathbf{v}_i}{\partial t} + \mathbf{v}_i \cdot \nabla\mathbf{v}_i = \mathbf{E} + \beta n_n\mathbf{v}_i, \tag{C.11}$$

$$\frac{1}{4\pi}\frac{\partial \eta}{\partial t} - n\mu_e\eta - \nabla\,(n\mu)\cdot\nabla\phi + \nabla\cdot(\mu_e\nabla p_e) - \{n\mu_{e\wedge},\phi\} - $$
$$-\{\mu_{e\wedge},p_e\} - \nabla\cdot(n\mathbf{v}_i) = 0, \tag{C.12}$$

where $\nabla^2\phi = \eta$ is solved (inverted) at every time step. Boundary conditions in axial direction for η are fixed are fixed to $\eta(0,y) = \eta(L_x,y) = 0$. Note that despite neglected electron inertia, the above system is non-quasineutral. In quasineutral approximation, one obtains the following equation for the electric potential:

$$-\nabla \cdot (n\mu\nabla\phi) + \nabla \cdot (\mu_e\nabla p_e) - \nabla \cdot (n\mu_{e\wedge}\nabla\phi \times \mathbf{B}) - $$
$$\nabla\mu_{e\wedge} \cdot \nabla p_e \times \mathbf{B} - \nabla \cdot (nv_i) = 0, \tag{C.13}$$

which is solved as the boundary value problem, with the specified potential $\phi(0,y) = U_0$, $\phi(L_x,y) = 0$.

Normalization scheme

System length L_x (in axial direction) and ion-sound velocity $c_s = \sqrt{T_e/m_i}$ for a typical electron temperature, $T_e = 20\,\text{eV}$, are chosen as basis for normalization. They form the characteristic frequency $f_0 = c_s/L$. Densities are normalized to the neutral density at the anode $N_0 = n_a(0,t)$ for a given flux (without recombination effect). Normalization scheme:

$$t^* = f_0 t,\ \ x^* = \frac{x}{L_0},\ \ E^* = E\frac{eL_0}{m_iV_0^2},\ \ j^* = \frac{j}{eN_0V_0},\ \ \mu_e^* = \mu_e\frac{m_if_0}{e},\ \ \beta^* = \frac{\beta N_0}{f_0}$$

where m_i is the ion mass, e is the elementary charge. Normalization for η and $\mu_{e\wedge}$:

$$\eta^* = \frac{\eta eL_0^2}{m_iV_0^2},\ \ \mu_{e\wedge}^* = \frac{\mu_{e\wedge}m_i^2f_0^2}{e^2}. \tag{C.14}$$

Appendix D

Stabilization of axial modes with circuit control algorithms

Hall thrusters operate in regimes that may be ineffective or prone to various oscillations (such as breathing modes). One can approach this issue by introducing a control or search algorithm for specific external parameters, such as applied voltage, magnetic field, input mass flow, etc., to obtain a better operation regime. The problem can be formulated in finding a specific set of fixed external parameters (by performing a search in parameter space), or more generally, to vary them dynamically in time, to achieve some goal "on the go". The desired goal or working regime can be a regime with constant power, constant current, maximum efficiency, thrust, etc.
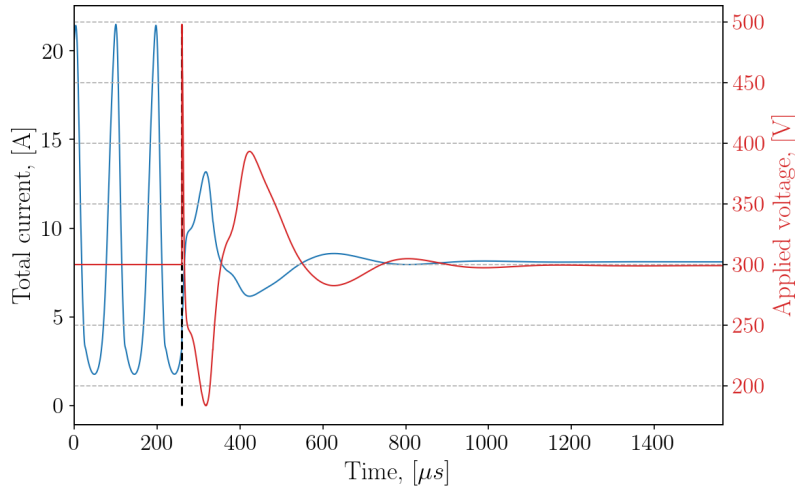

Figure D.1: Total current as a function of time. Dashed line represent a time when PD control was turned ON.

Here, a simple PD (proportional-derivative) controller is applied to the model of breathing mode recovered in the fluid model, given in Chapter 2, Case 2. We only will dynamically control the applied voltage U_0, Eq. (2.16), in order to keep the constant total power P, which generally depends on time as $P = I_T U_0(t)$. The error function is defined as

$$e(t) = P - U_0(t)I(t), \tag{D.1}$$

where $U_0(t)$ and $I(t)$ are instantaneous applied voltage and total current in the system, respectively. The value of P is fixed, it is chosen as $P = I_{av}U_0$, with the average current resulted from natural breathing oscillation I_{av} and $U_0 = 300\,\text{V}$. Finally, the applied voltage

$U_0(t)$ is adjusted dynamically accordingly to the PD algorithm:

$$U_0(t) = K_p e(t) + K_d \frac{de(t)}{dt}, \tag{D.2}$$

where K_p, K_d are proportional and differential coefficients, respectively. The second term of the right-hand side is discretized as $K_d(e(t) - e(t - \Delta t))$, where $\Delta t = 0.4\,\mu$s. Interestingly, we obtained a fully stationary solution by applying the PD controller to the oscillatory (breathing) model, see Fig. D.1. The applied voltage is adjusted in such a way to keep the power constant, and it stabilizes the breathing mode. Note that if PD control is switched off after the stationary state is achieved, the oscillations will start shortly thereafter. We believe this can be used to study the excitation mechanisms of such oscillatory behaviour (e.g., measure its linear growth rate).